Accretion and Feedback Processes in Supermassive Black Holes

Kastytis Zubovas

MPhys (Leicester)

Submitted in fulfilment of the requirements of the degree of
Doctor of Philosophy

15th of May, 2012

Theoretical Astrophysics Group
Department of Physics and Astronomy
University of Leicester

Accretion and Feedback Processes
in Supermassive Black Holes

by

Kastytis Zubovas

MPhys (Leicester)

Supermassive black holes (SMBHs) have been gradually recognised as important elements of galaxy and cosmic structure evolution. Their connection with the large-scale environment is maintained via feedback processes – communication of a fraction of the accretion luminosity to the host galaxy. Feedback is conjectured to expel gas from galaxies, quench star formation and establish the observed correlations between SMBH mass and host galaxy properties. Efficient feedback requires rapid gas accretion and is therefore usually investigated within the context of quasar activity phases in SMBH evolution.

In this Thesis, I investigate several implications of an SMBH wind feedback model, advancing our understanding of feedback processes and the immediate environment of SMBHs. I consider analytically the large-scale outflows and their observable properties. I find that rapidly accreting SMBHs may sweep galaxies clear of gas, turning them into red-and-dead spheroids.

I apply the same feedback model to our Galaxy. Its SMBH, Sgr A*, is currently exceptionally quiescent, although it must have been more active in the past in order to have grown to its present size. I investigate, both analytically and numerically, a short burst of activity which may have occurred ~ 6 million years ago, producing an outflow which formed two large γ-ray emitting bubbles perpendicular to the Galactic plane. The results show that dynamical footprints of outflows may persist for a long time and provide evidence of past AGN activity in quiescent galaxies.

I also present a model for the short-timescale flares observed daily in Sgr A*, based on tidal disruption and evaporation of asteroids in the vicinity of the SMBH. The model explains some observed flare properties, and thus improves our understanding of the processes occurring close to the SMBH. It also provides predictions for observable effects as the quiescent luminosity of Sgr A* varies on long timescales.

Acknowledgements

There are many people who have contributed, directly and indirectly, to my work in these past (almost) three years and helped make this Thesis reality. First and foremost, I am grateful to my supervisors Sergei Nayakshin and Andrew King. Their vast knowledge and experience, suggestions and ideas have made the beginning of my scientific career as exciting and productive as one could ever hope for. I am additionally thankful to Andrew King who was my academic tutor during my undergraduate studies and my Masters research project supervisor; only because of him I have become interested in astrophysics as a career path.

I would also like to thank the rest of the staff at the Theoretical Astrophysics group here in Leicester: Graham Wynn, Mark Wilkinson, Walter Dehnen, Richard Alexander, Justin Read and Giuseppe Lodato. The many discussions during morning tea/coffee breaks and group meetings that I listened to or participated in immensely broadened my understanding of astrophysics. A big thanks as well to Graham Wynn and Mike Goad, who provided me with work experience opportunities during my undergraduate years, allowing me to get a first taste of life as an astrophysics researcher.

My gratitude extends to all the current and former postdocs and graduate students in Theoretical Astrophysics group whom I had the chance to know, learn from, work with or just discuss life, the Universe and everything during tea-time: Chris Power, Celine, Andreas, Seung-Hoon, Sarah, David Maurin, Alex Hobbs, Pete, Fergus, Lee, Ugur, David Cole, Fabrizio, Chris Nixon, Alex Dunhill, Gillian, Hossam, Hastyar and Peter. Also a similar thanks to the X-Ray and Observational Astronomy group students and postdocs: Amy, Katherine, Vicky, Lucy, Kate, Will, Kim, Connor, Ben, Suzy, Jamie, Nathan and Dave. Thank you all for the many pleasant conversations.

I am grateful to the support staff at the University as well. The secretaries Lisa, Kiri, Merry and Joan and computing support team members Gary, Jon, Chris and Liam have always been very helpful in keeping the day-to-day study and research process running smoothly. My research benefitted from the ALICE High Performance Computing Facility at the University of Leicester, which is a part of the DiRAC Facility jointly funded by STFC and the Large Facilities Capital Fund of BIS.

Going back in time, I wish to thank several people without whom I would not have come to Leicester in the first place. They are Cyril Isenberg and Ken Pounds, for offering me, on behalf of the British Physics Olympiad and the University of Leicester, a funded position for an undergraduate degree in Physics; the Lithuanian team leaders of the International Physics Olympiads, Pavlas Bogdanovičius and Antanas Rimvidas Bandzaitis; the teachers at the "Fizikos Olimpas" extracurricular school of physics; and my secondary school Physics teacher Stasė Traigienė.

Of course, my parents are also responsible in no small way for the way my life turned out. Their constant encouragement to delve deeper into the mysteries of the world, the desire to give me the best possible education and support (both financial and emotional) has always helped me. Similarly my friends, both in the UK - especially Karoly, Tomas, Robert, Gediminas and Kai - and back home in Lithuania, have provided me time and

Contents

List of Figures

List of Tables

Dedicated to Ingrida, who waited longer than anyone should ever have to

1
Introduction

"All we have to decide is what to do with the
time that is given to us."

*J. R. R. Tolkien, "The Lord of the Rings",
Book I, Chapter 2*

1.1 What is a black hole?

1.1.1 A historical perspective

Although black holes have been investigated in detail only from approximately the middle of the last century, the first recorded investigations of similar concepts date back to the late 18th. Michell (1784) discussed the possibility of an object, perhaps a star, so massive that not even light could escape from its surface. Using classical (i.e. Newtonian) mechanics, he estimated the radius of such an object, which is identical to the well-known Schwarzschild radius for a black hole. However, he considered objects of density similar to that of the Sun, which required the radius of the object to exceed 500 $R_\odot$, and consequently the mass to be $\gtrsim 10^8$ $M_\odot$[1]. He also suggested that such an object would not be directly observable, but if it was part of a binary system, one could detect it by its gravitational pull on the companion star.

In a contemporary, but seemingly unrelated (Gillispie, 1997) incident, the noted French scientist Pierre Simon Laplace proposed (Laplace, 1796) and, three years later, proved mathematically (Laplace, 1799) an almost identical possibility, although he considered objects with the density of the Earth, and hence only required half the radius that the argument by Michell (1784) necessitated.

These two proofs are discussed in more detail, together with some historical perspective, by Montgomery et al. (2009). It appears, however, that neither of the two scientists believed that such objects could exist, so they only presented them as mathematical curiosities. No further developments of these models are known. Today, these theoretical constructs are called "dark stars", in order to distinguish them from the better-known general relativistic black holes.

1.1.2 General relativity

The modern definition of a black hole stems from the early days of the general theory of relativity (GR). When Einstein (1915) published the well-known field equations relating the presence of matter to the curvature of the spacetime around it, Schwarzschild (1916) presented the first solution only a year later. This solution, which soon became known as the Schwarzschild metric, describes the spacetime around a stationary, spherically symmetric, non-spinning distribution of matter of mass M:

$$\mathrm{d}s^2 = \left(1 - \frac{2GM}{rc^2}\right) c^2 \mathrm{d}t^2 - \frac{\mathrm{d}r^2}{1 - \frac{2GM}{rc^2}} - r^2 \mathrm{d}\Omega^2, \tag{1.1}$$

where $\mathrm{d}s$ is the spacetime distance between two events, G is the gravitational constant, c is the speed of light and Ω is the solid angle. One particularly interesting aspect of the

---

[1] $R_\odot \simeq 7 \times 10^{10}$ cm is the radius of the Sun and $M_\odot \simeq 2 \times 10^{33}$ g is its mass

solution is that at a radius $R = 2GM/c^2$, called the Schwarzschild radius, there is a singularity in the radial component of the metric, i.e. the radial component becomes infinite. For a while, it was considered to be a problem of GR, however only a conceptual one, as all astrophysical bodies known at the time were much larger than their Schwarzschild radii. Furthermore, Lánczos (1922) showed that singularities may be introduced into the Schwarzschild metric by changing the coordinate system, and Lemaître (1933) found a coordinate transformation that would make the singularity present in the Schwarzschild metric vanish. Therefore it was accepted that the singularity at the Schwarzschild radius is coordinate-dependent.

Nevertheless, the coordinate singularity has a physical meaning. It represents a "surface" through which matter can enter, but not leave, as for any particle at or inside the Schwarzschild radius, the future light-cone (i.e. the set of possible locations a particle can move to in space-time) points only toward the centre of the matter distribution. This "event horizon" is one of the key properties of a black hole.

In subsequent decades, other solutions to the Einstein field equations were discovered. Several among them can also correspond to black holes, such as the Kerr (1963) metric representing a rotating uncharged spherically symmetric matter distribution, as well as two metrics for charged black holes. The Kerr metric, obviously, reduces to the Schwarzschild metric in the limit of no rotation. The "no-hair" conjecture (Carter, 1973; Misner et al., 1973) states that only the three externally observable parameters, i.e. mass, angular momentum and charge, are necessary to fully describe a black hole. In an astrophysical context, a black hole is not expected to have significant electric charge (a charged black hole would preferentially accrete particles of the opposite charge and so its charge would fluctuate around zero), therefore the Kerr metric can be considered the most general solution of an astrophysical black hole.

1.1.3 Astrophysical black holes

For several decades after GR was formulated, astronomers considered black holes to be mere mathematical curiosities, rather than corresponding to any physical objects. Perhaps the first change to this received wisdom occurred in the late 1960s, when neutron stars were discovered. Previously these had also been considered only theoretical objects. The proof of the existence of this class of exotic objects led scientists to reconsider the possibility of black holes, especially given earlier theoretical calculations for the maximum mass of neutron stars, the Tolman-Oppenheimer-Volkoff limit (Tolman, 1939; Oppenheimer and Volkoff, 1939). After all, if white dwarfs were not the limit of how extreme (in terms of density and gravitational attraction) astrophysical bodies could become, neutron stars should not be the limit either. As no other form of matter with higher degenerate pressure than pure neutron "soup" was known at the time, black holes seemed the inevitable end

state of objects that retained more than 3 $M_\odot$ of material once they had lost all radiative pressure support.

Even then, a significant obstacle to the discovery and acceptance of black holes as real astrophysical objects was the uncertainty of what observable features one might expect to obtain from them. As these objects do not emit electromagnetic radiation (Zel'Dovich and Novikov, 1971), alternative evidence of their existence had to be sought. Much like Michell and Laplace almost two hundred years earlier, scientists in the middle of the 20th century thought that black holes may be detected by the gravitational effects on companion stars in binary systems, and perhaps by significant dimming of companion stars if the binary is eclipsing.

A true revolution in thinking came with the seminal paper by Shakura and Sunyaev (1973), which showed that black holes in binary systems may be expected to create a spectrum vastly different from that of a star. Such spectral features are generally caused by the macroscopic distribution of matter stripped from the companion star and accreting on to the black hole, a process which was already known to produce copious amounts of energy (Salpeter, 1964; Zel'Dovich, 1964). The gas distribution, composed of a relatively cold thin accretion disc with a hot corona, allows for production of a significant amount of X-rays, so that black holes should outshine the companion stars in this region of the spectrum. Even in the other radiation bands, the energy liberated by matter accretion may be large enough to provide significant observable luminosity. Spectral information would then allow one to identify a member of a binary system as an accreting object, which should be a black hole if its mass exceeds the upper limit of neutron star masses.

With this new understanding that black holes may, in fact, be luminous and that accretion may provide a lot of energy, came a new hypothesis on the power source of quasars. These "quasi-stellar objects", known since the 1950s (e.g. Edge et al., 1958, 1959), had been identified as extremely distant in 1962, following observations of the radio source 3C 287 and its identification with an optical counterpart (Schmidt, 1963; Matthews and Sandage, 1963; Schmidt, 1962). At these cosmological distances, quasars had to be the brightest known objects in the Universe, but the source of this immense power remained a mystery. Accretion of matter on to black holes offered a possible explanation. Early investigations of this possibility (Salpeter, 1964) culminated with the paper by Soltan (1982), which showed that given the luminosity density of quasars, they are very likely powered by accretion on to supermassive black holes. Furthermore, it predicted that most large galaxies today should harbour dormant supermassive black holes in their centres, corroborating earlier claims to that effect (Lynden-Bell, 1969).

While a compelling theoretical argument, Soltan's paper presented another challenge. It had been known that stellar mass black holes may form during the death of massive stars, and that their masses should range from $\sim$ 3 $M_\odot$ (the Tolman-Oppenheimer-Volkoff

limit) to $\sim 30-100$ M$_\odot$ (mass of the cores of the most massive stars). In order to power the emission from quasars, black holes had to have masses equal to millions or even billions of M$_\odot$. The origin of these supermassive black holes (SMBHs) became a puzzle which has not been solved to this day, despite numerous hypotheses and models, ranging from prolonged gas accretion on to initially stellar mass black holes (King and Pringle, 2006), to black hole mergers and star captures in globular clusters (Spitzer, 1987) to direct collapse of massive gas pockets in primordial environments (Begelman et al., 2006). For now, the two classes of black holes - stellar and supermassive - remain distinct in terms of their astrophysical origin, properties and areas of relevance to other astrophysical problems.

1.1.4   Observational evidence of black holes

Even though Shakura and Sunyaev (1973) give predictions for a number of observable black hole emission properties, which have later been examined in more detail by other authors (e.g. Pringle, 1981; Papaloizou and Lin, 1995; Lin and Papaloizou, 1996; Balbus, 2003), these only provide indirect evidence of their existence. A black hole itself may only be imaged, much like it had been envisaged before the 1970s, by the shadow that its event horizon casts on the light from background objects or its own accretion flow obscured by the shadow of the event horizon. Resolving the event horizon of a black hole is a formidable task, and it is only in the last decade that the first dedicated attempts to do so have been carried out (e.g. Falcke et al., 2000; Fish et al., 2011), without definite success.

The indirect evidence comes, as predicted by Shakura and Sunyaev (1973), from X-ray emission and variability on timescales comparable to the dynamical timescale, $t_{\mathrm{d}} =$ a few seconds or less, at the event horizon. The first source to be widely accepted as being powered by accretion on to a black hole is Cygnus X-1 (Bowyer et al., 1965; Rothschild et al., 1974), with many other Galactic sources following in subsequent years. Strong evidence for the existence of supermassive black holes came from gravitationally redshifted emission of the Fe Kα line (Tanaka et al., 1995) and a number of high-resolution observations of stellar and gas kinematics (e.g. Harms et al., 1994; Kormendy and Richstone, 1995). The supermassive black hole of our own Galaxy, Sgr A* (Balick and Brown, 1974), has been identified via numerous channels, including emission spectrum and its variability (Falcke et al., 1993; Baganoff et al., 2003; Genzel et al., 2003a), small geometric size obtained with interferometric observations (Krichbaum et al., 1993, 1998) and, most clearly, by monitoring stellar orbits in the central parsec of the Galaxy (Schödel et al., 2002; Ghez et al., 2005, 2008). See Section 1.5 for more details on observations of the Galactic centre.

For the time being, black holes of all varieties remain elusive to direct detections, but this may change in the upcoming decade. Nevertheless, the vast amounts of indirect evidence have convinced practically all astronomers of their existence. As a result, they

have become a regular type of object for astrophysical studies, and numerous properties of their immediate and more distant environs have been investigated since the end of the last century. In the next Section, I will briefly review observational evidence for a connection between supermassive black holes and their host galaxies, before moving on to a physical model describing this connection.

1.2 Relations between black holes and their host galaxies

The Soltan (1982) argument mentioned above connects the space density of the background light emitted by quasars to the space density of supermassive black holes today. It turns out that most, and possibly all, large (stellar mass $M_* \gtrsim 10^{10}$ M$_\odot$) galaxies harbour supermassive black holes at their centres (Lynden-Bell, 1969; Kormendy and Richstone, 1995; Magorrian et al., 1998; Merritt and Ferrarese, 2001). This correspondence has led astrophysicists to ponder the possibility of links between the properties galaxies and the supermassive black holes contained therein. The majority of such investigations consider only the mass of the SMBH, because the angular momentum is very difficult to measure; however, some work on the expected evolution of SMBH spin with cosmic time has been done (e.g. King et al., 2005; Berti and Volonteri, 2008), often yielding very different results.

In the past ~ 15 years, a number of observational campaigns and investigations revealed several important and somewhat unexpected correlations between SMBHs and their host galaxies (more precisely, their spheroidal components). Magorrian et al. (1998), using data of 36 nearby galaxies and following on from earlier investigations (Kormendy and Richstone, 1995), found that the central massive object masses are almost linearly proportional to the masses of stellar bulges, giving what is now known as the Magorrian relation: $M_{\rm BH}/M_{\rm b} \simeq 0.002$, valid over more than two orders of magnitude in either mass. This relation is sometimes presented in a more observationally direct way, relating the SMBH mass with the *luminosity* of the host spheroid. This latter relation typically has a slope slightly steeper than linear (e.g. ~ 1.11 in Gültekin et al., 2009), due to the fact that more luminous galaxies also tend to have higher mass-to-light ratios (Magorrian et al., 1998). The relation has since been refined by various studies, suggesting that the slope is somewhat super-linear even when bulge masses are considered (e.g. Häring and Rix (2004) found $M_{\rm BH} \propto M_{\rm b}^{1.12}$, while Laor (2001) calculated an even steeper slope $M_{\rm BH} \propto M_{\rm b}^{1.53}$). The overall scatter in the relation is ~ 0.45 dex (Magorrian et al., 1998; Marconi and Hunt, 2003), but the intrinsic scatter is probably as low as ~ 0.3 dex (Gültekin et al., 2009).

There have also been studies of the evolution of the relation with redshift, generally finding that SMBHs were comparatively more massive at higher redshift, suggesting a delay between the growth of SMBHs and the growth of bulges (Shields et al., 2006; Peng

et al., 2006; McLure et al., 2006; Greene et al., 2010b; Targett et al., 2012) or that SMBHs formed as massive seeds but their subsequent growth did not keep up with the growth of their host galaxies (Koushiappas et al., 2004; Begelman et al., 2006). On the other hand, some authors found a lack of redshift evolution, suggesting various selection biases as a possible reason for why some differences between low-redshift and high-redshift galaxies seem present (e.g. Shields et al., 2003; Schulze and Wisotzki, 2011).

Another, potentially more important and revealing, correlation was discovered in 2000 (Ferrarese and Merritt, 2000; Gebhardt et al., 2000a) and connects the SMBH mass with the velocity dispersion in the host galaxy spheroid. This relation is usually given as $M \propto \sigma^\alpha$. The value of α has been estimated by different authors, using different galaxy samples, SMBH mass estimation techniques, etc., to be anywhere between ~ 3.6 and ~ 5 (e.g. Graham, 2008; Gebhardt et al., 2000b; Tremaine et al., 2002; Ferrarese and Merritt, 2000, in order of increasing α). The relation has also been refined several times, extending the range of σ to values as low as ~ 40 km/s (Ferrarese et al., 2006; Greene et al., 2010a) and as high as ~ 350 km/s (McConnell et al., 2011). The scatter in the relation is generally found to be ~ 0.25 dex (Tremaine et al., 2002), slightly lower than in the $M_{\mathrm{BH}} - M_{\mathrm{b}}$ relation, likely hinting at a more fundamental nature (Gültekin et al., 2009); however, there have been claims that the intrinsic scatter in both relations is similar (Marconi and Hunt, 2003).

Both relations rely significantly on resolving the SMBH sphere of influence, $R_{\mathrm{infl}} = GM_{\mathrm{BH}}/2\sigma^2$, to calculate the SMBH mass (other measurements, such as reverberation mapping, are usually only useful for active galaxies (Peterson, 1993, 1997)). This process induces a possible bias, where for a given σ, some black holes may be missed if they are significantly below the formal $M - \sigma$ relation. As a result, Batcheldor (2010) recently suggested that the $M - \sigma$ relation may be only an upper limit. However, statistical analysis of available samples seems to disfavour such an interpretation, at least for early-type galaxies (Gültekin et al., 2011).

Certain other correlations between SMBH mass and host galaxy parameters have also been discussed in the literature, such as the kinetic energy of random motions in the galaxy (Feoli and Mancini, 2009; Mancini and Feoli, 2012) and the gravitational binding energy of the bulge (Aller and Richstone, 2007). Hopkins et al. (2007) even found a fundamental plane for SMBHs, similar to that of elliptical galaxies. Properties of the galaxy outside of the spheroidal component, i.e. those of the disc or the dark matter halo, do not seem to correlate with the black hole mass (Kormendy et al., 2011; Kormendy and Bender, 2011). This implies that there is a relation between the growth of bulges and their black holes, but not between SMBHs and other components of galaxies.

The nature of this connection has been a subject of many analytical (e.g. Silk and Rees, 1998; King, 2003, 2005; Murray et al., 2005) and numerical (e.g. Di Matteo et al.,

2005; Booth and Schaye, 2009) investigations. While some models attempt to explain the correlations as being due to qualitatively similar evolution of both SMBHs and host galaxy spheroids (e.g. Treister et al., 2011; Devecchi et al., 2010), the majority of researchers seem to agree that a physical connection between the evolution of the two types of object is required in order to explain the tightness of the correlations. This mechanism is most likely some form of SMBH feedback (Alexander and Hickox, 2012).

There is currently no universal agreement regarding the nature of this feedback, nor on its precise details. One of the dominant models for explaining this connection is the wind feedback model, first proposed by King (2003) in connection with the then-recent observations of wind emanating from several active galactic nuclei (AGN; Pounds et al., 2003a,b; King and Pounds, 2003). Investigation of several properties of this model form the major part of this Thesis. In the next Section, I present the basic properties of the wind feedback model before moving on to describe the ways it can be simulated numerically.

1.3 Wind feedback model

1.3.1 Basic constraints

There are several properties of galaxies, both directly observed and easily inferred using basic physics, that any model of SMBH-galaxy co-evolution must satisfy in order to be viable. First and foremost, any feedback from the black hole on its host cannot be grav-itational. The sphere of influence of an SMBH, defined as the region where its gravity dominates over that of the background stellar distribution, is small, $R_{\rm infl} \simeq 5 M_8 \sigma_{200}^{-2}$ pc, where M_8 is the black hole mass in 10^8 M$_\odot$ and σ_{200} is the velocity dispersion of the host in units of 200 km/s. Therefore the bulge in general does not feel the gravity of the SMBH.

On the other hand, the feedback can be energetic. If the SMBH gained most of its mass during luminous accretion (Soltan, 1982), then the amount of energy liberated is

$$\Delta E \simeq \eta M_{\rm BH} c^2 \simeq 2 \times 10^{61} M_8 \text{ erg,} \tag{1.2}$$

where $\eta \simeq 0.1$ is the radiative efficiency of accretion, which only depends on the spacetime metric around the black hole and is never very different from the fiducial value for luminous thin-disc accretion (Shakura and Sunyaev, 1973). In comparison, the binding energy of a galaxy bulge is typically

$$E_{\rm b} \simeq M_{\rm b} \sigma^2 \simeq 8 \times 10^{58} M_{11} \sigma_{200} \text{ erg,} \tag{1.3}$$

where M_{11} is the bulge mass in 10^{11} M$_\odot$. It is clear that a black hole releases more than enough energy to completely unbind the bulge and even the whole galaxy ($M_{\rm gal} \sim 10^{13} - 10^{14}$ M$_\odot$). This immediately implies that since we only observe correlation between

the spheroid and the SMBH, the black hole accretion energy *cannot* be efficiently coupled to
the bulge gas, otherwise black holes would only grow to much lower masses than observed
before they unbind the bulges, removing their own long-term fuel supply.

The low observed scatter in the $M - \sigma$ relation suggests another constraint on the
feedback: its effects must manifest rapidly. If the process caused by injection of accretion
energy is very slow to remove the gas from the surroundings of the SMBH, the black hole
activity would have to last for a long time, strongly dependent on the size of the bulge, and
one would expect a lot of scatter in the final SMBH mass for a given value of σ. Similarly,
if feedback is to be implicated in causing the transition of galaxies from the blue cloud
to the red sequence, the dearth of galaxies in the intermediate "green valley" (Schawinski
et al., 2007) zone also suggests that the feedback is rapid.

Finally, observations reveal that black holes seem to grow ahead of their bulges (Targett et al., 2012), but both AGN activity and star formation activity decline with cosmic
time (Watson et al., 2009). The mean SMBH mass in an active galaxy was larger in
the past (Vestergaard and Osmer, 2009; Örndahl et al., 2003; Schawinski et al., 2010).
Similarly, star formation in more massive galaxies happened at larger redshift (e.g. Treu
et al., 2005). This "downsizing" may be at least partially explained as a natural consequence of hierarchical cosmological structure formation (Neistein et al., 2006), but there
are tentative indications that other processes may be responsible (Cimatti et al., 2006).
If SMBH feedback is responsible for shutting off both quasar activity and star formation,
as suspected, the model should also explain the downsizing phenomenon.

1.3.2   Basis of the model: AGN winds

Over the past decade, observations of blueshifted high-ionisation iron absorption lines
revealed fast ($v_{\mathrm{w}} \sim 0.1c$), quasi-spherical winds (Pounds et al., 2003a,b), present in a
large fraction of nearby active galaxies (Tombesi et al., 2010a,b). The winds have mass
outflow rates comparable with the Eddington accretion rate (King and Pounds, 2003) and
momentum outflow rates rather similar to

$$\dot{M} v_{\mathrm{w}} = \frac{l L_{\mathrm{Edd}}}{c},\qquad(1.4)$$

where

$$L_{\mathrm{Edd}} = \frac{4\pi G M_{\mathrm{BH}} c}{\kappa}\qquad(1.5)$$

is the Eddington luminosity of the black hole, calculated by requiring that the radiation
pressure force on the electrons in an accretion flow would just compensate the gravitational attraction of the SMBH; l is a ratio between the actual SMBH luminosity and the
Eddington limit. During periods of quasar activity, black holes are expected to reach $l \simeq 1$
(Steinhardt and Elvis, 2010; King, 2010a). However, they cannot have significantly larger

accretion rates, as those would surpass the upper limit set by the dynamical infall rate in the galaxy at large (King, 2010b); as a result, the AGN luminosity is close to L_{Edd} during quasar phases.

The wind is launched from the radius at which the local accretion rate through the thin disc exceeds the Eddington limit of the SMBH (possibly corrected to account for accretion disc gravity) and so one would expect some variation in both the $\dot{M}$ and v_{w}. Observations reveal a spread of wind velocities between $\sim 0.03c$ and $\sim 0.3c$ (Tombesi et al., 2010a,b), and the spread in $\dot{M}$ around $\dot{M}_{\mathrm{Edd}}$ is of the same order. From a theoretical standpoint, equation 1.4 together with the definition of accretion luminosity $L = \eta \dot{M} c^2$ give the wind velocity $v \simeq \eta c = 0.1c$, where η is the radiative efficiency of accretion (King, 2010b; Frank et al., 2002). Such winds have high ionisation levels due to their low density:

$$\xi_{\mathrm{w}} = \frac{L}{nR^2} = \frac{L_{\mathrm{Edd}} \times 4\pi v_{\mathrm{w}} \mu m_{\mathrm{p}}}{\dot{M}_{\mathrm{w}}} = 4\pi \mu m_{\mathrm{p}} \eta^2 c^3 \simeq 4 \times 10^6, \tag{1.6}$$

where μm_{p} is the mean particle mass in the wind. This explains the observed hydrogen- and helium-like iron lines (FeXXV and FeXXVI) in their spectra.

1.3.3 Wind shock

The SMBH wind, launched from the inner parts of its accretion disc, blows approximately radially in a spherically symmetric bubble with an almost constant velocity, until it reaches the ambient gas. As the wind is highly supersonic, a strong shock develops, where the wind is thermalised to a temperature

$$T_{\mathrm{sh}} \simeq \frac{3 m_i v_{\mathrm{w}}^2}{16 k_{\mathrm{B}}} \sim \begin{cases} 10^{10} \ \mathrm{K} & \text{for protons,} \\ 10^7 \ \mathrm{K} & \text{for electrons;} \end{cases} \tag{1.7}$$

here k_{B} is the Boltzmann constant and $m_i = m_{\mathrm{p}}$ or m_{e}, depending on the particles considered and assuming rapidly established energy equipartition for each species. The shocked wind becomes an extremely hot bubble which attempts to expand and lift the ambient medium.

The efficiency of this expansion depends crucially on how rapidly the shocked wind loses its thermal energy due to non-adiabatic processes, i.e. cooling. The only form of cooling efficient at such high temperatures is the inverse Compton process (Ciotti and Ostriker, 1997). The Compton equilibrium temperature (Rybicki and Lightman, 1979) is $T_{\mathrm{C}} \sim 2 \times 10^7$ K, so the wind particles can give up their energy to the background AGN radiation field. The timescale for cooling, assuming that the protons and electrons reach thermal equilibrium rapidly, depends on the density of the radiation field (cf. King, 2003):

$$U_{\mathrm{rad}} = \frac{L_{\mathrm{Edd}}}{4\pi R^2 c}, \tag{1.8}$$

neglecting the possible small correction due to non-spherical geometry of the wind (and the radiation field). The relativistic Compton cooling timescale for an electron of initial energy E is then

$$t_\mathrm{C} = \frac{3m_\mathrm{e}c}{8\pi\sigma_\mathrm{T}U_\mathrm{rad}}\frac{m_\mathrm{e}c^2}{E}, \tag{1.9}$$

where σ_T is the Thomson scattering cross section. Substituting the values for the post-shock electron energy (based on eq. 1.7), the radiation density (eq. 1.8) and the Eddington luminosity (eq. 1.5) I find

$$t_\mathrm{C} = \frac{2}{3}\frac{cR^2}{GM_\mathrm{BH}}\left(\frac{m_\mathrm{e}}{m_\mathrm{p}}\right)^2\left(\frac{c}{v_\mathrm{w}}\right)^2 \simeq 10^7\, R_\mathrm{kpc}^2\, M_8^{-1}\ \mathrm{yr}. \tag{1.10}$$

If I drop the assumption of rapidly established thermal equilibrium, then this cooling timescale must be compared with the electron-ion collisional equilibration timescale. Faucher-Giguère and Quataert (2012) recently investigated this issue and found that accounting for the equilibration increases the cooling timescale by $1-2$ orders of magnitude, depending on wind properties. The conclusions of the work presented in this Thesis are, however, unchanged by accounting for this effect.

It is immediately obvious that the Compton cooling timescale increases with radius faster than the dynamical timescale $t_\mathrm{dyn} \simeq R/\sigma \simeq 5\times10^6 R_\mathrm{kpc}\sigma_{200}^{-1}$ yr. However the latter is longer than the former in the central few hundred parsecs of a galaxy. Therefore, in the central regions, one may expect that the shocked wind radiates its energy away much more rapidly than it can transfer it to the surrounding interstellar medium. Subsequent calculations (see Section 1.3.4 below) confirm the validity of this assumption. In this case, the ambient gas only feels the ram pressure of the wind. The acceleration due to ram pressure force is equal to the wind momentum flow rate (eq. 1.4). This creates a mild outflow, which is called a momentum-driven flow.

1.3.4 Momentum-driven flow

The properties of a momentum-driven flow have been studied extensively previously (King, 2003, 2005, 2010b). Here I briefly summarise them and refer the reader to these three papers for more details.

The equation of motion of a spherically symmetric outflowing shell is

$$\frac{\mathrm{d}}{\mathrm{d}t}\left[M(R)\dot{R}\right] + \frac{GM(R)\left[M_\mathrm{BH} + M_\mathrm{tot}(R)\right]}{R^2} = 4\pi\rho_\mathrm{w}v_\mathrm{w}^2 = \frac{lL_\mathrm{Edd}}{c} \tag{1.11}$$

where

$$M(R) = 4\pi\int_0^R \rho_\mathrm{g}r^2\mathrm{d}r \tag{1.12}$$

is the swept–up interstellar gas mass, M_BH is the black hole mass, $M_\mathrm{tot} = M(R)/f_\mathrm{g}$ is the

total mass within radius R (including any stars and dark matter), $f_g = \rho_g/\rho_{tot}$ is the gas fraction relative to all matter (note that it is assumed here that the density of both gas and the background potential follow the same radial profile) and ρ_g and ρ_{tot} are the gas and background potential densities, respectively. The two terms on the left hand side of eq. (1.11) represent the change in the momentum of the swept up shell and the weight of that shell, respectively.

The dynamics of the shell qualitatively depend on the distance to the black hole. Inside the sphere of influence, the dominant contribution to the gravitational attraction comes from the SMBH and the equation of motion becomes

$$\frac{d}{dt}\left[M(R)\dot{R}\right] + \frac{GM(R)M_{BH}}{R^2} = \frac{L_{Edd}}{c}. \tag{1.13}$$

Integrating the equation once (see King, 2010b, for details) shows that the maximum mass a black hole can lift out of its own gravitational potential is

$$M(R) = \frac{4\pi R^2}{\kappa}. \tag{1.14}$$

This is equivalent to saying that the Thomson optical depth of the flow, $\tau = \kappa M(R)/4\pi R^2 \lesssim 1$. If this condition is not satisfied, the flow stalls and collapses, continuing to feed the SMBH until such time that the ambient gas density decreases enough for the outflow to resume (note that the condition 1.14 does not depend on the black hole mass). Thus the outflow is self-regulating to have Thomson optical depth of $\simeq 1$.

Far away from the SMBH, one can neglect the gravity of the black hole in the equation of motion. One also needs some prescription for $M(R)$. A simple, analytically tractable mass profile, which nevertheless is a reasonable approximation to gas in real galactic spheroids, is that of a singular isothermal sphere. This profile has a density distribution

$$\rho_g = \frac{f_g \sigma^2}{2\pi G R^2}; \tag{1.15}$$

the corresponding enclosed mass is

$$M(R) = \frac{2 f_g \sigma^2 R}{G}. \tag{1.16}$$

Substituting this into eq. (1.11), integrating twice and rearranging, I find

$$R^2 = \left[\frac{GL_{Edd}}{2 f_g \sigma^2 c} - 2(1 - f_g)\sigma^2\right] t^2 + 2R_0 v_0 t + R_0^2, \tag{1.17}$$

where R_0 and v_0 are boundary conditions corresponding to the flow properties during the transition between the sphere of influence and larger radii. The sign of the term within

the square brackets determines whether the outflow can continue indefinitely (provided that the AGN is still luminous). From the condition that the term is positive, substituting the expression for $L_{\rm Edd}$, I derive the major prediction of the model:

$$M_{\rm BH} \geq M_\sigma = \frac{f_{\rm g} \kappa}{\pi G^2} \sigma^4 \simeq 3.68 \times 10^8 \sigma_{200}^4 \ {\rm M_\odot}, \tag{1.18}$$

using the cosmological gas fraction $f_{\rm g} = f_{\rm c} = 0.16$. Physically, this means that an outflow can only expand to large radii if $M_{\rm BH} > M_\sigma$. This predicted relation has both the slope and the intercept remarkably similar to the observed $M - \sigma$ relation, despite having no free parameter.

When the condition $M > M_\sigma$ is satisfied, I may make another simplifying assumption that only the radiative driving term is important in eq. (1.17) and calculate the velocity of a momentum-driven outflow, using eq. (1.18) to simplify the expression:

$$v_{\rm m} \simeq \frac{R}{t} \simeq \left(\frac{G L_{\rm Edd}}{2 f_{\rm g} \sigma^2 c} \right)^{1/2} \simeq \sqrt{2} \sigma \left(\frac{M_{\rm BH}}{M_\sigma} \right)^{1/2}, \tag{1.19}$$

which can be used to define the flow timescale $t_{\rm flow} = R/v_{\rm m}$. Combining this expression with that for the Compton cooling timescale (eq. 1.10), I find a cooling radius for efficient IC cooling:

$$
\begin{aligned}
R_{\rm C} &\simeq \frac{3 G M_{\rm BH}}{2c} \left(\frac{m_{\rm p}}{m_{\rm e}} \right)^2 \left(\frac{v_{\rm w}}{c} \right)^2 \left(\frac{f_{\rm g} \kappa \sigma^2}{2\pi G^2 M_{\rm BH}} \right)^{1/2} \\
&\sim 520 \ \sigma_{200} \ M_8^{1/2} \ v_{0.1}^2 \left(\frac{f_{\rm g}}{f_{\rm c}} \right)^{1/2} \ {\rm pc}.
\end{aligned}
\tag{1.20}
$$

This finding shows that the earlier assumption (Section 1.3.3) of a momentum-driven outflow in the central regions of the galaxy is justified.

The energy flow rate (i.e. "kinetic luminosity") of the momentum-driven flow can be calculated by combining its linear momentum rate (equal to the wind momentum outflow rate) and $v_{\rm m}$, an expression for which may then be substituted from eq. (1.19):

$$\dot{E}_{\rm m} = \frac{\dot{p}_{\rm w} v_{\rm m}}{2} = \frac{L_{\rm Edd} v_{\rm m}}{2c} \simeq \frac{\sigma}{\sqrt{2} c} \left(\frac{M_{\rm BH}}{M_\sigma} \right)^{1/2} L_{\rm Edd} \simeq 5 \times 10^{-4} \sigma_{200} \left(\frac{M_{\rm BH}}{M_\sigma} \right)^{1/2} L_{\rm Edd}, \tag{1.21}$$

where I also used eq. (1.18) to parametrise the SMBH mass. It is evident that the coupling between the luminosity of the SMBH and a momentum driven outflow is very inefficient, as required by the basic constraints (cf. Section 1.3.1).

1.3.5 Energy-driven flow

Energy-driven outflows occur when the contact discontinuity between the wind and the ambient ISM moves beyond the cooling radius (eq. 1.20). In this regime, most of the thermal energy in the shocked wind bubble is lost to adiabatic expansion, further inflating the bubble. The energy flow rate of the system then becomes equal to the energy flow rate of the wind:

$$\dot{E}_{\rm en} = \frac{\eta L_{\rm Edd}}{2} = 0.05 L_{\rm Edd} = \frac{\eta c}{v_{\rm m}} \dot{E}_{\rm m} \sim 100 \sigma_{200}^{-1} \dot{E}_{\rm m}. \tag{1.22}$$

This coupling is much more efficient and one may expect that the outflow is accelerated to a much greater velocity. Indeed, King (2005) derived an equation of motion for this flow in the case of an isothermal potential (eq. 1.15) and found that the outflow, when driven, rapidly (in a few $\times 10^5$ yr) accelerates to a velocity $v_{\rm e} \sim 900$ km/s $\sim 4.5\sigma$ in the case of $f_{\rm g} = f_{\rm c}$. The properties of energy-driven flows are discussed in more detail in Chapters 2 and 4 of this Thesis.

1.4 Numerical simulations

Analytical investigation of AGN wind feedback, and more generally of gas flows around SMBHs, is very useful in order to understand the general behaviour. However, quantitative predictions (and in some cases even qualitative details) obtained by such calculations often lack precision due to the necessity of making a number of assumptions so that the equations become tractable. In such cases, numerical hydrodynamical simulations are often employed to get a more detailed picture of the processes occurring in these astrophysical environments.

In this Thesis, I have used an astrophysical simulation code GADGET-3, an updated version of the public code GADGET-2 (Springel, 2005). The code uses a hybrid implementation of N-body algorithms to track non-hydrodynamic particles (such as dark matter or stars) and the Smoothed particle hydrodynamics (SPH) formalism for the gas particles, with feedback implemented via the "virtual particle" method of Nayakshin et al. (2009a). I describe each of these in turn.

1.4.1 N-body algorithms

1.4.1.1 Force calculation and softening

Gravitational interactions between particles in GADGET are followed using N-body algorithms. The term describes a large class of numerical techniques used to follow the motions of particles under the influence of long-range forces. In particular, GADGET employs the collisionless N-body formalism, which means that close encounters between

two particles are not considered important. This allows softening of the force of gravity, that is, the actual attractive force between any two particles tends to a constant value when the distance between them becomes less than the softening length ε. In the version of GADGET that is used in the simulations presented in this Thesis, the gravitational softening function is closely linked to the SPH smoothing kernel (see Section 1.4.2 below) and is expressed as

$$W_{\mathrm{gr}}(r,h) = \frac{8}{\pi h^3} \begin{cases} 1 - 6\left(\frac{r}{h}\right)^2 + 6\left(\frac{r}{h}\right)^3, & 0 \leq \frac{r}{h} \leq \frac{1}{2}, \\ 2\left(1 - \frac{r}{h}\right)^3, & \frac{1}{2} < \frac{r}{h} \leq 1, \\ 0, & \frac{r}{h} > 1, \end{cases} \tag{1.23}$$

where r is the distance between the two particles and h is the SPH smoothing length, here taken to be equal to 2.8ε. This softening represents the assumption that the number of simulated particles is much smaller than the number of actual particles in the system, i.e. $N_{\mathrm{sim}} \ll N_{\mathrm{real}}$, and that the distribution of the latter is inherently smooth. This assumption is warranted in the simulations performed in this Thesis.

1.4.1.2   Tree method for force calculation

In principle, the force calculation requires one to calculate the interaction between every pair of particles, the number of which scales as N^2 and is therefore highly computationally expensive. However, it is possible to use certain techniques to overcome this problem. The particular method employed in GADGET is the TreePM, or Tree-Particle-Mesh, algorithm, which scales as $N\log N$ for large N, but preserves accurate force calculations at small distances. The method has been described extensively in the literature (e.g. Bode et al., 2000; Bagla and Ray, 2003) and its implementation into GADGET has been presented in Springel (2005); here I only provide a brief qualitative overview.

The cornerstone of this approach is a split of the computational domain into cubical cells: eight in the first iteration, encompassing the whole particle distribution, with subsequent division of each cell into eight daughter cells, if needed, until finally each cell contains only one particle. Then, for each particle, the code "walks the tree", starting from the "root node" of the largest cells and, if necessary, walking "up the branches" to ever smaller cells. At each cell, the code checks whether the gravitational force approximated between the target particle and the whole mass distribution of the cell in question is accurate enough (given some condition for accuracy). If it is, the approximation is used and smaller daughter cells are not considered. If the accuracy is not good enough, the code moves to the daughter cells and checks each of those in turn. For the smallest cells, called "leaves", the force between the cell and the target particle is exactly the force between the two particles, so it is accurate to within the errors caused by the force smoothing. Overall,

this approach allows the gravitational force from distant particles to be approximated by the ensemble average of those particles (essentially employing Newton's second theorem; Section 2.2.1 of Binney and Tremaine 2008), while the forces from nearby particles are still computed via full two-body interactions, only attenuated by softening.

1.4.2   Smoothed particle hydrodynamics

Smoothed particle hydrodynamics is a numerical method used to investigate the hydrodynamics of fluids by following the motion of a number of interpolation points - the "smoothed particles" of the title - that are implicitly assumed to fairly sample a smooth physical fluid. The method was invented by Lucy (1977) and Gingold and Monaghan (1977). Since the 1970s the method has been extensively developed and adapted to a variety of astrophysical (and engineering) problems, from stellar evolution to cosmology. A number of excellent reviews of the subject exist (e.g. Monaghan, 1992; Springel, 2010; Price, 2012), and I refer the reader to those for a detailed overview of the SPH algorithms. Below, I only present the most fundamental concepts of SPH and make a few remarks on their implementation in GADGET.

1.4.2.1   Calculating density

As mentioned above, SPH is concerned with following motions of fluids by tracking the motion of interpolation points. The connection between the two requires us to be able to calculate properties of the smooth fluid from the properties of the point particles. The fundamental property, upon which most SPH implementations are based, is the fluid density. It is calculated from the following equation:

$$\rho(\boldsymbol{r}) \simeq \sum_i m_i W_{\mathrm{SPH}}(|\boldsymbol{r} - \boldsymbol{r}_i|, h), \qquad (1.24)$$

where $\boldsymbol{r}$ is a coordinate vector of any point in the fluid (in general not coincident with an interpolation point), m_i is the mass of the ith particle, $\boldsymbol{r}_i$ is the particle's position, and $W_{\mathrm{SPH}} = W_{\mathrm{SPH}}(|\boldsymbol{r}|, h)$ is an SPH smoothing kernel. In GADGET, the form of W_{SPH} is identical to W_{gr} (equation 1.23), but this does not generally have to be the case. The smoothing kernel between the positions of two particles i and j is quite often written, for compactness, as $W_{ij}(h) = W_{ji}(h)$.

The smoothing length is usually different for each particle, chosen to produce the desired number of neighbours ($N_{\mathrm{ngb}} = 40$ in the simulations presented in this Thesis and similar numbers for other implementations using the cubic spline kernel). It is calculated by requiring that the mass contained within the volume of a sphere of radius h should be

constant:

$$h_i = \left(\frac{3N_{\mathrm{ngb}}m}{4\pi\rho_i}\right)^{1/3}, \tag{1.25}$$

where it is assumed that all particles have the same mass m (this is standard in SPH). The two equations (1.24) and (1.25) are coupled, therefore finding consistent values for ρ and h requires iteration. Once the smoothing lengths for all particles are known, all properties of the underlying fluid can be calculated by appropriately interpolating the corresponding properties of the relevant interpolation points, i.e. the points that have the required fluid patch within their smoothing kernels.

1.4.2.2   Force calculation and viscosity

The principal force that requires SPH algorithms is the pressure force (gas gravity can be treated via N-body algorithms). In the typical conservative formulations of SPH, this force is calculated from a discretized form of the Lagrangian for a fluid and is given by

$$\frac{\mathrm{d}\boldsymbol{v}_i}{\mathrm{d}t} = -\sum_j m_j \left[f_i \frac{P_i}{\rho_i^2}\nabla_i W_{ij}\left(h_i\right) + f_j \frac{P_j}{\rho_j^2}\nabla_i W_{ij}\left(h_j\right) \right]; \tag{1.26}$$

the coefficient f_i is

$$f_i = \left[1 + \frac{h_i}{3\rho_i}\frac{\partial\rho_i}{\partial h_i}\right]^{-1} \tag{1.27}$$

with a corresponding expression for f_j. P_i and P_j are the pressures of the two particles, given by $P_i = K_i\rho_i^\gamma$, where K_i is an entropic function and γ is the standard isobaric-to-isochoric specific heat ratio ($\gamma = 5/3$ in adiabatic flows and $\gamma = 1$ in isothermal gas).

The entropic function is constant in both space and time and depends only on the adopted equation of state for the simulation, provided that the flow is smooth. However, in practice gas flows often develop strong gradients and even discontinuities (e.g. shocks). In these cases, the entropy of each particle is no longer conserved and this has to be accounted for. In addition, from a numerical point of view, improper treatment of shocks may lead to gas properties becoming multivalued close to the shock fronts; this is both unphysical and breaks the assumption of a smooth distribution. To alleviate this problem, artificial viscosity is implemented in SPH. The precise implementation varies from code to code, but in the case of GADGET, viscosity acts as an additional force on the particles

$$\left.\frac{\mathrm{d}\boldsymbol{v}_i}{\mathrm{d}t}\right|_{\mathrm{visc}} = -\sum_j m_j \Pi_{ij}\nabla_i\overline{W}_{ij}. \tag{1.28}$$

Here, $\overline{W}_{ij} = \overline{W}_{ji} = 0.5\left[W_{ij}\left(h_i\right) + W_{ij}\left(h_j\right)\right]$ and Π_{ij} is some function that is nonzero only if the two particles are approaching each other. The form of that function and the precise

condition for turning on the artificial viscosity (the "switch") have been the subject of a number of investigations and improvements (Monaghan and Gingold, 1983; Balsara, 1995; Morris and Monaghan, 1997; Cullen and Dehnen, 2010). GADGET uses a variant of the Morris and Monaghan (1997) implementation, which is given by

$$\Pi_{ij} = -\frac{\alpha}{2} w_{ij} v_{ij}^{\text{sig}} / \rho_{ij}, \tag{1.29}$$

where

$$v_{ij}^{\text{sig}} = c_i + c_j - 3w_{ij} \tag{1.30}$$

is called the signal velocity between the two particles, c_i (c_j) is the sound speed evaluated at particle i (j) and $w_{ij} = \boldsymbol{v}_{ij} \cdot \boldsymbol{r}_{ij} / |\boldsymbol{r}_{ij}|$ is the projection of the particle velocities on the radial vector between the two, but it is set to zero if the particles are receding from each other. This implementation allows artificial viscosity to increase in stronger shocks. The parameter α is usually set to between 0.5 and 1.

Physically, artificial viscosity behaves as an extra pressure term and allows entropy to grow as

$$\frac{\mathrm{d}A_i}{\mathrm{d}t} = \frac{1}{2} \frac{\gamma - 1}{\rho_i^{\gamma-1}} \sum_j m_j \Pi_{ij} \boldsymbol{v}_{ij} \cdot \nabla_i \overline{W}_{ij}. \tag{1.31}$$

This artificial entropy growth induces dissipation of some quantities, such as velocity and pressure, into the simulation; this may cause problems in some cases, for example, when trying to capture the effect of instabilities along sharp boundaries. However, it is a simple and rather robust way of preventing unphysical behaviour of gas at discontinuities. In the simulations presented in this Thesis, the presence of artificial viscosity does not cause any significant problems.

1.4.3   Particle motion

1.4.3.1   Time integration

There are various methods used for advancing the positions of the particles ("drifting") and updating their velocities ("kicking"). The earliest methods, such as the Euler method (Euler, 1768; Butcher, 2003), simply update both the velocities and positions at discrete points in time, letting the particles advance linearly between any such points. Such methods, however, are extremely inaccurate, unless miniscule timesteps are employed. Much more powerful are higher-order methods, where the new position of a particle is determined from a number of its previous quantities - either higher order time derivatives of its motion (velocity, acceleration, jerk, etc.) or several previous points on a trajectory.

Another advance in accuracy is achieved when a leapfrog algorithm is employed. In this method, each timestep is split into two sections. Then, the particle can be kicked for

half the timestep, drifted for the full timestep, and kicked again for half a timestep, to produce what is known as the KDK leapfrog. Alternatively, the order of the actions can be reversed, giving the DKD leapfrog. Either of the two approaches allows an even better and memory-efficient approximation to be made to the actual particle path. GADGET uses the KDK leapfrog algorithm, which requires knowledge of the particle acceleration, but does not necessitate preservation of past positions.

1.4.3.2   Timesteps

Finally, the correct duration of the particle timestep has to be determined. Qualitatively, the timestep should be as long as possible (to conserve computational resources), but not so long that accuracy of integration becomes compromised. For N-body systems, the earliest, and still rather common, constraint on timestep durations is the CFL condition (Courant et al., 1928), which states that the timestep cannot exceed a fraction $C < 1$ of the typical particle scale length divided by the typical signal velocity. The precise definitions of "particle scale length" and "signal velocity" vary between implementations, and so any given CFL condition does not by itself have a strictly defined numerical meaning. However, more precise definitions exist, most commonly based on particle accelerations, which are easier to know in absolute terms than scale lengths. GADGET employs a timestep condition

$$\Delta t_i = \min\left[\Delta t_{\max}, \left(\frac{2\eta\varepsilon}{|\mathbf{a}_i|}\right)^{1/2}, \frac{Ch_i}{\max_j\left(v_{ij}^{\mathrm{sig}}\right)}\right],\tag{1.32}$$

where $\Delta t_{\max}$ is a timestep "ceiling" set by the user, η is the desired integration accuracy, also set by the user, ε is the gravitational softening length (Section 1.4.1), $\mathbf{a}_i$ is the acceleration of particle i, C is a CFL-like factor set by the user and v_{ij}^{sig} is the signal velocity between particles i and j (eq. 1.30).

In general, the timestep calculated from eq. (1.32) is different for each particle. This may lead to problems, as particles would not be advanced coherently in time and so the forces calculated from instantaneous particle positions would represent a time-delayed (or even time-advanced) state of parts of the system. There are two ways of resolving this issue. The simplest approach is to set the actual timestep of all particles to be the shortest of the timesteps calculated for each particle. This means that the whole simulation advances in lockstep and no integration accuracy is lost, but is generally computationally inefficient, as some particles have to be integrated much more often than their dynamics require. Therefore, GADGET (and many other codes) uses an alternative approach of individual particle timesteps. Here, each particle is assigned a timestep which is a certain fraction ξ of the longest timestep in the simulation, but not longer than the duration imposed by

the condition (1.32). The fraction is constrained to be a power of two in order to preserve the accuracy of the simulation.

1.4.4   Subgrid physics

Computing power is a rather strong limitation to the temporal and spatial range that can be probed with numerical simulations. Most of the computing time is spent following particles on shortest orbits and moving with the greatest velocities; if the dynamic range in the simulation is large (typically more than an order of magnitude in linear scale), this may mean that slow-moving particles are barely advanced at all. Of course, to some extent this represents the behaviour of real physical systems: parts of the system that move, on average, with greater velocities, evolve faster than their slow-moving counterparts. Nevertheless, this numerical obstacle limits the variety of astrophysical problems that can be directly addressed by any particular simulation. If one is interested in a problem that involves processes on many different spatial and temporal scales, alternative methods are required in order to understand them. One such method is utilisation of so-called "subgrid" numerical prescriptions. These are modules in the simulation that approximate the effects of processes happening on smaller spatial scales than the resolution of the simulation (hence the name "subgrid", originally referring to being smaller than the size of a grid cell in a grid-based simulation). There is a large variety of typical subgrid modules implemented in numerical simulations. The two most important ones for the simulations presented in this Thesis are black hole accretion and gas cooling.

1.4.4.1   Sink particle accretion prescription

Supermassive black holes typically accrete from accretion discs with radii $r_{\rm d} \lesssim 0.03$ pc, because at larger radii these become unstable to self-gravity and fragment to form stars (Toomre, 1964; Goodman, 2003; King and Pringle, 2007). Any simulation that cannot resolve such small spatial scales, as is the case for the simulations presented in this Thesis, has to resort to numerical schemes to approximate the whole black hole feeding process. This is typically done by treating the SMBH as a "sink particle".

The sink particle is an N-body particle (cf. Section 1.4.1) with a mass equal to the SMBH mass, which should ideally be much greater than the mass of a single SPH particle. The particle has an accretion radius $r_{\rm accr}$ associated with it. Whenever an SPH particle approaches the sink particle closer than $r_{\rm accr}$, it is "swallowed", i.e. the SPH particle is removed from the simulation and its mass (and, if need be, momentum, angular momentum and/or other properties) is added to that of the sink particle. That way the simulation does not have to treat particles very close to the sinks, which would otherwise be typically moving very rapidly and slow down the simulation progress considerably.

Using this prescription for black hole accretion in principle allows one to connect the rate of accretion of SPH particles to the luminosity generated by the black hole particle. However, if $r_{\mathrm{accr}} \gg r_{\mathrm{d}}$, this prescription may not be realistic, as there is a significant delay between gas falling through the accretion radius and actually accreting on to the black hole, producing the luminosity. As a result, in the simulations presented in this Thesis, I have not used this connection.

There are many improvements that can be done to make subgrid accretion more realistic. For example, only particles with low enough angular momentum and energy to be captured by the black hole at r_{accr} should be captured. In addition, it is possible to have the sink particle properties track the evolution of an accretion disc as well (Power et al., 2011a). If these improvements are made, the self-consistent connection between accretion rate and black hole luminosity becomes an attractive option. Nevertheless, I have not used these adjustments since the simulations I ran do not require detailed modelling of black hole feeding and implicitly assume a sub-resolution accretion disc feeding the black hole throughout the duration of the AGN phase.

1.4.4.2   Gas cooling

Atomic and molecular processes that govern gas temperature happen on length and time scales far too small to resolve in any astrophysical simulation. While gas energy can increase due to entropy generation in shocks (see Section 1.4.2.2 above), radiative processes require subgrid prescriptions. There are many possible ways to approximate gas radiative cooling, including enforcement of an isothermal energy equation (gas temperature is kept constant all the time), a beta cooling prescription (a crude approximation of gas cooling exponentially on a timescale $t_{\mathrm{cool}} = \beta t_{\mathrm{dyn}}$, where β is a free parameter and t_{dyn} is the dynamical time of the gas particle in question) and more sophisticated ones. Among the latter, two examples of particular interest for the present Thesis both use semi-analytically calculated fits to realistic cooling functions. One is the Sutherland and Dopita (1993) cooling curve, appropriate for any low-density astrophysical plasma. Another is a heating-cooling prescription appropriate for low-density plasmas subject to quasar radiation, derived by Sazonov et al. (2005). Both take into account effects of metal line cooling, bremsstrahlung emission, photoionisation and Compton heating. Sutherland and Dopita (1993) additionally include electron collisional ionisation and more detailed atomic physics, while Sazonov et al. (2005) extend the cooling function to higher temperatures ($T \gg T_{\mathrm{c}}$, the Compton temperature; cf. Section 1.3.3) and include Compton heating/cooling and photoionisation caused by the background quasar radiation field.

1.4.5 Implementing wind feedback

Feedback from star clusters (in the form of supernova explosions and winds from massive stars) and supermassive black holes has been recognised as an important element in galactic evolution for several decades (e.g. Dopita, 1985; Merritt and Quinlan, 1998; Silk and Rees, 1998). In numerical modelling, it is usually treated with a purely subgrid prescription, adding a fraction of the SMBH or star cluster luminosity as energy into the surrounding gas (e.g. Di Matteo et al., 2005; Booth and Schaye, 2009). In this Thesis, I use a different prescription. While still involving subgrid elements, it can resolve some of the complicated dynamics of the interaction of the fast SMBH wind with the surrounding ambient gas envelope.

The core concept of this "virtual particle" method, developed by Nayakshin et al. (2009a), is the representation of the fast wind from the SMBH (see Section 1.3.2) by non-SPH particles that only exist for long enough to transfer the wind feedback momentum and/or energy to the surrounding gas (hence the name "virtual"). These particles are emitted by the SMBH isotropically and travel at a constant velocity $v_{\rm w} = 0.1c$. The particles carry momentum

$$p_{\rm virt} = \frac{L_{\rm Edd}\Delta t_{\rm BH}}{cN_{\rm virt}}, \tag{1.33}$$

where $N_{\rm virt}$ is the number of particles emitted in a black hole particle timestep $\Delta t_{\rm BH}$; the value of the latter is set to ensure that the black hole accretion timescale is adequately resolved. The number $N_{\rm virt}$ is chosen to give $p_{\rm virt} \lesssim m_{\rm SPH}\sigma$, where $m_{\rm SPH}$ is an SPH particle mass. This condition ensures that the interactions between the virtual and the SPH particles are sufficiently frequent to reduce the (random-number-generated) noise to acceptable levels. The kinetic energy of a virtual particle is $E_{\rm virt} = 0.5p_{\rm virt}v_{\rm w}$. They have negligible mass (only used as a tracer parameter) and do not participate in either N-body or SPH interactions. This allows their propagation to be followed rather quickly and prevents the simulation from grinding to a halt, as it would if any SPH particles moved with such high velocities.

Each virtual particle has a search radius, which is typically set to several times the typical SPH smoothing length in the region of interest (cf. Section 1.4.2 and eq. 1.23). Whenever an SPH particle enters the sphere defined by the search radius of the virtual particle, the propagation of the latter is integrated more carefully, potentially dropping to shorter timesteps (although in the simulations performed in this Thesis, the longest timestep was generally short enough to obtain the required accuracy). The purpose of this is to make sure that the virtual particle does not jump past an SPH particle.

The next step in the calculation happens when an SPH particle contains a virtual particle within its smoothing kernel. In this case the virtual particle starts transferring its momentum and/or energy to the SPH particle in question. This is done in steps, usually

about 10 steps are required to reduce the virtual particle's momentum to $< 1\%$ of its original value, at which point the virtual particle is removed from the simulation.

The momentum and energy given up by the virtual particle are shared by all the SPH particles that contain the virtual particle in their smoothing kernels. The fraction of momentum and energy gained by each SPH particle is proportional to the value of the smoothing function of that particle at the position of the virtual particle. This way, the effect of the virtual particle is communicated smoothly and allows resolving the coherent push by the wind, as well as some effects of optical thickness.

Energy transfer from the virtual particles to the SPH particles can be further modulated by a function dependent on SPH particle position. If the particle is within the cooling radius (Section 1.3.3), most of the kinetic energy in the pre-shock wind should have been lost to cooling before getting transferred to the gas. Therefore, I have implemented a step-function transition, using an analytically calculated expression for R_C (equation 1.20) for the problem at hand. An SPH particle with $r < R_C$ would immediately lose all energy it gained from the virtual particle, retaining only momentum; while an SPH particle with $r > R_C$ would retain both the energy and momentum input. Such a simple prescription was more than adequate for the purpose of the simulations run for this Thesis, and I even turned the transition off completely (effectively reducing the cooling radius to zero), finding no noticeable change in the results (see Chapter 2 for more details). However, a more complicated initial setup would warrant an improvement to the transition function. This function would require calculating the efficiency of cooling of the wind shock at the location of a given SPH particle from its properties in the simulation as well as implementing a smooth transition between momentum-driven and energy-driven outflows.

This method has been tested and found to work sufficiently well, at least in the case of momentum-driven flow, by Nayakshin et al. (2009a) and Nayakshin and Power (2010). The work presented in this Thesis comprises the first time this method has been applied to model energy-driven flows. Tests of energy balance and comparison with analytical predictions show that the method is adequate and precise enough for the purposes of the current investigations.

1.5   The Galactic black hole and its environment

Today, astronomers generally agree that most galaxies harbour supermassive black holes at their centres (see Section 1.1.4 for an overview of how this agreement was reached). Our own Galaxy is no exception. The dynamical centre of the Milky Way was identified with a peculiar radio source Sgr A* almost four decades ago (Balick and Brown, 1974). Later observations of stellar motions in the region revealed the presence of a rather dim ($L \simeq 300 L_\odot$) object with a mass $M_{\mathrm{SgrA}^*} \simeq 4 \times 10^6$ M$_\odot$ and radius smaller than 17

light-hours (6×10^{-4} pc; Ghez et al., 2008). Further observations of emission variability constrained the size further, to less than 1 AU (Shen et al., 2005). This evidence eliminates all reasonable doubt that the central object is a supermassive black hole.

The relative dimness of Sgr A* poses a challenge to theoretical models. According to the Soltan (1982) argument, Sgr A* gained most of its mass during phases of luminous accretion. However, its current luminosity suggests an accretion rate of $\dot{M} \sim 10^{-9} - 10^{-8}$ M$_\odot$ yr^{-1} (Yuan et al., 2003) and hence a growth timescale $t_{\mathrm{grow}} = 4 \times 10^{14} - 4 \times 10^{15}$ yr $\gg t_{\mathrm{Hubble}}$. This means that Sgr A* must have been growing much more rapidly (and so presumably was much brighter) in the past. The activity history of our Galaxy's SMBH is still an open question (Narayan, 2002; Ponti et al., 2010).

The morphology of gas in the vicinity of Sgr A* is also not typical for systems with higher Eddington ratio. There is no evidence of an accretion disc (Cuadra et al., 2003; Paumard et al., 2006), but only of a quasi-spherical accretion flow (Yuan et al., 2003). This feature has motivated development of radiatively inefficient accretion models (Narayan and Yi, 1994; Narayan et al., 1998; Blandford and Begelman, 1999). Such one-phase models seem to be the preferred solution of black hole accretion at low values of the Eddington ratio ($l \lesssim 10^{-2}$), transitioning to the standard (Shakura and Sunyaev, 1973) thin disc mode after a threshold accretion rate (and a corresponding Eddington ratio) is reached (Liu et al., 1999; Różańska and Czerny, 2000; Meyer et al., 2000).

1.5.1 The flares from Sgr A*

The dim quiescent emission from Sgr A* is punctuated by daily flares, visible in X-rays (Baganoff et al., 2001) and infrared (Genzel et al., 2003a). The flares typically last for several hours and the peak emission in both bands may rise by up to 2 orders of magnitude above quiescence (e.g. Porquet et al., 2003). All X-ray flares are accompanied by infrared ones, but not vice versa. There is tentative evidence of flaring in the sub-mm and radio wavelengths, but this is not thoroughly confirmed, and a causal connection with the X-ray/infrared flares is not established (Herrnstein et al., 2004; Mauerhan et al., 2005).

These flares suggest that the immediate environment of Sgr A* is not completely quiescent. Some stochastic process must be repeating every few hours, drastically changing the properties of (a part of) the accretion flow for a short period of time. A number of models have been proposed to explain the spectral features of the flaring state (e.g. Markoff et al., 2001; Markoff, 2005; Dodds-Eden et al., 2009), but so far no consensus has been reached. Furthermore, there is no accepted model of a physical mechanism that would trigger the flaring state, although once again, there have been several models proposed (e.g. Falcke and Markoff, 2000; Tagger and Melia, 2006; Yusef-Zadeh et al., 2006b).

In Chapter 3 of this Thesis, I investigate a model for the flares based on tidal disruption of asteroids in the vicinity of Sgr A*. The asteroids are assumed to be stripped away from

their parent stars in the central parsec of the Galaxy by the gravitational perturbations of Sgr A* and the other stars. They then form a quasi-spherical distribution, and subsequent gravitational perturbations cause relaxation of the asteroid orbital angular momentum distribution, leading to quasi-steady injection of asteroids into orbits with extremely low angular momentum. These asteroids approach the SMBH close enough to break up and evaporate, affecting the properties of the accretion flow for a short duration. I find that this is a rather promising physically-motivated model for explaining the flare frequency and size distribution. More details about the observed flares and the constraints they impose on the models are also provided in that Chapter.

1.5.2   Hints of higher past activity

Several pieces of evidence suggest that Sgr A* went through relatively recent phases of very high luminosity. Revnivtsev et al. (2004) discovered a light-echo passing through the giant molecular cloud Sgr B2, hinting at a much brighter ($L_\mathrm{X} \gtrsim 10^{39}$ erg s^{-1}) phase of Sgr A* activity that occurred ~ 100 yr ago (Ponti et al., 2010). Other similar events may have occurred earlier in the past, but we cannot detect them due to lack of such "Compton mirrors" as Sgr B2. It has been suggested that variability on century or millennium timescales may reflect feeding events from a compact ring of molecular gas circling Sgr A* (Morris et al., 1999).

Finally, recent analysis of the data collected by the *Fermi* gamma-ray telescope done by Su et al. (2010) revealed two giant (~ 10 kpc high) gamma-ray emitting teardrop-shaped cavities disposed symmetrically around the Galactic plane. These cavities, called "*Fermi* bubbles", have a narrow waist (< 1 kpc wide) at the Galactic plane and are pointing toward the Galactic centre. The bubbles have a different spectrum than the background sky and a gamma-ray luminosity of $\sim 10^{37}$ erg s^{-1}. A number of models have been proposed to explain the bubbles, including long duration Galactic wind (Crocker and Aharonian, 2011), recent jets (Guo and Mathews, 2011) and periodic stellar tidal disruption (Cheng et al., 2011).

In Chapter 2 of this Thesis, I consider a past outburst of AGN activity in Sgr A* as the cause of the *Fermi* bubbles. There is good reason to believe that a burst of star formation occurred in the central parsec ~ 6 Myr ago (Paumard et al., 2006), creating $\sim 10^4$ M$_\odot$ of stars, with an unknown amount of gas falling into the SMBH. I find that if the burst was caused by a $\sim 10^5$ M$_\odot$ molecular cloud, then most of the cloud may have accreted on to Sgr A* and triggered an Eddington-limited quasar outburst which lasted ~ 1 Myr. This outburst created an outflow, which was then collimated by the Central Molecular Zone – a reservoir of dense gas in the Galactic plane with radius ~ 200 pc – to produce the observed *Fermi* bubbles that are seen today. I refer the reader to that chapter for further details on the *Fermi* bubbles and how my model explains their properties.

1.6   Structure of the Thesis

This Thesis is composed of this introduction, three science chapters, and a conclusion chapter.

In Chapter 2, I present a model for the *Fermi* bubbles of the Milky way. Using the wind feedback model (see Section 1.3), I find that the spherically symmetric outflow from Sgr A* only has to be collimated by the Central Molecular Zone of the Milky Way - a large reservoir of predominantly molecular gas in the central ~ 200 pc of the Galaxy, positioned in a disc-like configuration along the Galactic plane - in order to reproduce the morphology and size of the observed *Fermi* bubbles (see Section 1.5.2). The two free parameters of the model – the gas fraction f_g and the duration of the quasar phase t_q – have plausible values. Furthermore, the energy content of the bubbles is reproduced as well, and I comment on how the observed emission features may be explained by this model. The results have implications for feeding of supermassive black holes in general, as well as for several other interesting features of the central parts of the Galaxy, such as the recently discovered "*Herschel* ring" (Molinari et al., 2011), the Arches and Quintuplet star clusters and the Sgr B2 giant molecular cloud.

In Chapter 3, I investigate a hypothesis regarding the origin of the flares from Sgr A* (see Section 1.5.1). The hypothesis centres on the notion that small rocky bodies - asteroids and similar sized objects - are abundant around stars in the central parsec of the Galaxy, as they are around other stars where we can observe debris discs (Wyatt, 2008). These asteroids are stripped from parent stars by tidal interactions with other stars and with Sgr A* and form a quasi-spherical distribution - a "Super-Oort cloud" (Nayakshin et al., 2012b). Dynamical relaxation processes cause asteroids from the cloud to be deflected on very low angular momentum orbits toward Sgr A* from time to time. As an asteroid comes within ~ 1 AU of Sgr A*, it is tidally disrupted and its remnants evaporate in the accretion flow around the SMBH. The new material has a very different energy distribution from the accretion flow and may serve as a physical origin for the "hot blob" spectral model of Sgr A* flares. I find, for reasonable assumptions about debris disc masses and radiative efficiency of asteroid destruction, that the numbers and luminosity distribution of the flares can be explained by this model.

Finally, in Chapter 4, I consider a more general case of an SMBH driving a large-scale outflow throughout a galaxy. I derive and solve the equation of motion for the outflow in an isothermal potential, then use it to constrain the duration of quasar activity required to clear a galaxy of gas. I find that a quasar outflow can persist for an order of magnitude longer than the quasar phase driving it. A large-scale outflow should also show observable signatures. I derive their properties and find the expected parameters that would be derived from observations of such outflows. Comparing them with several recent observations (Feruglio et al., 2010; Rupke and Veilleux, 2011; Sturm et al., 2011),

I find that the analytical predictions agree with them rather well.

Finally, I provide a brief summary of the main results in Chapter 5. I describe how the three investigations relate to the recent past, present and possible future of Sgr A*. I also discuss the implications of my work on the field of galaxy evolution as a whole and suggest several opportunities for further research along these paths.

2

Fermi Bubbles in the Milky Way: the closest AGN feedback laboratory courtesy of Sgr A*?[1]

"...and a sound arose of endless interchanging melodies, woven in harmony, that passed beyond hearing into the depths and into the heights, and the places of the dwelling of Ilúvatar were filled to overflowing, and the music and the echo of the music went out into the Void, and it was not void."

J. R. R. Tolkien, "Ainulindalë"

---

[1]The contents of this Chapter have been published as Zubovas, Nayakshin & King, 2011, MNRAS, 415L, 21 and Zubovas & Nayakshin, 2012, MNRAS, 424, 666

2.1 Introduction

2.1.1 Sgr A* – the SMBH of the Milky Way

Sgr A* is the supermassive black hole (SMBH) in the nucleus of our Galaxy. Its mass $M_{bh} \simeq 4 \times 10^6$ $M_\odot$ (Schödel et al., 2002; Ghez et al., 2005, 2008) makes it directly comparable with SMBH in other galaxies. The Soltan relation (Soltan, 1982) implies that most of the mass of these black holes was gained through luminous accretion. Yet by comparison with active galactic nuclei (AGN) Sgr A* is famously dim. It is spectacularly faint both in X-rays (less than $\sim 10^{-11} L_{Edd}$, where $L_{Edd} \sim$ a few $\times 10^{44}$ erg s^{-1} is its Eddington luminosity; Baganoff et al. 2003) and in the near infrared (Genzel et al., 2003b), prompting suggestions of a radiatively inefficient accretion flow (Narayan, 2002, and references therein). Currently, Sgr A* appears to be fed by accretion of gas captured (Cuadra et al., 2006) from the winds of the young massive stars populating the inner ~ 0.5 pc of the Galaxy (Paumard et al., 2006). However, X–ray reflection nebulae suggest that Sgr A* might have been much brighter a few hundred years ago, with luminosity of a few $\times 10^{39}$ erg s^{-1} (e.g. Revnivtsev et al., 2004; Ponti et al., 2010). This may reflect variations in the wind feeding rate of Sgr A* caused by changes in the stellar orbits of the most important wind-producing massive stars (Cuadra et al., 2008), or longer time scale feeding events from a few pc-scale molecular gas reservoirs (Morris et al., 1999).

Sgr A* is also famous as the site of a recent ($\sim 6 \times 10^6$ yr ago) star formation event in one and perhaps two stellar discs (Levin and Beloborodov, 2003; Genzel et al., 2003b; Lu et al., 2009) on scales of $\sim 0.03 - 0.5$ pc from the SMBH. The observed (e.g., Paumard et al., 2006) and theoretically constrained (Nayakshin et al., 2006) mass of the young stars is around a few times 10^3 $M_\odot$, perhaps even 10^4 $M_\odot$. Significantly, there is currently no trace of even a remnant gaseous disc near Sgr A* (Cuadra et al., 2003; Paumard et al., 2004). This led Nayakshin and Cuadra (2005) to question whether Sgr A* failed to become a quasar because this recent star formation event consumed nearly all the available gas in the central parsec of the Milky Way. They noted that this could be constrained with future observations: "a past bright AGN phase should also leave a hot buoyant radio bubble in the Milky Way halo".

2.1.2 The Galactic Centre environment

The central regions of the Galaxy are host to a number of interesting structures. For the purposes of this Chapter, the relevant ones are the Central Molecular Zone (CMZ), the stellar and dark matter background and the diffuse gas.

The CMZ is a disc of molecular gas extending out to ~ 200 pc (Morris and Serabyn, 1996). Its shape is poorly constrained (although see Molinari et al., 2011, for recent observational results identifying a ring of molecular clouds), but it appears to have a

vertical extent of ~ 50 pc above and below the Galactic plane, with which it is aligned. The mass in molecular gas contained in the CMZ is $M_{\mathrm{CMZ}} \sim 10^7 - 10^8$ M$_\odot$ (Morris and Serabyn, 1996), most of it in compact molecular clouds.

The gravitational potential of the Galaxy is dominated by stars inside the bulge and by the dark matter halo outside it. There is currently no consensus as to the shape of the potential (see, e.g., Belokurov et al., 2006; Ascasibar et al., 2006; Law and Majewski, 2010, for various arguments), so as a rough approximation, it is considered spherically symmetric in this Chapter. There is also a diffuse gaseous component, the interstellar medium (ISM), with temperature $T \sim T_{\mathrm{vir}} \sim 2.6 \times 10^5$ K and mean density $n \sim 1$ cm^{-3}. This density is much lower than that of the background inside $R \sim 1$ kpc. This suggests that gas distribution might follow the density profile of the background, i.e. there is a constant gas fraction $f_{\mathrm{g}} \equiv \rho_{\mathrm{g}}/\rho_{\mathrm{pot}}$, where "g" stands for "gas" and "pot" for "background potential".

2.1.3   The Fermi-LAT gamma-ray lobes

A recent observation may shed a rather unexpected light on a period of activity in Sgr A* that is well beyond reach of direct observations, having occured several Myr ago. *Fermi*-LAT data have recently been analysed to reveal two giant γ-ray emitting bubbles, disposed symmetrically on either side of the Galactic plane (Su et al. 2010; although see Dobler et al. 2010 and Dobler et al. 2011 for a different interpretation). They are roughly teardrop-shaped and extend $\sim 8 - 10$ kpc above and below the plane, but are centred on Sgr A* with a narrow ($d \sim 100$ pc) waist along the plane. The limbs of the lobes coincide with the extended structure seen in medium-energy X-rays by ROSAT (Snowden et al., 1997). The lobes have γ-ray luminosity $L_\gamma \simeq 4 \times 10^{37}$ erg s^{-1}, thought to be produced by some form of inverse Compton emission from cosmic rays. Observational constraints (Su et al., 2010) and emission modelling (Crocker and Aharonian, 2011) allows one to estimate the total kinetic and thermal energy content of the *Fermi* bubbles as $E_{\mathrm{bub}} \sim 10^{54-55}$ erg.

There have been several suggestions made regarding the possible origin of the *Fermi* bubbles. Su et al. (2010) discuss a number of physical processes and provide a constraint that if the bubbles are older than a few $\times 10^6$ yr, the γ-ray emission must be powered by ions rather than electrons due to a short cooling time of the latter (see their section 7.1 and Figure 28), unless electrons are continuously accelerated within the bubbles (which may not be unreasonable; see Section 2.6.4 below). Crocker et al. (2011) and Crocker and Aharonian (2011) detailed these arguments further and suggested that the emission is powered by cosmic ray (CR) protons rather than electrons. They further consider a quasi-steady state model in which the CR protons are continuously injected by supernova explosions. CR protons and heavier ions are then trapped inside the bubbles for the bubble lifetime, which the authors require to be about 10 Gyrs. Note that a long duration

quasi-static equilibrium is the only channel through which stellar processes could inflate the bubbles, as SN explosions and stellar winds cannot accelerate gas to more than a few hundred km/s (Martin, 2005; Thacker et al., 2006; Everett et al., 2008). On the other hand, Mertsch and Sarkar (2011) argued that the emission spectrum of the bubbles is inconsistent with CR protons and therefore the bubbles must be a recent feature powered by, cosmic ray electrons.

The scenario of a more recent origin of the bubbles has also been investigated by several authors. Guo and Mathews (2011) suggest that a jet launched by Sgr A* $1-2$ Myr ago could create the morphology and emission structure observed. Cheng et al. (2011) argue that the bubbles are inflated by episodic Sgr A* activity caused by tidal disruptions of stars passing too close to Sgr A*. Here I present and investigate another model of recent Sgr A* activity as the cause of the *Fermi* bubbles.

2.1.4   Sgr A* feedback: when and how?

In this Chapter I argue that Sgr A* is a very natural candidate for the source of the energy that inflated the gamma-ray lobes. As noted above, the Galactic Centre underwent a peculiar star formation event localised to the inner 0.03 - 0.5 pc about 6 Myr ago (Paumard et al., 2006). Thus, a plausible scenario is that not all of the gas deposited into the central pc of the Milky Way went into making the young stars, and a fraction of it was accreted by Sgr A*, as found in realistic simulations of the process (e.g., Bonnell and Rice, 2008; Hobbs and Nayakshin, 2009). Thus Sgr A* is likely to have had a short but very bright quasar phase concurrent with the star formation event ~ 6 million years ago.

I further argue that the observed highly symmetrical lobes are unlikely to have originated from a jet outflow. To obtain the qualitative agreement with the observed shape of the lobes, Guo and Mathews (2011) directed their jets perpendicular to the plane of the Galaxy. I claim that this would be unlikely. Radio surveys show that jet directions are completely uncorrelated with the large-scale structure of the host galaxies (Kinney et al., 2000; Nagar and Wilson, 1999). Furthermore, the observed orientations of the stellar discs in the central pc of the Galaxy (see Paumard et al., 2006) are inclined at very large angles to the Galactic plane. The jets are likely to have been fed by gas discs oriented similarly to the stellar discs. One would therefore expect that accretion of gas onto Sgr A* ~ 6 million years ago would result in jets directed at very large angles to the symmetry axis of the lobes, contradicting observations.

In contrast, a symmetrical pair of lobes with a narrow waist along the galaxy plane is natural if an isotropic outflow from near the black hole encounters higher gas densities along this plane than perpendicular to it. Near-spherical outflows like this are a direct consequence of super-Eddington disc accretion (Shakura and Sunyaev, 1973; King and Pounds, 2003) and offer a plausible explanation for the $M - \sigma$ relation (Silk and Rees,

1998; King, 2003, 2005).

2.1.5   Simulations of the Fermi bubbles

Numerical simulations of spherical outflows from accreting black holes have been carried out by, e.g., Nayakshin and Power (2010). Using a method of passing momentum of the wind to the ambient gas via "virtual" particles (Nayakshin et al., 2009a, also Section 1.4.5), they reproduce most of the analytical results of King (2003, 2005, 2010b). However, there are some important differences between the analytical and numerical results, the most important one being that on average, numerical simulations predict higher SMBH masses and/or longer activity periods in order to produce the same feedback effect as analytical calculations. This is because the analytical treatment considers bubble expansion into a stationary ISM, whereas numerical simulations treat the evolving gas density profile self-consistently.

This difference warrants a test of the analytical framework using numerical simulations. With an initial setup that mimics some important aspects of the GC environment (see Section 2.1.2), the simulations show that an initially spherical outflow can be collimated strongly enough to produce the observed shape and size of the *Fermi* bubbles. In addition, this enables me to put better constraints on the duration of the quasar phase, the mean gas density in the bulge, and the other effects that this activity might have had. I find that a longer quasar outburst is needed than calculated analytically, most likely because the energy produced by the Sgr A* outflow is spread more widely in the simulations and in reality, i.e., outside the bubbles themselves, than assumed analytically.

2.1.6   Chapter structure

The structure of this Chapter is as follows. At first, in Section 2.2, I review the theory behind the simpler and better understood quasi-spherical AGN outflows, and then consider the more complicated case of the present-day Milky Way nucleus in Section 2.3, deriving the relevant expressions showing that the model naturally predicts the shape and size of the Fermi bubbles, as well as providing some constraints on the quasar phase luminosity, its duration and the mass accreted by Sgr A* during the event. After the analytical discussion, I turn to numerical simulations to test the model, and present their setup in Section 2.4 with results following in Section 2.5. The implications of this model regarding the poorly understood problem of star formation versus gas accretion in the central parsecs of AGN, the energy content of the bubbles and radiative processes powering their emission, the activity history of Sgr A* and, by extension, other galactic nuclei, as well as the effects of feedback on the CMZ, are discussed in Section 2.6. I provide a brief conclusion in Section 2.7.

2.2 Spherical outflows

In regions close to the black hole, AGN winds are revealed through blueshifted absorption lines in X–ray emission (Pounds et al., 2003a,b; King, 2010b). Tombesi et al. (2010a,b) show that they are present in more than 35 percent of a sample of over 50 local AGN, and deduce that their solid angles are large (certainly $> 0.6 \times 4\pi$, and probably greater). The observed absorption columns imply that in many cases the flows are quite recent (few years old), suggesting that winds are an almost ubiquitous feature of central black hole activity (King, 2010a).

Although supermassive black holes in galaxy centres frequently accrete at the Eddington rate, accretion at significantly higher rates requires extreme conditions (cf King, 2010b). Accordingly I consider cases where the accretion rate far from the SMBH only mildly exceeds $\dot{M}_{\rm Edd}$, and both the central accretion rate and the outflow rate $\dot{M}_{\rm w}$ are $\simeq \dot{M}_{\rm Edd}$. Then the wind has scattering optical depth ~ 1, and the photons driving it typically scatter only once before escaping (see Section 1.3.4). The front-back symmetry of electron scattering means that the wind momentum must be of the same order as the original photon momentum, i.e.

$$\dot{M}_{\rm w} v_{\rm w} \simeq \frac{L_{\rm Edd}}{c} \tag{2.1}$$

so that the wind velocity $v_{\rm w} \sim \eta c$, where $\eta \sim 0.1$ is the accretion efficiency (e.g. King and Pounds, 2003; King, 2010b, as well as Section 1.3.2 of this Thesis). The wind flows with essentially constant velocity $v_{\rm w}$ until it shocks against the interstellar gas of the host galaxy, driving a second shock outwards into this ambient medium and sweeping it up into a shell. A simple representation of the interstellar density is the isothermal distribution

$$\rho_{\rm g}(R) = \frac{f_{\rm g}\sigma^2}{2\pi G R^2} = 2.5 \times 10^{-26} f_{-3} R_{\rm kpc}^{-2} \text{ g cm}^{-3} \tag{2.2}$$

where $f_{\rm g}$ is the gas fraction, and σ is the velocity dispersion. For the rest of this Chapter, I parametrise $f_{\rm g} \equiv 10^{-3} f_{-3}$ and $R = R_{\rm kpc}$ kpc. I also use $\sigma = 100$ km/s, appropriate for the Milky Way, unless otherwise noted.

Within this model, then, in galaxies with large $\sigma \gtrsim 150$ km s^{-1}, Eddington outflows tend to sweep the vicinity of the hole clear of gas of density given in eq. (2.2) and prevent further accretion and growth, establishing the $M-\sigma$ relation for the black hole mass (King, 2003, 2005). At smaller values of σ, any effect of this kind is out-done by the effects of mass loss from nuclear star clusters. These sweep out the gas (McLaughlin et al., 2006; Nayakshin et al., 2009b) and establish an offset $M - \sigma$ relation between the total cluster mass and the bulge velocity dispersion (Ferrarese et al., 2006, Fig. 2, middle panel). The Milky Way is probably a member of this star-cluster dominated class of galaxies, and indeed its SMBH mass lies significantly below the value predicted from the $M - \sigma$ relation

(see, e.g. Greene et al., 2010a, , Fig. 9).

The double shock pattern caused by the impact of an Eddington outflow on the host interstellar medium must move radially outwards from the vicinity of the black hole. The nature of this motion depends crucially on whether or not the shocked wind cools within the flow time. If cooling is effective, most of the energy injection rate

$$\dot{E} = \frac{1}{2}\dot{M}_{\text{out}}v^2 = \frac{\eta^2 c^2}{2}\dot{M}_{\text{out}} = \frac{\eta}{2}L_{\text{Edd}} \qquad (2.3)$$

is lost to radiation, and only the ram pressure of the outflow is communicated to the host ISM. This is a momentum-driven flow. If instead the flow does not cool, the shocked wind expands adiabatically, doing PdV work against the swept-up interstellar medium. This is an energy-driven flow, which expands faster through the ISM than a momentum-driven one (see Section 1.3.5 and Chapter 4 for more details).

2.3   *Fermi*–LAT lobes as quasi-spherical outflows

The γ-ray lobes observed by the *Fermi*–LAT instrument are very wide features that I first consider to be approximately quasi-spherical. I now consider whether the shocked gas cools in conditions appropriate for the outburst. The outflow speed $v \simeq 0.1c$ implies a shock temperature $T_s = (3m_{\text{p}}/16k)\eta^2 c^2 \simeq 1.6 \times 10^{10}$ K. This is much higher than the Compton temperature $\sim 10^7$ K of the SMBH accretion flow, so when the shock is sufficiently close to the hole, Compton cooling by the central radiation field is very effective and enforces momentum-driven flow. As the shock reaches a critical radius R_C (eq. 1.20) the radiation field becomes too dilute to cool it. Also, the shocked wind has far too low a density to cool effectively by atomic or free-free processes, so the flow becomes energy-driven (King, 2003; King et al., 2011). For the parameters of Sgr A* (mass $M_{\text{BH}} \simeq 4 \times 10^6$ M$_\odot$, velocity dispersion $\sigma \simeq 100$ km s^{-1}) the transition to energy-driven flow occurs at a radius

$$R_C \simeq 12 \, f_{-3}^{1/2} \text{ pc}. \qquad (2.4)$$

Even at the cosmological gas fraction ($f_{-3} = 160$) the estimate (2.4) is so small compared with the size of the γ-ray lobes that the outflow can be considered essentially always energy-driven in directions away from the Galactic plane (note that this approximation is only valid when considering such large scale structures; the gas dynamics and quenching of black hole accretion, which is expected to produce the $M - \sigma$ relation, are still governed by the momentum-driven flow equations). In an energy-driven outflow, the shocked wind density driving the expansion is always much lower than the density of the swept-up interstellar medium outside it. This makes the shock interface inherently Rayleigh-Taylor unstable (cf King, 2010a). The hot shocked gas mixes with cool dense interstellar gas

throughout the flow in directions away from the Galactic plane. This mixture is clearly a promising site for γ-ray emission (see Section 2.6.5). On the other hand, within the Galactic plane the gas density is far higher, and one would expect little expansion (see also Section 2.3.3). This kind of outflow thus naturally produces the main qualitative features of the *Fermi*-LAT gamma-ray map: extensive γ-ray emitting lobes placed symmetrically on each side of the Galactic plane, with a narrow waist in the plane.

2.3.1 Kinematics of the energy-driven flow

King (2005) derived the properties of an energy-driven flow starting with the equation of motion

$$\frac{\mathrm{d}}{\mathrm{d}t}\left[M(R)\dot{R}\right] + \frac{GM(R)M_{\mathrm{tot}}(R)}{R^2} = 4\pi R^2 P \tag{2.5}$$

and the energy equation

$$\frac{\mathrm{d}}{\mathrm{d}t}\left[\frac{4\pi R^3}{3} \times \frac{3}{2}P\right] = \frac{\eta}{2}lL_{\mathrm{Edd}} - P\frac{\mathrm{d}}{\mathrm{d}t}\left(\frac{4\pi}{3}R^3\right) - 4f_{\mathrm{g}}\frac{\sigma^4}{G}\dot{R}. \tag{2.6}$$

Eliminating the pressure P between the two equations and expressing the enclosed mass using equation 1.16 gives

$$\frac{\eta}{2}lL_{\mathrm{Edd}} = \frac{2f_{\mathrm{g}}\sigma^2}{G}\left[\frac{1}{2}R^2\dddot{R} + 3R\dot{R}\ddot{R} + \frac{3}{2}\dot{R}^3\right] + 10f_{\mathrm{g}}\frac{\sigma^4}{G}\dot{R}. \tag{2.7}$$

This equation has a solution $\dot{R} = v_{\mathrm{e}} = const.$ while the quasar is active:

$$v_{\mathrm{e}} = \left[\frac{2\eta\sigma^2 c}{3}\frac{0.16}{f_{\mathrm{g}}}\frac{M}{M_\sigma}l\right]^{1/3} \simeq 1920\ \sigma_{100}^{2/3}\ f_{-3}^{-1/3}\ l^{1/3}\ \mathrm{km\ s}^{-1}. \tag{2.8}$$

Here M_σ is the predicted value of the SMBH mass in the Milky Way from the $M - \sigma$ relation (eq. 1.18), $M \simeq 0.2M_\sigma$ is the mass of Sgr A* and $l \equiv L/L_{\mathrm{Edd}} \sim 1$ is the Eddington ratio of the SMBH luminosity.

For the rest of this section I model the outflow away from the disc plane as a sector of a spherical flow. If the Eddington accretion phase lasts for a time t_{q}, the shock reaches a radius

$$R_0 \simeq v_{\mathrm{e}}t_{\mathrm{q}} \tag{2.9}$$

by the time the quasar phase ends. However the shocked wind gas is able to drive further expansion, which finally stalls at a radius

$$R_{\mathrm{stall}} \simeq \frac{v_{\mathrm{e}}}{\sigma}R_0 \simeq \frac{v_{\mathrm{e}}^2}{\sigma}t_{\mathrm{q}} \tag{2.10}$$

after a time

$$t_{\text{stall}} \simeq 0.5 \left(\frac{v_{\text{e}}}{\sigma}\right)^2 t_{\text{q}} \tag{2.11}$$

(see King et al., 2011, and Chapter 4 for derivation), so that

$$t_{\text{stall}} = \frac{R_{\text{stall}}}{2\sigma}. \tag{2.12}$$

2.3.2   Implications for the outburst properties

I now apply these results to our Galaxy, and in particular the γ-ray lobes. If the outflow producing the observed lobes had stalled, then $R_{\text{stall}} \sim 10$ kpc, which from (2.12) requires $t_{\text{stall}} = 50$ Myr. This would mean that the outflow was produced well before the last accretion event in the Galactic Centre, which appears unlikely, as there is no evidence of Sgr A* activity at around that time.

If instead one assumes that the γ-ray lobes were produced in this event, it is obvious that the energy-driven outflow is still proceeding, with a mean velocity $\langle v \rangle \gtrsim 1600$ km s^{-1} over its lifetime. This immediately provides a constraint on the gas density in the bulge of the Milky Way:

$$f_{-3} \lesssim \left(\frac{1920}{1600}\right)^3 l \simeq 2l \ . \tag{2.13}$$

It is clear that the gas fraction in the Milky Way halo must have been similar to 10^{-3} in order for the bubbles to be inflated within the present model. Numerical simulations below confirm this.

Requiring $t_{\text{stall}} > 6$ Myr in eq. (2.11) now gives $t_{\text{q}} \gtrsim 5 \times 10^4$ yr. Additionally, requiring that the bubble stalling radius should be greater than their current radius, equations (2.10) and (2.8) give

$$t_{\text{q}} > 2.5 \times 10^5 f_{-3}^{2/3} \text{ yr}. \tag{2.14}$$

As both estimates are lower limits on the outburst duration, only the larger one of the two (i.e., eq. 2.14) is relevant.

In 0.25 Myr, Sgr A* accreting at its Eddington limit consumes $\Delta M \simeq 2 \times 10^4$ M$_\odot$ of gas. This is greater than the total expected if the hole accreted the disc mass

$$M_{\text{disc}} \sim \frac{H}{R} M_{\text{BH}} \simeq 8000 \text{ M}_\odot \tag{2.15}$$

within the self-gravity radius where the ring of young stars formed (cf equations 7, 12 of King and Pringle, 2007). This estimate also exceeds the results of Nayakshin (2005). I return to this point in section 2.6.8.

Within the wind feedback model, at least $\sim 2 \times 10^{56}$ erg is ejected as the outflow's mechanical energy. This is more than an order of magnitude larger than the energy

content of the bubbles as estimated by Su et al. (2010). However, I find that a large fraction of the outflow's energy goes into mechanical work expended to drive the ambient cooler medium away from the Galaxy's centre. Zubovas and King (2012, also Chapter 4 of this Thesis) show that even while the quasar driving is on, only 1/3 of the energy input is retained in the shocked wind while the quasar is active. When the quasar turns off, the bubble expands adiabatically, converting its thermal energy into kinetic energy of the bubble and the surrounding shell. Therefore it is likely that the actual amount of energy retained by the bubbles is much lower than the original energy input by Sgr A* into the outflow, bringing the value in line with the observations. Numerical simulations confirm this prediction; cf. Section 2.6.3.

2.3.3   The role of the Central Molecular Zone in focusing the outflow

The shell expansion velocity, v_e, depends on the gas density in the direction of expansion (eq. 2.8). Clearly, if the ambient gas distribution is not spherically symmetric then the outflow must lose its spherical symmetry too. As a minimum effect, the velocity of the contact discontinuity must be smaller in the directions of denser gas. The most salient feature in the distribution of gas in the inner Galaxy – the Central Molecular Zone (CMZ; Morris and Serabyn, 1996, ; see Section 2.1.2), a massive disc-like molecular gas feature in the inner ~ 200 pc – presents an almost impassable barrier to the Sgr A* outflow. The mass of the molecular gas in the zone is $M_{\mathrm{CMZ}} \sim 10^8\ M_8\ \mathrm{M}_\odot$ (Dahmen et al., 1998; Pierce-Price et al., 2000). Its weight is

$$W_{\mathrm{CMZ}} \sim \frac{GM_{\mathrm{enc}}(R_{\mathrm{CMZ}})M_{\mathrm{CMZ}}}{R_{\mathrm{CMZ}}^2} = \frac{2M_{\mathrm{CMZ}}\sigma^2}{R_{\mathrm{CMZ}}} \simeq 6.4 \times 10^{34} M_8\ \mathrm{dyn}, \qquad (2.16)$$

where $M_{\mathrm{enc}}(R_{\mathrm{CMZ}})$ is the mass enclosed within radius $R_{\mathrm{CMZ}} \sim 200$ pc. The outward force (momentum flux of the outflow incident on the CMZ) in the isotropic outflow model is

$$F_{\mathrm{out}} \sim \frac{H}{R}\frac{L_{\mathrm{Edd}}}{c} \simeq 4.3 \times 10^{33} \mathrm{dyn}, \qquad (2.17)$$

where $H/R \sim 0.2 - 0.3$ is the geometrical aspect ratio of the disc (see Fig. 1 in Morris and Serabyn, 1996).

Comparing the two for the fiducial parameters accepted above, one finds

$$\frac{F_{\mathrm{out}}}{W_{\mathrm{CMZ}}} \sim 0.05\ M_8^{-1}, \qquad (2.18)$$

which shows convincingly that the outflow from Sgr A*, even in its full 'quasar' mode, is not strong enough to disperse the CMZ since the latter is simply too massive. This conclusion is reinforced by the fact that there is also atomic and ionised gas in the region

of the CMZ disc that would increase W_{CMZ} further.

Another way to come to the same conclusion is by estimating the gas density in the midplane of the CMZ, for which I infer $\rho_{CMZ} \sim 5 \times 10^{-22}$ g cm^{-3} with the parameters mentioned above, whereas the density of gas which could be driven away by a SMBH outflow, for a SMBH obeying the $M - \sigma$ relation, is given by equation 2.2, and is $\sim 10^{-22}$ g cm^{-3} at $R = 200$ pc and $\sigma = 100$ km s^{-1}. As Sgr A* is undermassive compared with the prediction from $M - \sigma$, the discrepancy between the two densities is even larger.

I therefore conclude that the outflow along equatorial directions stalls, except in the rare cases where local density variations provide an avenue for escape. As the observed column density in the Galactic plane varies little with direction in the Galactic Centre region (Goto et al., 2008; Schödel et al., 2010), I believe it is reasonable to neglect the effect of this escape (see Section 2.6.7). The shocked outflow gas cannot simply pile up there, however. Indeed, if that were the case then the pressure (thermal energy density) would increase in that location without limit. The thermal pressure of the shocked gas in the directions perpendicular to the Galactic plane is much lower because the outflow proceeds in those directions easily. Thus there is a strong pressure gradient in the shocked outflow gas pointing perpendicular to the Galactic plane. This pressure gradient clearly must launch a "secondary" thermally driven outflow away from the Galactic plane, efficiently collimating Sgr A* outflow into these directions.

Kompaneets (1960) considered propagation of a blast wave in an exponential plane-parallel atmosphere. Moellenhoff (1976) used a similar approach and proposed that the double extragalactic radio sources are formed by explosions of supermassive stars in the centres of oblate galaxies. He has shown that the outflow accelerates in the direction of the axis of rotation of the galaxy, and eventually results in ejection of two clouds of gas into these directions. From the point of view of qualitative gas dynamics, the present model is a reincarnation of these earlier ideas. However, the initial conditions used here are observationally motivated and tied to the case of the Milky Way. The background density field (the rotationally supported massive CMZ and non-rotating diffuse "halo" gas; see Sections 2.1.2 above) is very different from the density fields considered by Moellenhoff (1976) and others for the double extragalactic radio sources. As a result, I do not use their results directly, but comment upon the differences in Section 2.6.1.

There are two possible complications to this simple picture. First of all, the estimate does not take into account energy deposition by the outflow into the CMZ, which makes the latter somewhat more prone to the feedback; see Section 2.6.7. The vertical thermal expansion timescale is $\sim t_{dyn} (T_{CMZ}/T_h)^{1/2}$, where T_h is the temperature of the shock-heated CMZ gas. In the simulations, I find that most of the CMZ gas remains rather cold, with maximum temperature $\lesssim 3 \times 10^5$ K. At such temperatures, cooling is very efficient (Sutherland and Dopita, 1993). As a result, the shock-heated gas cools down rapidly, and

the expansion timescale is still comparable to the duration of the quasar phase, therefore this extra heating effect is not dominant.

Another complication is the possible instability of the interaction between the SMBH wind and the dense material in the CMZ disc. I discuss this in more detail in Section 2.6.5.3. Overall, I do not expect significant growth of instabilities that would affect the general dynamics of the outflow pushing against the CMZ.

In conclusion, although outflows ultimately control black hole growth, and materially affect the Galaxy bulge, as shown by the $M - \sigma$ relation, they cannot disperse the Galaxy disc, as recently shown by Nayakshin et al. (2012a). This fits very naturally with the recent conclusion by Kormendy et al. (2011) that SMBHs do not correlate observationally with host galaxy discs.

2.4   Numerical simulation setup

2.4.1   Numerical method

The workhorse code for solving gas dynamics in the fixed potential of the bulge and the black hole is GADGET-3, an updated version of the code presented in Springel (2005).

Feedback from the SMBH is implemented with the "virtual particle" method explained in detail in Nayakshin et al. (2009a) and in Section 1.4.5 of the Introduction chapter. I track both the momentum and kinetic energy feedback from the SMBH wind, and formally adopt $R_{\rm C} = 0$, finding no difference in the results from the case when a more appropriate cooling radius is used.

While I do not model hydrodynamically the reverse wind shock, which thermalises the wind and creates a pressurised bubble that can expand adiabatically, I find that this process is somewhat mimicked in the simulations by low density gas that is present in the otherwise evacuated bubble. These particles predominantly originate on the surfaces of the Central Molecular Zone (see Sections 2.4.2 and 2.5.1.3 below), where they are heated to very high temperatures and rise to fill the voids; subsequently the quasar wind heats these particles even further. The bubbles are found to be significantly over-pressurised with respect to the surrounding gas. This allows the bubble to expand thermally as expected if the reverse shock were modelled by SPH (see Section 2.5.1 below).

In all the simulations presented below, I use an ideal equation of state for the gas. The gas pressure is given by $P = \rho kT/\mu$, where mean molecular weight, $\mu = 0.63m_{\rm p}$ (assuming ionised gas of Solar abundance), k is Boltzmann's constant, and ρ and T are the gas density and temperature, respectively. In all simulations except for one, I employ the standard GADGET optically thin cooling prescription based on the Sutherland and Dopita (1993) cooling curves, in addition to heating from the virtual particles on the contact discontinuity of the bubble. In the only exception to this, simulation 'Cool' (see

Test	f_g	$N_\mathrm{p,halo}$	t_q/Myr	$\left(\frac{H}{R}\right)_\mathrm{CMZ}$	$M_\mathrm{CMZ}/M_\odot$	$N_\mathrm{p,CMZ}$	R_b/kpc	d_b/kpc	h_b/kpc	v_v/km s^{-1}	v_h/km s^{-1}
Base	10^{-3}	7.5×10^5	1	0.25	10^8	10^6	11.5	9	~ 1	1090	670
HR-low	10^{-3}	7.5×10^5	1	0.125	10^8	10^6	11.5	9	~ 1	1110	680
Cool*	10^{-3}	7.5×10^5	1	0.25	10^8	10^6	9.5	10	~ 1	820	650
Fg-low	4×10^{-4}	3.0×10^5	1	0.25	10^8	10^6	~ 15	~ 10	2.5	2560	610
Fg-high	4×10^{-3}	3.0×10^6	1	0.25	10^8	10^6	6	6	~ 1	220	400
Tq-low	10^{-3}	7.5×10^5	0.3	0.25	10^8	10^6	7	4	2	300	360
Both-low	4×10^{-4}	3.0×10^5	0.3	0.25	10^8	10^6	~ 7	~ 4	4	960	270
Mc-low	10^{-3}	7.5×10^5	1	0.25	10^7	10^5	7	8	2	330	470

Table 2.1: *Fermi* bubble numerical simulation parameters and main results; see Sections 2.4 and 2.5 for more details. From left to right, the parameters are: Test ID, gas fraction, number of SPH particles in the halo, quasar outburst duration, CMZ mass, CMZ scale height, number of particles in the CMZ. The results are: bubble height, width and distance between its lower edge and the SMBH; velocity of the swept-up ISM in the z direction at $x = y = 0$ and velocity of the swept-up ISM in the xy plane at the mid-height of the bubble; all five at 6 Myr.

* - Simulation 'Cool' is identical to 'Base', but includes a Sazonov et al. (2005) heating-cooling prescription.

Table 2.1), I check the sensitivity of the results to the assumed cooling function by utilising the optically thin radiative cooling rates for gas ionised (and also heated) by the quasar radiation field as calculated by Sazonov et al. (2005), who also provided an analytical fit to the respective rates that I use here.

Simulation snapshots showing density and temperature are plotted using an angle slice projection method presented in Nayakshin and Power (2010). Specifically, the gas column density projected over the y coordinate is calculated by

$$\Sigma(x, z) = \int_{-y(x,z)}^{y(x,z)} \rho(x, y, z)\, dy, \qquad (2.19)$$

where the limits of the integration are given by $y(x,z) = r \tan \zeta$ and $r = \sqrt{x^2 + z^2}$. The angle ζ is chosen so that $\tan \zeta = 1/4$ throughout this paper. This projection method conveniently allows one to get an unobscured look into the inner parts of the simulation and yet have enough particles at the outer edges for a statistically meaningful figure to be derived when plotting. In addition, since most of the results presented in this paper are symmetrical around the z axis, the snapshot plots, where applicable, are divided vertically and show the surface density in blue-white on the left and temperature in red-orange on the right. On some surface density plots, I also show the gas velocity vectors projected on the plane of the figure. Their magnitudes are scaled to the maximum velocity in a given plot, so they only give qualitative information about gas dynamics.

2.4.2   Galaxy model and initial conditions

The initial setup for the Galaxy consists of three components, described below and summarised in Table 2.1. The 'Base' model is the model which best reproduces the *Fermi* bubble observations (Su et al., 2010). I analyse this simulation in detail below, and study the robustness of the results by varying some parameters of the model.

The whole computational domain is embedded in a static isothermal background potential with $\sigma = 100$ km/s. In the centre of the coordinate system, fixed in space, is the SMBH. While I do not model accretion on to Sgr A* in detail (See Section 2.6.8), occasionally SPH particles may get very close to the SMBH, especially closer to the end of the simulations when feedback from Sgr A* is turned off. To avoid very small time steps, and thus very high numerical costs, associated with these "uninteresting" particles, I remove them using the sink particle formalism if the SPH particles are closer than $r_{\mathrm{sink}} = 0.1$ pc to Sgr A*. The SMBH particle is "turned on" at the start of each simulation, radiating at its Eddington limit for a duration t_{q}, which is a free parameter of the model. Most of the models presented here use $t_q = 1$ Myr (since this was found to give the best results), although I explore shorter outbursts as well.

I position a massive disc of gas – the Central Molecular Zone (CMZ; Morris and

Serabyn, 1996) – in the plane of the Galaxy at a distance between $R_{\rm in,CMZ} = 5$ pc and $R_{\rm out,CMZ} = 200$ pc from Sgr A*. The inner radius is chosen so that the whole CMZ would be comfortably outside the sphere of influence of Sgr A* ($R_{\rm infl} \sim 2$ pc), but still account for the yet smaller circumnuclear disc of gas, which is observed to lie between ~ 2 and ~ 10 pc from the centre (Guesten et al., 1987; Morris and Serabyn, 1996). The model CMZ has uniform temperature throughout, chosen to give the appropriate constant scale height aspect ratio ($H/R = 0.25$ or 0.125), which is also the temperature floor adopted for the simulation in question. It is rotationally supported in the radial direction, with $v_{\rm rot} = \sqrt{2}\sigma$. The radial density distribution follows a $\rho \propto R^{-2}$ power law, and the mass of the disc is set to $M_{\rm CMZ} = 10^8$ M$_\odot$ (approximately the upper limit from observational constraints), although I ran one simulation with a much lower CMZ mass. Despite the high mass of the CMZ, it is marginally stable to self-gravity, since the Toomre (1964) parameter $Q \sim 3.4$ for $H/R = 0.25$, and 1.7 even for $H/R = 0.125$. Note that I do not fine-tune the CMZ to be only marginally stable in the simulations; it is a natural outcome of using the observationally constrained CMZ parameters. This result is probably not a coincidence: massive cold discs are widely believed to be self-regulating to have $Q \sim 1$ (Goodman, 2003; Thompson et al., 2005; Nayakshin et al., 2012b). In principle, such a low Q parameter might lead to fragmentation. However, since I set the temperature floor in the simulations to be equal to the initial CMZ temperature, I do not expect a significant fragmentation to occur (Gammie, 2001; Rice et al., 2005). This assumption is consistent with simulation results (see Sections 2.5.1.3 and 2.6.7 below). The SPH particle mass is $M_{\rm part} = 100$ M$_\odot$, giving a minimum mass resolution of ~ 4000 M$_\odot$.

Finally, there is a diffuse spherically symmetric gaseous "halo" extending between $r_{\rm in} = 1$ pc and $r_{\rm out} = 15$ kpc with density following the isothermal profile given by equation 2.2. The gas fraction $f_{\rm g}$ is a free parameter of the model and is varied between 4×10^{-4} and 4×10^{-3} in different tests, with the fiducial value of 10^{-3} for the 'Base' model (this corresponds to a particle density 6×10^{-4} cm^{-3} at $R = 5$ kpc; see Section 2.6.2 for the validity of this choice for gas density). The number of particles in the halo is set by their mass (I use same SPH particle masses for the CMZ disc and the halo). The gas temperature in the bulge halo is initially set to $T_{\rm halo} = T_{\rm vir} = 2.5 \times 10^5$ K, which corresponds to the virial temperature of the bulge. The initial gas velocity in the bulge is set to zero.

This halo setup I use is certainly oversimplified. For example, I do not account for the likely anisotropy of the initial gas distribution of the "halo" due to overall rotation of the Galaxy. I address this point qualitatively in the Discussion section.
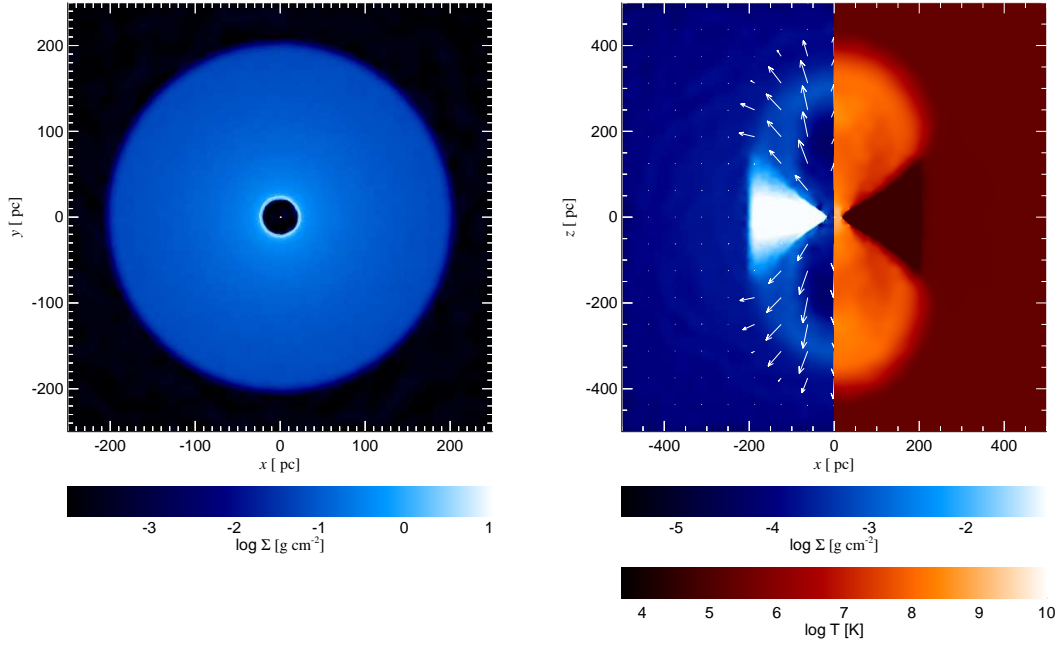
Figure 2.1: **Left:** The face-on column density of the CMZ disc at time $t = 0.1$ Myr for the 'Base' simulation. Note that the innermost region has been partially evacuated by Sgr A* feedback. **Right:** Cross-sectional plot of gas surface density (left half of the panel, blue-white) and temperature (right, red-orange) for the same snapshot. The CMZ (cold dense wedge in the Galactic plane) strongly collimates the outflow; even though its surfaces are ablated, teardrop-shaped cavities form readily.
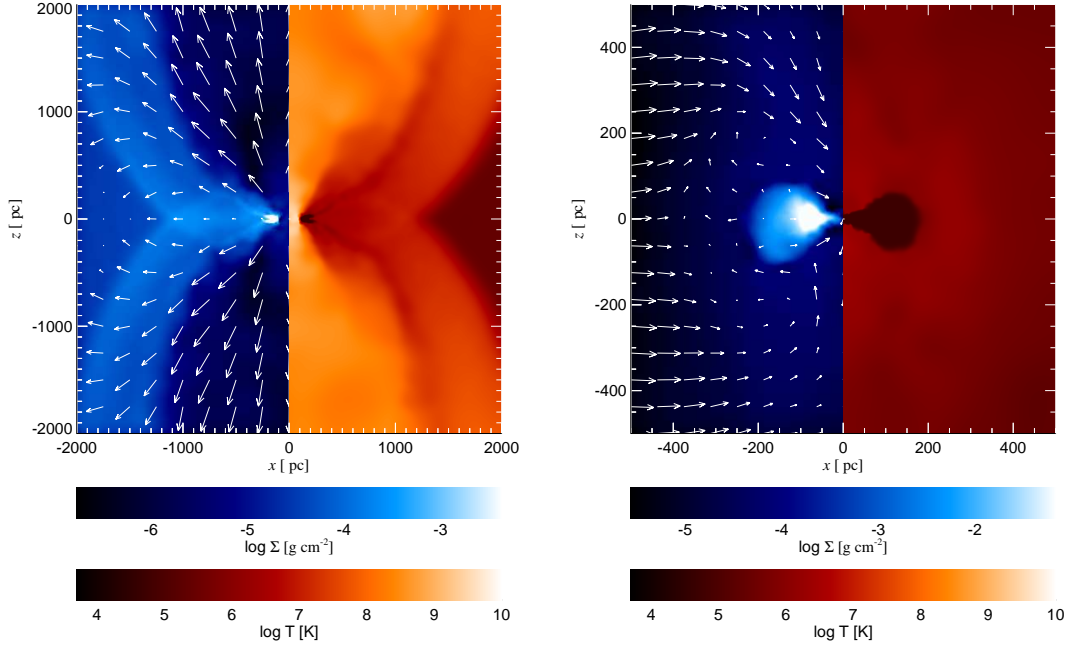
Figure 2.2: **Left:** Side view of gas surface density (left half of the panel, blue-white) and temperature (right, red-orange) in the central 2 kpc of the 'Base' simulation at $t = 1$ Myr. The CMZ has been enveloped by the external ISM shock fronts, but it still maintains the strong collimation of the diffuse cavities. The cavities are also filled with hot $10^8 - 10^9$ K gas, which allows them to expand in all directions once the feedback from Sgr A* has switched off. **Right:** Central 500 pc of the 'Base' simulation at $t = 6$ Myr. The CMZ remains, although its structure is perturbed. There is also a back-flow of warm ($T \simeq T_{\mathrm{vir}}$) gas into the central regions, evacuated by the buoyant rise of the bubbles.

2.5   Results

Table 2.1 shows the list, parameters and main results of all of the simulations that I present in this Chapter. Results of the three simulations in the top of the Table, separated from the rest by a horizontal line, appear to be a reasonable match to the *Fermi* Bubble observations by Su et al. (2010). The rest of the simulations produce bubbles that are unlike the observed ones.

I first describe the evolution and properties of the 'Base' model ($f_{\mathrm{g}} = 10^{-3}, t_{\mathrm{q}} = 1\,\mathrm{Myr}$).

2.5.1   Base simulation

2.5.1.1   Small and intermediate scales

Overall, the dynamics of gas in the simulation closely follows the analytical expectations. Almost immediately after the quasar switches on, the spherically symmetric outflow hits both the CMZ and the halo gas. The left panel of Figure 2.1 shows the face-on view of the CMZ disc at time $t = 0.1\,\mathrm{Myr}$. Note that only the central ~ 25 pc of the disc were evacuated by outflow from Sgr A*. The right panel of the same figure shows the edge-on projections of both gas column density and temperature (which I present in a single panel because of the azimuthal symmetry of the gas flow).

As expected, the spherical "halo" (the diffuse gas component) is affected by the outflow much more than the CMZ, with the contact discontinuity between the wind and the shocked ambient medium at a distance of about 300 pc. Also note that the bubbles do contain some gas mainly closer to the interface with the upper layers of the CMZ. That gas is heated to temperatures above 10^8 K. There is a transition region between the almost-spherical outflow perpendicular to the Galactic plane and the stalled outflow against the CMZ, completing the figure-8 morphology of the whole flow.

As time proceeds the inner hole in the CMZ disc grows in size, engulfing most of the disc by the end of the simulation (see Section 2.5.1.3 for a fuller discussion of this). The cavities opened by the outflow in the directions perpendicular to the Galactic plane grow even more. The left panel of Figure 2.2 shows the edge-on view of the inner 2 kpc of the Galaxy at time $t = 1\,\mathrm{Myr}$. Note the hour-glass shape of the cavities opened by the outflow, and a strong gradient in the outflow velocity with angle θ ($\tan\theta = |z/x|$) measured from the z-axis. In particular, the maximum velocity is reached at $\theta = 0$, such that velocity there is consistent with the analytical prediction of $v_{\mathrm{e}} \sim 2000$ km/s, and the minimum is at $\theta = 90°$. There is also a "failed" outflow around $\theta \approx 65°$; gas flowing along these directions eventually falls on the Galactic plane, shadowed by the CMZ from further Sgr A* feedback. Some material is ablated from the surfaces of the CMZ. It expands and contributes to the tenuous gas filling the cavities.

The right panel of Figure 2.2 presents the edge-on view of the central 500 pc at the

end of the simulation, at $t = 6$ Myr. Due to the relative buoyancy of the hot gas in the cavities with respect to the cooler ambient gas, the former leaves the region by that time, being replaced by the latter. This back flow of warm ($T \simeq T_{\rm vir}$) gas returning to the central region after Sgr A* switched off is clearly seen in the pattern of velocity vectors on the left hand side of the right panel of Figure 2.2. Note also that while the CMZ has been significantly affected by the outflow from Sgr A*, most of it remains in the region in the form of a ring discussed further in Section 2.5.1.3.

2.5.1.2   Large scales

I now discuss the larger scales of the 'Base' simulation. Figure 2.3 shows the edge-on views of the simulation domain at times $t = 1, 3$ and 6 Myr (clockwise from top left, respectively). The top left panel in particular shows that by the time Sgr A* switches off the cavities are still rather small when compared with the scale of the Galaxy: their height is $R \sim 3$ kpc and the maximum width is $d \sim 2.5$ kpc.

Further evolution of the hot bubbles is driven by the inertia of the outflow, the buoyancy of the bubbles and the fact that they are significantly over-pressurised with respect to the ambient medium (cf. the top left panel of Figure 2.4). Bubble expansion proceeds in an almost self-similar fashion, except for a ripple at roughly the middle of the bubble height (see Fig. 2.3, top right). It is most likely a Kelvin-Helmholtz unstable mode which arises due to the material inside the bubble moving parallel to the surface of the contact discontinuity. The ripple rolls over and disappears by $t = 6$ Myr (Fig. 2.3, bottom).

By the end of the simulation, the cavities have expanded to reach a height of ~ 11.5 kpc (Fig. 2.3, bottom), consistent with the observed vertical extent of the *Fermi* bubbles (Su et al., 2010). The width, at ~ 9 kpc, is slightly larger than observed ($d_{\rm obs} \sim 6$ kpc); I return to this point in Section 2.6.1. The cavities are filled with very hot ($T_{\rm bub} \sim 2 \times 10^8$ K ~ 17 keV) and diffuse ($f_{\rm g,bub} \sim 2 \times 10^{-5}$; see Fig. 2.4, bottom) gas. For completeness, Figure 2.5 shows the time evolution of the bubble's height, R, and width, d. The lateral expansion is initially somewhat slower than the vertical, but catches up in the Myr after the quasar switches off; the bubbles are as wide as they are tall at $t \sim 2$ Myr. This happens presumably because some of the material expanding outward along the disc plane was blown off the top of the CMZ disc (rotating gas is easier to blow away due to centrifugal force). Subsequently, vertical expansion once again becomes faster than lateral one. This may be driven by buoyancy: as the bubbles continue to rise up, their lower edges "lift off" from the plane, and the cooler gas can start flowing back along the plane.

The bubbles are slightly detached from the very centre of the Galaxy; the gradual increase in this detachment is visible in Figure 2.3, and also in the right panel of figure 2.2. This detachment is caused by the bubbles rising buoyantly out of the Galaxy potential. By $t = 6$ Myr, the gap between the centre and the lower edges of the bubbles is $h \sim 1$ kpc,
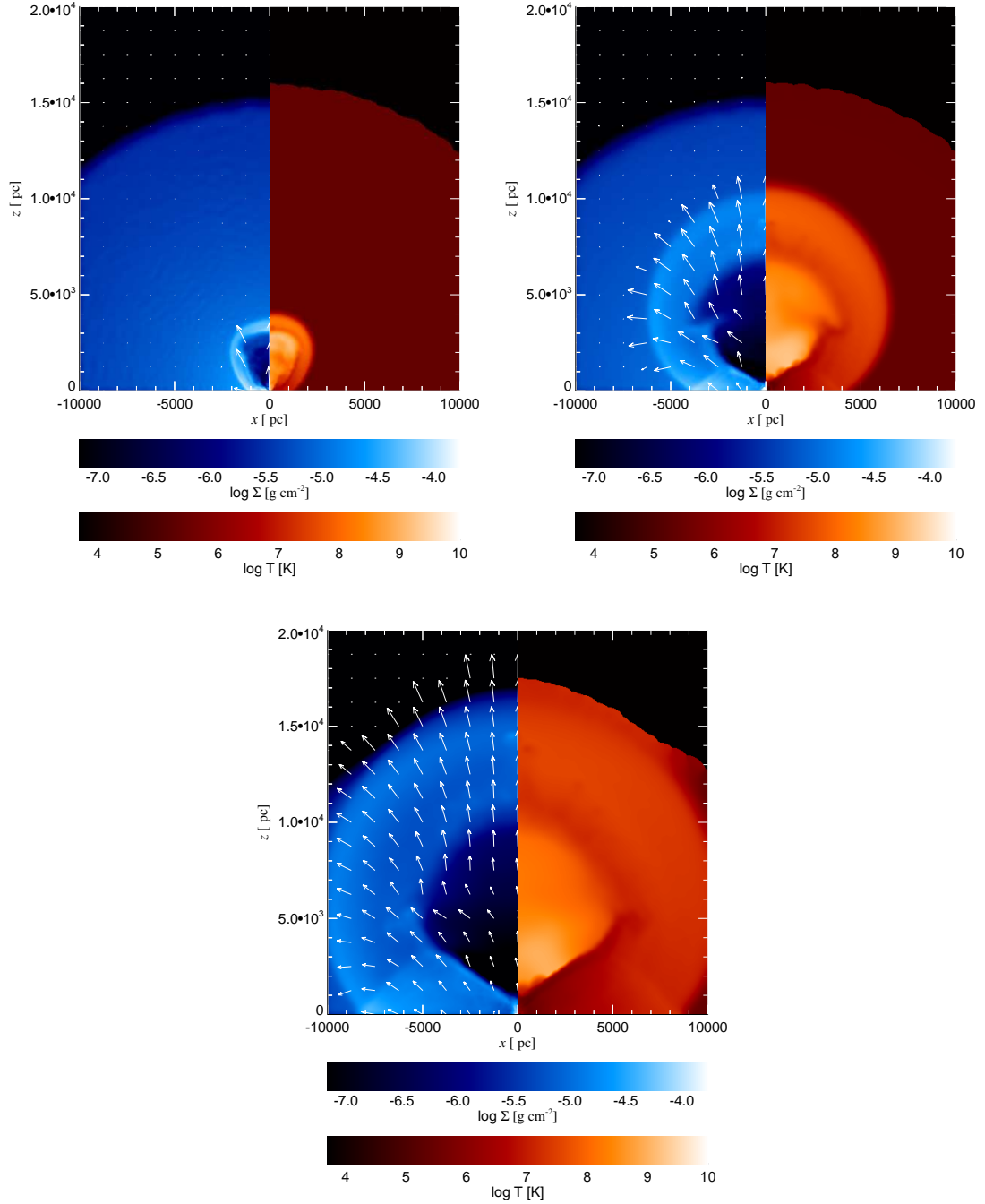
Figure 2.3: Gas evolution on large scales in the 'Base' simulation; the three panels correspond to $t = 1, 3$ and 6 Myr, clockwise from top left. Only the positive-z side of the computational domain is shown, due to symmetry around the Galactic plane. The CMZ strongly collimates the outflow and allows the formation of a teardrop-shaped cavity with a morphology very similar to that of the observed *Fermi* bubbles. The bubbles continue to expand and rise due to high pressure and low density, even once the feedback has switched off.
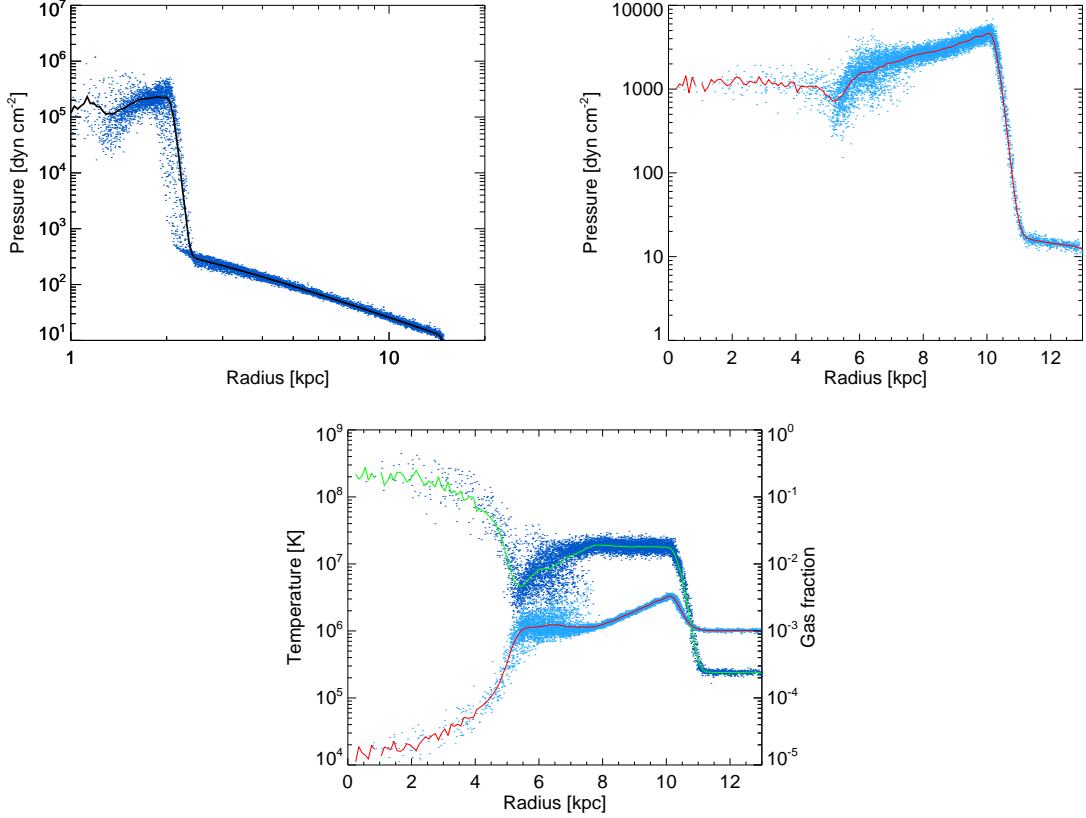
Figure 2.4: **Top left**: Gas pressure as a function of cylindrical radius ($r_{\mathrm{cyl}}^2 = x^2 + y^2$) for a selection of SPH particles at $1 < |z| < 2.5$ kpc (middle of the bubble) for the 'Base' simulation at $t = 1$ Myr; the solid line is the mean value at each radius. The central cavity is significantly over-pressurised in comparison to the ambient medium, leading to lateral expansion of the bubbles. **Top right**: Same but at time $t = 6$ Myr when the bubble is much larger. The vertical cut chosen is now $4.5 < |z| < 6$ kpc. Note that the gas pressure has dropped significantly and is slowly varying across the bubble and the shocked region. **Bottom**: Temperature (green curve and dark blue points, left scale) and gas fraction (red curve and light blue points, right scale) against cylindrical radius for the same time and particle cut as the top right panel. The hot diffuse inner cavity and dense surrounding medium are obvious and have rather sharp edges (thickness ~ 1 kpc). Solid lines show mean values of gas fraction and temperature at each radius.
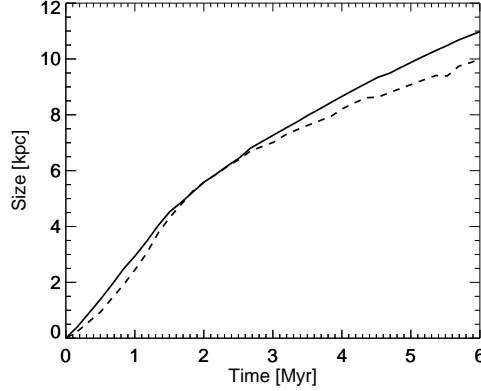
Figure 2.5: Height (solid line) and width (dashed line) of the bubbles as function of time in the 'Base' simulation.

in agreement with observations that permit any value of the gap size below ~ 2 kpc (Su et al., 2010).

The top left panel of Figure 2.4 shows the SPH particle pressure versus their cylindrical radius (defined as $r_{\mathrm{cyl}}^2 = x^2 + y^2$) selected at a slab of gas with $1 < |z| < 2.5$ kpc at $t = 1$ Myr, roughly corresponding to the midplane (i.e. half-height) of the bubbles at that age. I observe that the difference in pressure within the bubble and outside is greater than two orders of magnitude. This excess pressure continues to drive the expansion in directions both parallel and perpendicular to the Galactic plane long after the quasar has switched off.

The top right panel of figure 2.4 presents the same as the top left figure but at the end of the simulation and for a slab of material at a larger $|z|$ ($4.5 < |z| < 6$ kpc, corresponding roughly to the middle of the bubble that has now risen further from the Galactic plane at $t = 6$ Myr). Note that by $t = 6$ Myr, the gas pressure inside the bubble has dropped by two orders of magnitude; the pressure of the surrounding ISM is also lower, but only by about a factor 10, so the pressure difference between the bubble and its surroundings is much smaller. Consequently, the bubble expansion is much slower, as seen in Fig. 2.5 and the bottom panel of Fig. 2.3. The vertical expansion of the bubbles persists for longer due to residual momentum in the gas and buoyancy (see the last two columns in Table 2.1).

2.5.1.3 Feedback effects on the CMZ

In the simulation, I find that the CMZ is not dispersed by the outflow, a result consistent with the analytical prediction (cf. Section 2.3.3). However, the quasar wind is powerful enough to displace the inner ~ 120 pc of the CMZ to larger radii, resulting in formation of a dense thin ring (Figure 2.6, top left).

The average radial expansion velocity of the inner parts of the CMZ, $v_{\mathrm{r,CMZ}} \sim 100$ km/s,

is larger than the sound speed in its gas ($c_\mathrm{s} \sim 20 - 40$ km/s, for $H/R = 0.125$ and 0.25 respectively) and comparable to its rotational velocity. Therefore some of the CMZ gas is shock-heated to $T \sim 10^6$ K and expands vertically. This allows the quasar wind to ablate the outer surfaces of the CMZ further. Gas from these regions fills the voids in the halo (cf. Sections 2.5.1.1 and 2.5.1.2, above). This process, however, removes only a small amount of mass: by the end of the simulation, the CMZ mass (defined as the gas mass within a radius 250 pc in the Galactic plane and within $z = \pm 100$ pc) has decreased by less than 5%.

I would like to note another more significant dynamical effect of the Sgr A* outflow on the CMZ that re-shapes the initial disc configuration into a ring-like one. The outward force and pressure of quasar wind cause significant radial mixing in the CMZ. For example, some of the CMZ gas on the inner face of the disc is sent outward by the wind just above the surface of the outer regions of the disc, but stalls later on and falls back on the CMZ in the outer regions. This failed outflow has low angular momentum in comparison to gas in the outer disc. The angular momentum of the CMZ gas is then well mixed up. This establishes a narrow distribution of specific angular momentum – a ring. Note that this mechanism of ring formation is similar in spirit to that found by Hobbs et al. (2011) in their simulation S30, although there shocks between material with different angular momentum were due to initial conditions in the collapsing gas shell rather than quasar feedback.

Subsequently, the ring slowly relaxes and spreads back somewhat into a disc configuration due to viscous stresses; however, the viscous timescale for this to happen at $R = 100$ pc is $t_\mathrm{visc} \sim 10^8 \, (0.1/\alpha)$ yr for $H/R = 0.25$, where α is the standard Shakura and Sunyaev (1973) viscosity parameter. This is much longer than the timescales I am interested in, and thus unsurprisingly the ring persists until the end of the simulation (Figure 2.6, bottom).

Since the disc is only marginally gravitationally stable at the start of the simulation, it comes as no real surprise that the ring becomes more unstable than the original disc. As a result, some spiral density waves are visible in the top right panel of Fig. 2.6. Furthermore, a very massive dense clump forms at $t \sim 3.5$ Myr and there are hints of another forming by the end of the simulation at a position $\{x, y\} \sim \{80, -20\}$ pc. The radius of the clump is $r_\mathrm{cl} \sim 5$ pc and its mass $m_\mathrm{cl} \sim 10^7 \, \mathrm{M_\odot}$. Its density is then $n_\mathrm{cl} \sim 7 \times 10^5$ cm^{-3}, ~ 500 times greater than the background potential density at the clump's radial distance $R \simeq 100$ pc and similar to that of dense star forming molecular cloud cores. Due to the adopted temperature floor and lack of resolution in the simulations, the cloud cannot fragment into smaller globules, but one would obviously expect such an object to be unstable to gravitational collapse. The result would presumably be a massive star cluster. The orbit of the clump around Sgr A* is mildly eccentric ($e \sim 0.2$). This may be interesting as a
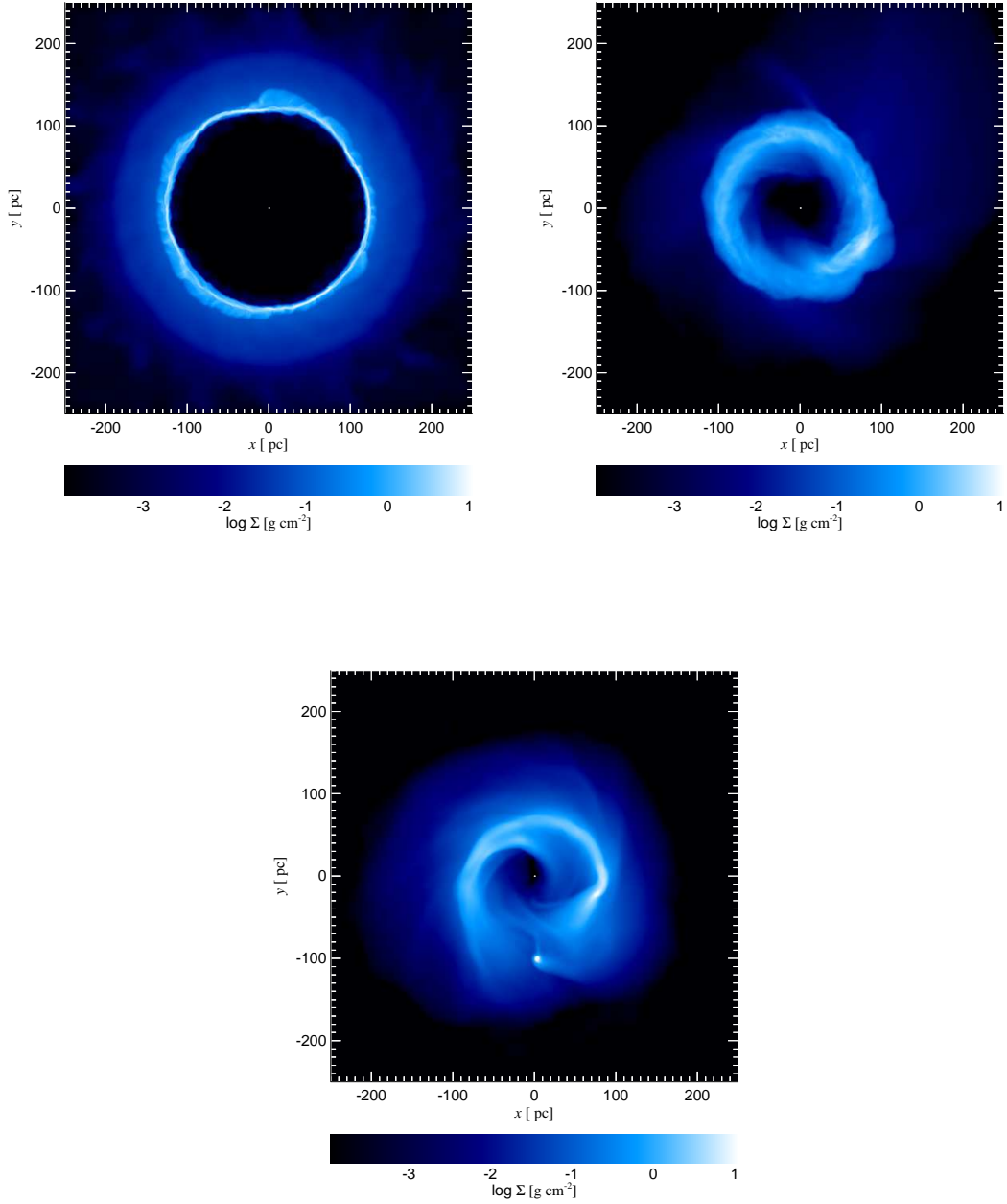
Figure 2.6: Density of gas in the central 250 pc of the 'Base' simulation at $t = 1, 3$ and 6 Myr (clockwise from top left), as seen from above the Galactic plane. The inner regions of the CMZ are strongly affected by the quasar activity, forming a ring (top left panel) which persists for several Myr (top right panel) while slowly spreading radially and developing unstable spiral filaments (bottom panel). A self-gravitating clump forms at $t = 3.5$ Myr, with another about to form by the end of the simulation. The total mass of the CMZ remains almost constant throughout the simulation.

potential route to formation of the Arches cluster which has a rather non-circular orbit (Stolte et al., 2008) in particular, but it may be also relevant to the origin of other young Galactic Centre star clusters and GMCs (cf. further discussion in Section 2.6.7.3).

2.5.2   Dependence on the ambient gas density

The ambient gas density before Sgr A* quasar outburst is a free parameter of the model. Therefore, I varied f_g to see how the conclusions depend on this parameter. A fourfold increase in f_g (Simulation 'Fg-high', Fig. 2.7, top left) results in a reduction of the bubble height by $\sim 40\%$ for the same t_q. This is consistent with the analytical prediction from equation (2.10) and can be understood in terms of the larger gas weight, which for an isothermal distribution is independent of radius and is

$$W_g = \frac{4 f_g \sigma^4}{G} \tag{2.20}$$

(King, 2003, 2010b). Denser gas weighs more, therefore it requires more energy to be lifted to the same height. Since the energy input is the same in both cases, higher values of f_g result in lower height reached by the bubbles. In fact, in simulation 'Fg-high', formally, the stalling radius of the bubble is $R_{stall} \sim 10$ kpc, similar to the size of the observed bubbles. However, the stalling time is $t_{stall} \sim 50$ Myr, which is much greater than the time since the hypothesized Sgr A* outburst. This shows that relatively high values of f_g are definitely disfavored within the present model of a recent outburst origin for the *Fermi* bubbles (unless perhaps t_q is much longer than a 1 Myr; but see Section 2.5.3).

Conversely, a simulation with a lower gas density initial condition ('Fg-low', Fig. 2.7, top right) produces a bubble that is $\sim 40\%$ taller, but its interior temperature is rather low, blurring the distinction between the bubble and its surroundings. Furthermore, the lower density bubble rises further from the Galactic centre, producing a detachment $h_b > 2$ kpc, inconsistent with the data (Su et al., 2010). These disagreements allow me to exclude the possibility of a significantly lower gas fraction in the halo as well.

The simulations show that the width of the bubbles, on the other hand, is almost independent of the ambient gas density. This is probably because the lateral expansion of the bubble is governed not only by the thrust from the outflow, but also by the pressure balance on both sides of the bubble (Fig. 2.4, top left and top right panels). The ambient gas pressure increases with higher f_g, but so does the pressure inside the cavity due to lower bubble volume. The two changes cancel each other out and the pressure inside the bubbles remains several orders of magnitude greater than in the external medium, leading to lateral expansion. Additionally, this expansion happens on an approximately dynamical timescale, which is given by the properties of the background potential and is also independent of f_g.
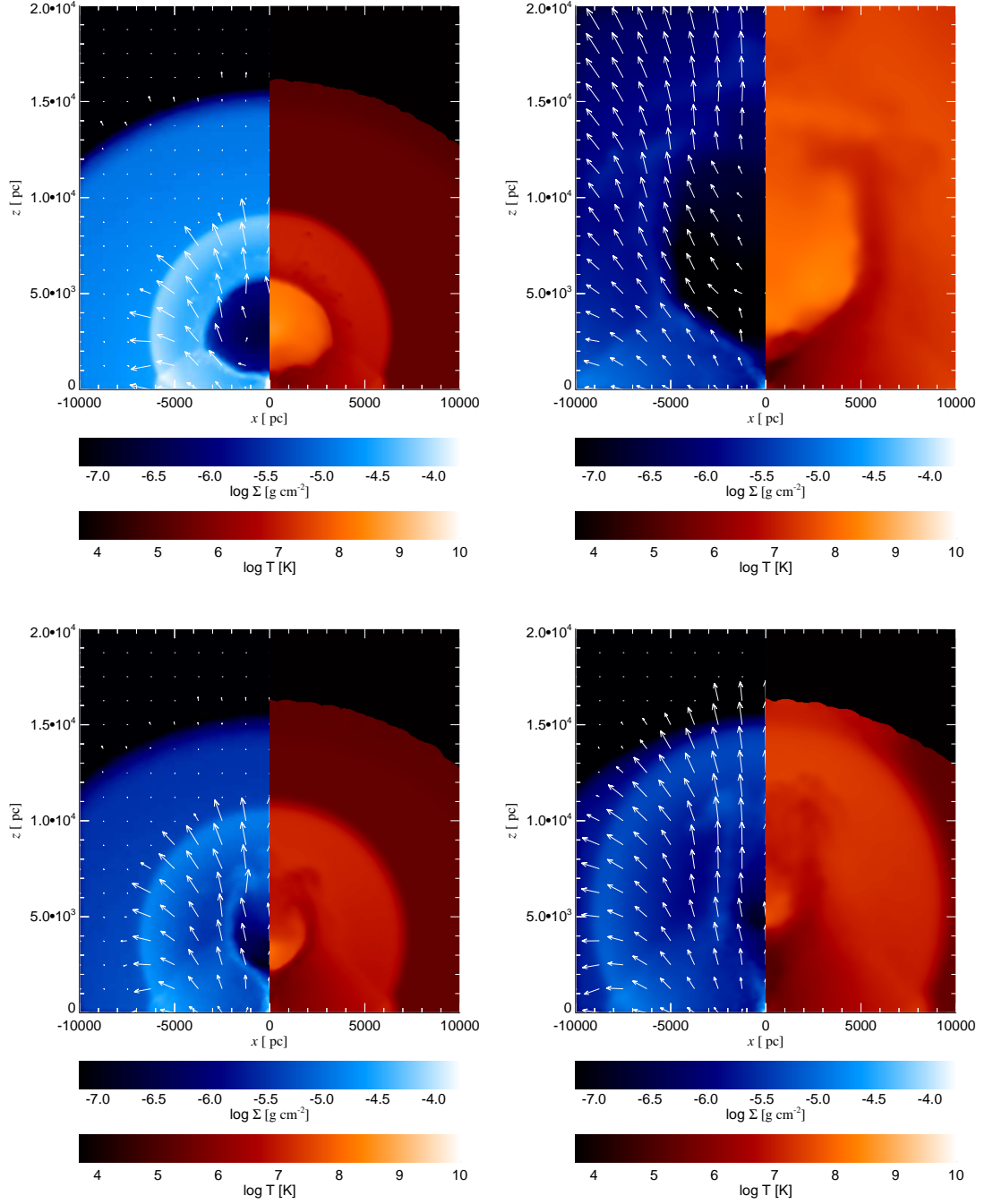
Figure 2.7: Density and temperature plots at $t = 6$ Myr of simulations with varying parameters. **Top left**: higher gas fraction $f_{\mathrm{g}} = 4 \times 10^{-3}$ ('Fg-high'). **Top right**: lower gas fraction $f_{\mathrm{g}} = 4 \times 10^{-4}$ ('Fg-low'). **Bottom left**: lower quasar outburst duration $t_{\mathrm{q}} = 0.3$ Myr ('Tq-low'). **Bottom right**: lower quasar outburst duration $t_{\mathrm{q}} = 0.3$ Myr and lower gas fraction $f_{\mathrm{g}} = 4 \times 10^{-4}$('Both-low').
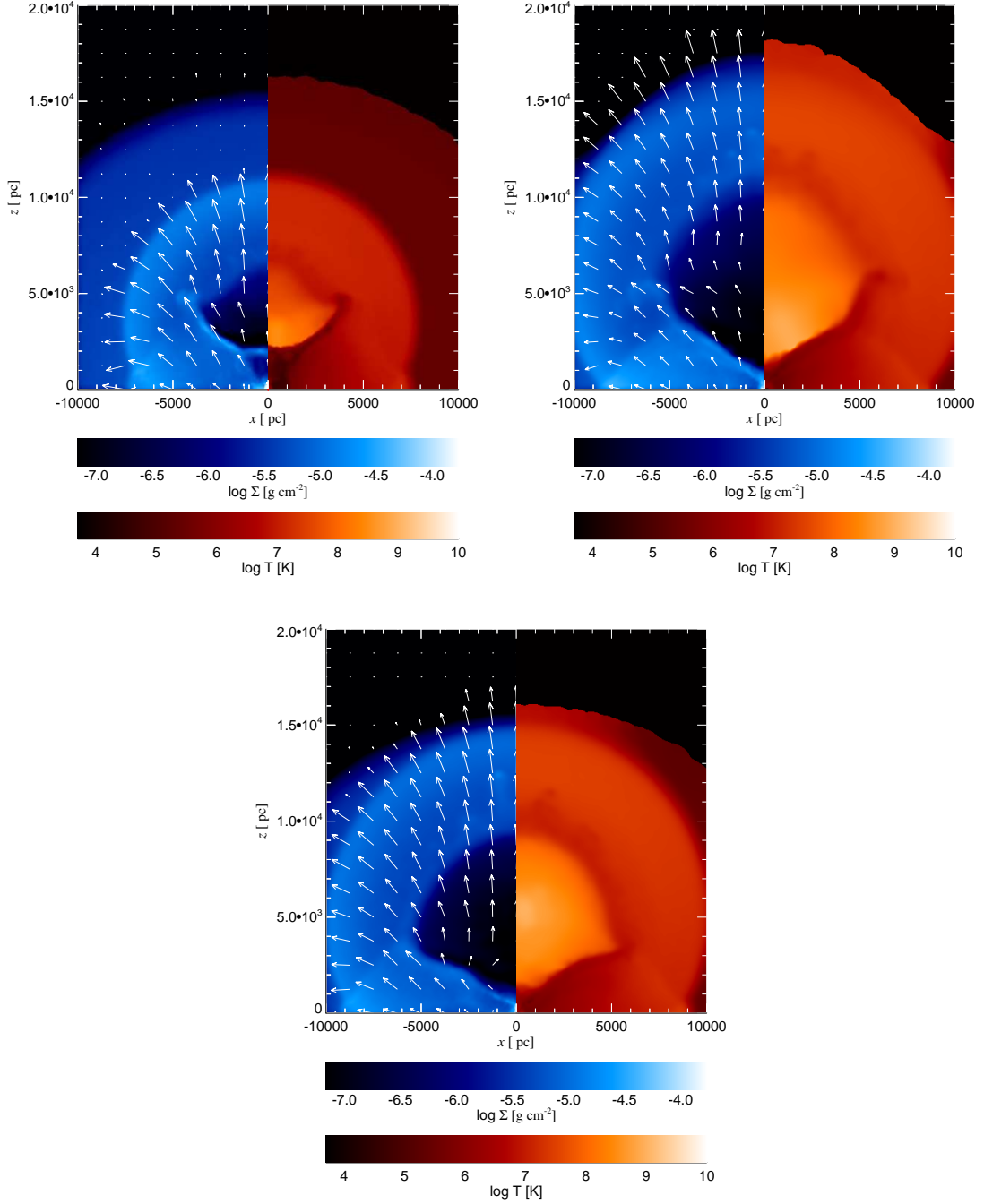
Figure 2.8: Density and temperature plots at $t = 6$ Myr of simulations with varying parameters. **Top left**: CMZ mass decreased by a factor 10 ('Mc-low'). **Top right**: CMZ aspect ratio decreased to $H/R = 1/8$ ('Hr-low'). **Bottom**: a different heating-cooling prescription has been used ("Cool').

2.5.3 Dependence on the outburst duration

I now explore how simulation results depend on the outburst duration. Simulation 'Tq-low' (see Table 1) is identical to the 'Base' simulation except there I set $t_q = 0.3$ Myr. As expected, lower t_q results in physically smaller bubbles (see Fig. 2.7, bottom left). Due to a smaller amount of energy injected and a longer duration of adiabatic expansion phase after quasar switch off, the contrast between the temperature and density in the bubble interior and the surrounding shell is also smaller. The bubbles have lower densities (effective $f_g \sim 4 \times 10^{-4}$, compared with the ambient $f_g \sim 10^{-3}$) and somewhat higher temperatures ($T_{bub} \sim 10^7$ K) than the surroundings, and thus rise buoyantly away from the centre, resulting in large ($\gtrsim 3$ kpc by 6 Myr) separations of the bubbles from the centre. Vertical expansion of the bubble, however, is slower than in the 'Base' simulation; the outer edges of the bubbles reach only $\sim 5 - 6$ kpc by the end of the simulation. In addition, the bubble width is significantly smaller than in the 'Base' simulation, since a lower energy input results in a lower pressure inside the bubble, therefore lateral expansion is also slower.

This result provides a rough lower limit to the quasar outburst duration required to inflate the bubbles: $t_q > 0.3$ Myr, and quite likely $t_q \sim 1$ Myr. This is compatible with the analytical results, where I found $t_q > 2.5 \times 10^5$ yr from morphological arguments (cf. Section 2.3.2). I discuss this point further in Section 2.6.8.

Given that a lower value of t_q produces smaller bubbles, while a lower value of f_g increases their size (See Section 2.5.2), is it possible that reducing both t_q and f_g may yield as good or better morphological fit to the observed bubbles as the 'Base' simulation? I run a simulation to test this idea (see simulation 'Both-low' in Table 2.1), but find results incompatible with observations. The bottom right panel of Figure 2.7 shows the surface density and temperature projections at the end of the simulation. While the height of the bubbles is comparable to that found in the 'Base' simulation, the width is too narrow. Also the gap between the Galactic centre and the lower edge of the bubbles is too large, and the morphology of the whole region appears too non-uniform compared with the observations by Su et al. (2010).

Increasing both t_q and f_g simultaneously by a factor larger than a few is also not a viable option. Morphologically, had the CMZ been able to withstand onslaught from Sgr A* feedback for longer, the dynamics of the gas may have produced reasonably shaped hot bubbles. But I am already using a CMZ mass that corresponds to the upper limits derived from observations (Morris and Serabyn, 1996), and even with $t_q = 1$ Myr the CMZ is significantly affected in the 'Base' simulation. It seems evident that increasing t_q further may do too much damage to the CMZ, i.e., drive most of it to much larger distances from the Galactic Centre than is currently observed. Therefore I think that t_q longer than ~ 1 Myr is not very likely, although there remains a possibility that the current CMZ

is only a remnant of an even more massive gas disc that preceeded the Sgr A* quasar outburst.

2.5.4   Dependence on the CMZ properties

Having checked the effects of varying the halo and quasar parameters, I now vary the properties of the CMZ. In simulation 'Mc-low', I reduce the CMZ mass by a factor of 10, making it smaller than the current observational estimates ($M_{\rm CMZ} \sim 3 - 5 \times 10^7$ M$_\odot$; Dahmen et al., 1998; Pierce-Price et al., 2000).

The results are shown in Fig. 2.8, top left. Comparing the figure with the right panel of Figure 2.3, note that the shape of the bubbles and the shocked region is closer to spherical in the case of a less massive CMZ. Although the lower CMZ mass still yields a weight ~ 5 times larger than what the quasar outburst should be able to lift, the vertical density stratification in a homogeneous disc makes a large part of the CMZ diffuse enough to be blown away. The rest of the CMZ is shock-heated to higher temperatures than in the 'Base' simulation and begins to expand vertically, providing more material that can be removed by the wind. As a result, most of the CMZ is blown away by ~ 0.7 Myr in simulation 'Mc-low', and the outflow proceeds quasi-spherically for the last 0.3 Myr of the quasar activity. Although almost all of this material eventually accretes back onto the reforming CMZ disc after the quasar has switched off, the effects on the diffuse "halo" gas are profound. The bubble height is $\sim 40\%$ lower, their width is $\sim 20\%$ smaller and the bubbles are significantly detached from the Galactic centre. This simulation does not appear to match the morphology of the *Fermi* bubbles as well as the 'Base' simulation does.

I next check the influence of the CMZ geometry by reducing its scale height to yield the geometrical aspect ratio of $H/R = 0.125$, with a corresponding decrease in the temperature floor of the simulation ('HR-low', Fig. 2.8, top right). This value is smaller than the CMZ aspect ratio favored by the current observations ($H/R \sim 0.15$; Pierce-Price et al., 2000; Jones et al., 2011), so that the simulations effectively cover all the reasonable parameter space in terms of H/R for the CMZ.

I find no qualitative difference between simulations 'HR-low' and 'Base'. This suggests that even if the exact geometry of the CMZ plays a role in determining the bubble shape, the magnitude of this effect is quite limited. In all simulations, the bubbles are collimated much more strongly than pure shielding by the CMZ would suggest (the opening angle of the bubbles is $\Omega_{\rm b} \sim 0.4 \times 4\pi$, while the solid angle not obscured by the CMZ in the 'Base' simulation is $\Omega_{\rm CMZ} \sim 0.8 \times 4\pi$), therefore this lack of difference is not particularly surprising.

2.5.5   Effect of the heating-cooling prescription

Simulation 'Cool' is identical to the 'Base' simulation, except that I use a physically motivated optically thin quasar heating-cooling prescription (Sazonov et al., 2005) instead of the standard Sutherland and Dopita (1993) one, as in the other simulations in this Chapter. The prescription is based on a fit to the radiative heating and cooling rates of the gas illuminated by a typical quasar radiation field. The radiative processes include photoionization heating, Compton and inverse-Compton processes, bremsstrahlung and line cooling, and assume an optically thin medium, which is well justified for the low column densities that I find in this paper, $\Sigma \lesssim 10^{-4}$ g cm^{-2}. The only region where gas may become optically thick to X-rays from Sgr A* is the midplane of the CMZ disc. However, I find that the higher density gas is able to cool efficiently anyway, thus staying close to the imposed temperature floor of $T = $ a few $\times 10^4$ K in any event.

The overall effect of changing the heating-cooling prescription on the large scale gas distribution is small (Fig. 2.8, bottom). The bubble interior is $\sim 50\%$ hotter ($T_{\mathrm{bub}} \sim 3 \times 10^8$ K as opposed to 2×10^8 K in the 'Base' simulation), most likely due to less efficient cooling in the adopted prescription at $t > t_{\mathrm{q}}$. The temperature of the outer shell is practically the same. Morphologically, this difference results in bubbles that have $\sim 10\%$ lower height and practically the same width, although the KH-unstable ripples (cf. Section 2.5.1.2) are missing. The bubbles are also somewhat less collimated, as the material close to the Galactic plane is able to cool down more efficiently and collapse to higher densities. In general, however, the bubbles look rather similar. This shows that the results are not very sensitive to the details of gas heating and cooling. This finding is also consistent with the analytical predictions of King (2010b) and King et al. (2011), where by construction an energy-driven outflow occurs when cooling of the shocked wind and the shocked ISM becomes inefficient; I comment on this result further in Section 2.6.3. The effect of the X-ray heating from Sgr A* on the CMZ material is even smaller than that on the diffuse ambient gas, as explained above.

It should be noted that this insensitivity to quasar photo-ionisation heating and radiative cooling is to be expected due to the low density and a rather short duration of Sgr A* outburst compared with typical cosmological conditions (Sazonov et al., 2005). At higher densities I would expect the structure of the ambient gas to be significantly dependent on the details of the cooling function employed in the simulations.

2.6   Discussion

2.6.1   Summary of results

In general, the numerical simulations agree with the analytical calculations and confirm the hypothesis that an Eddington-limited outburst of Sgr A* outflow is a promising way

of explaining the morphology of the observed *Fermi* bubbles. Starting with the model for AGN feedback developed to explain the $M_{bh} - \sigma$ relation for classical bulges and elliptical galaxies (King, 2003, 2005), the "typical" initial conditions for numerical simulations of AGN feedback (Nayakshin and Power, 2010) needed to be amended only to account for (a) the lower present day gas content of the Milky Way (i.e., smaller gas fraction f_g); (b) the presence of a massive gas disc, the CMZ, in the plane of the Galaxy in the central 200 pc; (c) a finite duration of Sgr A* outburst, which is a free parameter of the model, and is small compared to the dynamical time in a host galaxy bulge.

Given this setup, I confirm the analytical prediction that a spherically symmetric outflow from Sgr A* is collimated by a geometrically thin CMZ disc in directions perpendicular to the Galactic plane. The outflow then produces two teardrop shaped cavities that have sizes similar to the observed γ-ray emission features. I varied the free parameters of the model – the quasar outburst duration t_q and the gas fraction f_g – to constrain their values to $t_q \approx 1$ Myr and $f_g \approx 10^{-3}$. The former is plausible and has interesting implications for Sgr A* feeding (cf. Section 2.6.8 below). The latter is poorly constrained observationally but consistent with estimates by McKee (1990) and Sofue (2011).

The opening angles of the bubbles as seen from Sgr A* are $\Omega_b \sim 0.4 \times 4\pi$. This is significantly smaller than the solid angle not obscured by the CMZ in the 'Base' simulation ($\Omega_{CMZ} \sim 0.8 \times 4\pi$), showing that CMZ casts a larger "feedback shadow" than could be expected based on its geometrical aspect ratio alone. This difference is caused by the following two effects. First of all, the CMZ not only hinders the outflow propagation directly through it, but also "reflects" a part of the outflow. The thermally driven outflow of hot gas ablated from the CMZ surfaces away from the Galactic plane redirects the gas flow lines towards vertical directions. Secondly, the bubbles rise due to buoyancy, and cooler material streams to fill the void along the Galactic plane, further reducing the opening angle of the bubbles. I did not consider either of these effects in the analytical calculations, but their presence generally improves overall correspondence between model results and observations. Early analytical work on similar problems (Kompaneets, 1960; Moellenhoff, 1976) found that the outflows are collimated into more column-like shapes than I find in the simulations. However, these papers used considerably different distributions for the ambient medium, which strongly affect the results. Furthermore, the rapid cooling of the CMZ in my simulations provides extra collimation which was not found by the previous authors.

In addition, although I was not originally interested in the evolution of the CMZ due to Sgr A* feedback – the role of the CMZ in the simulations was to stop and redirect the quasar wind only – I found several CMZ-related results interesting from an observational point of view: (a) re-shaping of the CMZ into a ring-like structure, perhaps explaining recent *Herschel* observations that the CMZ is a dusty ring rather than a disc; (b) an

induced star formation mode in the CMZ which is triggered by Sgr A* feedback. These points are further discussed in Section 2.6.7.

I now make a detailed comparison of the simulation results to observations.

2.6.2 Gas mass within the bubbles

In the simulations presented in this Chapter, two cavities corresponding to the observed *Fermi* bubbles are filled with hot and diffuse gas. The observationally estimated mass of gas within the bubbles ($M_{\text{bub}} \sim 10^8$ M$_\odot$; Su et al., 2010) is much greater than the mass of the shocked wind in the model. The latter, from analytical arguments in Section 3.2, is $M_{\text{w}} \simeq \dot{M}_{\text{Edd}} t_{\text{q}} \sim 8 \times 10^4$ M$_\odot$ for $t_{\text{q}} = 1$ Myr. The mass contained inside the cavities is $M_{\text{bub,sim}} \sim 6 \times 10^5$ M$_\odot$ for the 'Base' simulation. The density of gas within the bubbles ($n_{\text{bub}} \sim 3 \times 10^{-5}$ cm^{-3}) is also much lower than the one typically adopted in spectral modelling of the bubble emission ($n \sim 10^{-2}$, Su et al., 2010; Crocker and Aharonian, 2011).

I believe that these simulations under-predict the gas density inside the bubbles which would otherwise be obtained in a more sophisticated simulation. I use a one-phase model for the ambient medium, whereas observations of gas in the Milky Way show that it is multi-phase (Dame et al., 2001). I would thus expect some cold and warm gas to be present even at large heights above the disc before Sgr A* "turns on". Much like in supernova shocks expanding into the ambient medium, molecular clouds embedded in the ambient gas are expected to be overtaken by the quasar wind and later evaporate inside the bubbles, increasing the hot gas density there at late times (e.g. McKee and Cowie, 1975). In addition to that, having strong density inhomogeneities in the ambient medium should provoke strong Rayleigh-Taylor instabilities (King, 2010a) during the quasar outburst event; I discuss these in Section 2.6.5 below. These may allow formation of dense filaments resilient to Sgr A* feedback that are left behind the shock just like the molecular clouds discussed above. I believe that these differences do not affect the large-scale gas dynamics within our simulations.

2.6.3 Bubble energy content

The total energy input by the quasar into the system is

$$E_{\text{in}} \simeq \frac{\eta}{2} L_{\text{Edd}} t_{\text{q}} \simeq 8 \times 10^{56} t_6 \text{ erg}, \tag{2.21}$$

where t_6 is quasar activity time in Myr and $\eta/2 = 0.05$ is the coupling efficiency of the energy-driven wind (eq. 2.3). As mentioned in Section 2.3.2, E_{in} is significantly larger than the observational estimate of the total gas energy content of the bubble: $E_{\text{bub,obs}} \sim 10^{54-55}$ erg (Su et al., 2010). However, in the simulations, the injected energy
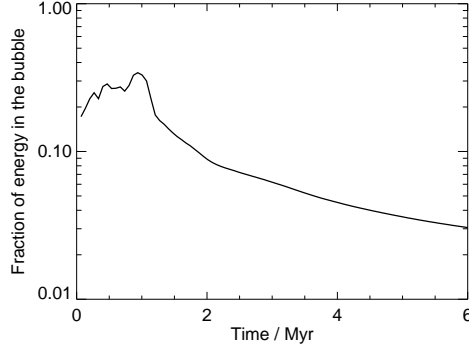
Figure 2.9: Time evolution of the fraction of energy input into the system by the quasar wind that is retained inside the bubbles. The rest of the energy is contained in the shell of shocked expanding ambient gas.

E_{in} is split between the bubble and the surrounding shell. Even when the quasar is active, analytical calculations show that only $1/3$ of the input energy remains inside the bubble (Zubovas and King, 2012, also Chapter 4 of this Thesis), and this value should decrease after the quasar has switched off, as the bubble cools due to expansion.

To quantify this further, I computed the fraction of energy injected into the ambient gas by Sgr A* and retained by the bubble in the 'Base' simulation as a function of time (other simulations show similar results). To this end, I first compute the sum of kinetic and thermal energy for all the gas particles in the simulation, $E_{tot}(t)$. I exclude in this calculation the gravitational potential energy of gas because for most SPH particles in the calculation changes in the latter are small compared with the changes in the kinetic and thermal energy; additionally, cooling is not very efficient in a low-density energy-driven flow, therefore the changes in results due to this channel are also negligible. I then define the energy content of the gas within the bubble, $E_{bub}(t)$, as the sum of kinetic and thermal energy of the gas inside the bubble. The fraction of energy retained in the bubble is thus defined as

$$\epsilon_{E,in}(t) \equiv \frac{\Delta E_{bub}}{\Delta E_{tot}} = \frac{E_{bub}(t) - E_{bub}(0)}{E_{tot}(t) - E_{tot}(0)} \ . \tag{2.22}$$

Figure 2.9 presents the evolution of $\epsilon_{E,in}$ with time. While the quasar is active, the fraction of energy retained inside the bubble grows slightly and fluctuates around the analytically derived value of $1/3$. Once the quasar switches off, the expanding bubble cools and transfers most of its energy to the surrounding shell, so that by $t = 6$ Myr, only $\sim 3\%$ of the total energy input is retained inside the bubble. Hence the total energy content of the bubbles by the end of the simulation is

$$E_{bub} \sim 0.03 E_{in} \simeq 2.5 \times 10^{55} \ t_6 \ \text{erg}, \tag{2.23}$$

a value similar to but still a little larger than the observed one. This energy is contained predominantly in thermal gas motions and cosmic rays, rather than the bulk motion of the gas (the sound speed in the bubble gas is $c_{\rm s,bub} \sim 3000$ km/s $> v_{\rm v}$ of bubble expansion), and so is in principle visible to observations.

A further decrease in the bubble energy content may be caused by radiative cooling. To check this, I consider the evolution of $E_{\rm tot}(t)$ and find that after $t = t_{\rm q}$ it is conserved to within a few %. Adding a reasonably parametrised (using $r_{\rm s} = 1$ kpc as a scale radius) value for the gas potential energy does not change the result either. Therefore the importance of cooling on the total energy content is minimal and does not affect the previous considerations.

2.6.4   Expected radiation from the bubble

The main emission components of interest are the γ-ray emission from the the lobes (Su et al., 2010), a tentative microwave feature coincident with the bubbles identified in the WMAP all-sky maps (Finkbeiner, 2004; Su et al., 2010) and an X-shaped feature visible in the X-rays closer to the Galactic plane, coinciding with the edges of the bubbles, known as the "ROSAT limbs" (Snowden et al., 1997). I discuss each of the three components in turn.

While I do not model cosmic ray (CR) particles in the simulations, I note that astrophysical shocks are known to accelerate electrons, protons and other particles to CR energies (Blandford and Eichler, 1987) in a variety of environments and put as much as $\sim 10\%$ of the blast wave energy into the high energy particle component in the case of supernova shocks. I certainly do not see an obvious reason why shocks driven by an even faster outflow from a quasar would be less efficient in producing CRs than supernovae.

Two competing explanations for the origin of the γ-ray emission from the *Fermi* bubbles were suggested in the literature to date. Crocker and Aharonian (2011) suggested that the emission is powered by CR protons through *pp* collisions with the plasma in the bubbles. In this scenario, $\sim 10^{39}$ erg s^{-1} of energy is injected into the bubbles in the form of CRs for $\sim 10^{10}$ yrs to achieve saturation in the system (cf. also Crocker, 2011). This yields $\sim 3 \times 10^{58}$ erg in CR energy alone. This is some 3 orders of magnitude larger than the thermal energy retained within the bubbles in the 'Base' simulation (equation 2.23). Therefore I conclude that the model is very unlikely to produce a bright enough γ-ray emission if emitting particles are hadrons.

On the other hand, Mertsch and Sarkar (2011) explore the possibility that electrons accelerated by shocks in turbulent plasma inside the bubbles can reproduce the spectral features, as well as the constant surface brightness profile. They find that this acceleration process can continuously replenish the energetic electron population, overcoming the problem of rapid electron cooling via the inverse-Compton process. The cooling time due

to both IC and synchrotron losses is less than 5 Myr for 100 GeV electrons at $z = 5$ kpc above the Galactic plane (Fig. 28 and Section 7.1 in Su et al., 2010). Since the current γ-ray luminosity of the bubbles is $\sim 4 \times 10^{37}$ erg s^{-1}, and the age of the bubbles is 6 Myrs in the model, I conclude that at least $\sim 10^{52}$ erg of CR electrons is required to explain the *Fermi* Bubbles, and somewhat more if I account for continuous replenishment from plasma turbulence. This would be a very small fraction of the bubble energy content in the present model, and at least on that basis is possible.

The origin of "continuous" shock driving inside the bubbles can be naturally explained by the model. Since the *Fermi* bubbles are still expanding at the end of the simulations, I expect that the whole volume of the cavities inflated by the quasar outburst is still filled with shocks produced by the small-scale Rayleigh-Taylor instabilities at the contact discontinuity, which I do not resolve in the simulations (Section 2.6.5), and the strong differential motions of the unresolved clouds evaporating inside the bubbles (Section 2.6.2). These instabilities could continue to inject energy into the shocks inside the bubbles (see Figure 2 in Mac Low et al., 1989). As noted in Section 2.6.2, a higher resolution modelling that includes a multi-phase description for the ambient pre-shock gas is likely to result in strong Rayleigh-Taylor instabilities of the wind shock front during the quasar outburst event (King, 2010a). This should let cold gas filaments fall into the bubble's interior due to gravity, leading to high Mach number shocks. Protons and electrons could thus be continuously accelerated on these shocks now, as suggested by Mertsch and Sarkar (2011).

The observed microwave haze spatially coincides with the *Fermi* bubbles, although its intensity decreases with height above the Galactic plane, especially in the southern bubble (see the bottom right panel of Figure 18 in Su et al. 2010 and the left panel of Figure 5 in Dobler 2012). The luminosity of synchrotron emission from cooling electrons decreases with height above the plane possibly due to an expected decrease in the magnetic field strength. I believe that same electrons responsible for the γ-ray emission may be responsible for the WMAP haze. In this regard, my model is similar to that of Biermann et al. (2010), where the authors require fast diffusion and recent origin ($t \lesssim 10^7$ yr) of the CR particles responsible for the haze emission.

The ROSAT-observed X-ray background in the region of the *Fermi* bubbles is composed of X-shaped ridges coincident with the lower limbs of the bubbles, most clearly visible in the hard (1.5 keV) band of the instrument, and a cavity in soft-band X-ray emission coincident with the bulk of the bubble area (Snowden et al., 1997; Su et al., 2010). The spatial coincidence of the features suggests a common origin.

In the simulations, gas inside the bubbles has temperatures as high as $\sim 10 - 20$ keV (see Figure 2.4, bottom) and so most of its thermal emission is harder than what ROSAT would detect. This could then explain the deficit of soft X-ray emission from within the bubbles. The shocked ISM (see Section 2.6.6 below) is heated to temperatures of a few

times 10^7 K, (although that is expected to scale as $\propto \sigma^2$, so may vary somewhat if the model for the potential in the inner 10 kpc of the Galaxy is varied). The shocked shells around *Fermi* bubbles should then be best visible in the harder ROSAT bands. X-ray emissivity scales as $\propto n^2$, where n is gas particle density. The latter tends to be larger close to the Galactic plane due to superposition of the shells around the two bubbles (Figure 2.3, bottom) and vertical stratification. Therefore I would expect the lower limbs of the shells to be brighter in X-rays, as observed.

2.6.5 Stability of the outflow

The simulations presented in this Chapter show the large-scale outflow proceeding in a stable manner, without developing any small-scale features, except for a single ripple (see Figure 2.3, top right and bottom) at around the middle of the bubble height. However, formally both the inner shock of the quasar wind and the contact discontinuity between the wind and the ISM are Rayleigh-Taylor unstable (King, 2010a). Here, I investigate the reasons why I do not find this instability, or any of several others, in the simulations, although one may expect to see them in similar numerical work.

2.6.5.1 Rayleigh-Taylor instabilities

Figure 2.4, bottom, shows that even by the end of the 'Base' simulation, gas inside the bubble is significantly less dense than in the surroundings ($f_{\mathrm{g,bub}}/f_{\mathrm{g,shell}} \simeq 10^{-2}$). As a result, the contact discontinuity is Rayleigh-Taylor unstable. The growth timescale of the instability depends on the associated wavelength λ:

$$t_{\mathrm{RT}} = \left(\frac{2\pi\lambda}{g} \frac{\rho_{\mathrm{shell}} + \rho_{\mathrm{bub}}}{\rho_{\mathrm{shell}} - \rho_{\mathrm{bub}}} \right)^{1/2}. \tag{2.24}$$

In the case considered here, the ratio of density sum and difference is $\simeq 1$, and the gravitational acceleration is $\simeq \sigma^2/R$, giving

$$t_{\mathrm{RT}} \simeq \frac{R}{\sigma} \left(\frac{2\pi\lambda}{R} \right)^{1/2}. \tag{2.25}$$

For a limited growth timescale $t_{\mathrm{gr}} = 6t_6$ Myr I find that there is a maximum wavelength of the perturbation which experiences significant growth:

$$\lambda_{\mathrm{max}} = \frac{(\sigma t_{\mathrm{gr}})^2}{2\pi R} \simeq 40 \; R_{\mathrm{kpc}}^{-1} t_6^2 \; \mathrm{pc}. \tag{2.26}$$

Therefore the only instabilities that grow significantly have very short wavelengths, unless they start to develop while the outflow radius is < 1 kpc.

On the other hand, the linear resolution of the simulations is approximately equal to the typical particle smoothing length, which in the region of interest (i.e. in the bubble and in the shell) is $h_{\mathrm{SPH,sh}} \sim 500$ pc. Therefore the unstable wavelengths that show significant growth are not resolved. In principle, this is a shortcoming of the simulation and of the SPH method in general (Agertz et al., 2007). However, Mac Low et al. (1989) find a very similar result in the case of an expanding *adiabatic* bubble using a grid code ZEUS. Furthermore, these authors do find very strong shell instabilities in the case of a rapidly cooling shocked ambient medium, but even in those cases they find that the large scale dynamics is described surprisingly accurately by the Kompaneets (1960) method that completely neglects the instabilities. Therefore I believe that the simulation results are sufficiently accurate as far as the large-scale dynamics of the bubbles is concerned.

However, as discussed in Sections 2.6.2 and 2.6.4, the RT instabilities may be especially important in the case of an inhomogeneous ambient medium that I do not model here. The RT "fingers" may penetrate deep into the bubble, increasing the average gas density inside it and providing additional shock fronts for the acceleration of CR particles. These issues thus deserve future more detailed investigations.

2.6.5.2 Vishniac instability in the outer shell

The shocked ambient medium may also be prone to pressure-based instabilities similar to those described analytically by Vishniac (1983) and confirmed numerically by Mac Low and Norman (1993). However, this type of instability can only act on a thin shell. This condition requires efficient cooling of the shocked ambient gas. Given the set up I investigate here, the cooling time of the shocked ambient gas is long compared with the total duration of the simulation (Section 2.6.3), therefore I would not expect the outer shell to become unstable.

2.6.5.3 Stability of the CMZ

In the simulations the interface between the CMZ and the outflow does not appear to be strongly unstable. This may be a general deficiency of the SPH algorithm (Agertz et al., 2007), but I note that these possible instabilities are not the primary focus of this Chapter. In addition, the observed CMZ is a highly dynamic irregular structure (Molinari et al., 2011), so these instabilities would not be inconsistent with the observations. I further discuss self-gravitational instabilities of the CMZ in Section 2.6.7.

2.6.6 Bubble edges and the outer ISM shock

The expanding SMBH outflow drives a strong forward shock into the ISM, which is expected to be adiabatic and move with $v_{\mathrm{ISM}} \sim 4/3 v_{\mathrm{e}}$ (Zubovas and King, 2012, also Chapter

4 of this Thesis). Since the shell thickness is initially zero, its vertical extent should also be $r_{\mathrm{ISM}} \sim 4/3 r_{\mathrm{b}}$, i.e. the thickness of the snowplough shell should be 1/3rd of the bubble height. Note that in the simulations, it is somewhat greater: $d_{\mathrm{sh}}/r_{\mathrm{b}} \sim 0.4$. This result is not due to poor resolution. At late times, the thickness of the shell is ~ 10 times greater than the typical SPH particle smoothing length inside it ($h_{\mathrm{SPH,sh}} \sim 500$ pc), therefore I believe the large-scale morphology of the region is well resolved.

The most likely reason for the discrepancy is the fact that the analytical model assumes a continuous quasar outflow driving the shell, whereas in the simulations the quasar turns off at $t = 1$ Myr. As a result the shell is less compressed in the radial direction.

In addition, the one-phase treatment of the ambient diffuse medium (cf. Section 2.6.2) can under-estimate the radiative cooling in the shell. Therefore, a more realistic multi-phase simulation could be expected to have thinner shell enveloping the *Fermi* bubbles.

Simulations also show transition regions at the edges of the bubbles (e.g. at $r_{\mathrm{cyl}} = 4 - 5$ kpc in Figure 2.4, bottom). These are $\lesssim 1$ kpc thick zones where both temperature and density change from the values appropriate for bubble interior to those of the swept-up ISM. The observed bubble edges are $5 - 10^{\mathrm{o}}$ wide, corresponding to a few hundred parsecs, in good agreement with simulation results. However, I must note that the SPH particle smoothing length in these regions is comparable to the region thickness, therefore numerical effects probably dominate the result.

2.6.7 Has Sgr A* feedback affected the CMZ?

The primary goal of this Chapter is investigating whether Sgr A* feedback is a reasonable model for the morphology of the *Fermi* bubbles. In doing so I purposely introduced a very simple model for the CMZ – a $\Sigma(R) \propto R^{-1}$ circular disc in the plane of the Galaxy with mass and size consistent with observations (Morris and Serabyn, 1996). This simple model nevertheless resulted in an interesting transformation and excitation of the CMZ that is worthy of further discussion.

2.6.7.1 The Herschel ring: a feedback-compressed disc?

In particular, I find that, under the strong coercion from Sgr A* feedback, the initial disky configuration of the CMZ attains a morphology more reminiscent of a dense ring (see Section 2.5.1.3 and Figure 2.6). I believe this is a general result of an AGN feedback acting on a disk since the physics behind this "anti-diffusion" evolution of the disk is simple and thus robust.

When the inner regions of the disc are blasted with an outward-directed feedback from the centre, little of the material outflows to infinity; most actually falls back onto the disc at large radii, mixes with gas there, reducing its angular momentum, and thus induces an inward-directed radial flow at those radii. AGN feedback thus serves as an external agent

that forces shock mixing of gas initially located at different radii and carrying different specific angular momenta. An initially broad distribution of angular momentum (a disc) becomes more narrow (a ring).

The slow viscous evolution of the dense ring that is formed by feedback suggests that such a ring should be still present in the GC today. In fact, recent *Herschel* observations of the GC region have revealed a ring-like structure on the scale of ~ 100 pc (Molinari et al., 2011), qualitatively similar to what I find in the simulations. The observed feature is elliptical and offset from Sgr A*. In Section 2.6.7.2 below I discuss how this strongly non-circular and offset structure could be formed in the model.

The fact that the CMZ is only perturbed but not dispersed to infinity is consistent with analytical predictions in Section 2.3.3. Note also that it may seem paradoxical how this very massive gas disc gets evacuated in the inner region and yet Sgr A* continues to accrete from presumably a much smaller disc at the assumed Eddington rate for ~ 1 Myr as in the 'Base' simulation. However, the paradox is easily solved by realising that weight per unit mass of the gas – i.e., acceleration due to gravity – scales as $\propto M(R)/R^2$, where $M(R)$ is the total mass enclosed within radius R. The disc that fed Sgr A* may have had a radius of order $R \sim 0.1$ pc or even less (Nayakshin, 2005; Alexander et al., 2012). The weight of the *accretion disc* of mass $M_\mathrm{d} = 10^5 M_5$ M$_\odot$ is then

$$W_\mathrm{ac} = \frac{G\,\mathrm{M_{bh}}M_\mathrm{d}}{R} = 1.2 \times 10^{36} M_5 \text{ dyn} , \tag{2.27}$$

which is some ~ 20 times larger than that estimated for the CMZ (equation 2.16). It is thus perfectly reasonable that a smaller-scale disk would be too tightly bound to the SMBH to be expelled or even significantly perturbed by feedback, unlike gas at larger radii. Nayakshin et al. (2012a) show in their Appendix that this is a general point.

2.6.7.2 Non-circular orbit of the Herschel ring

Molinari et al. (2011) find that the Herschel ring is offset from Sgr A* and thus the centre of the Milky Way by about 50 pc, which is comparable with the size of the ring itself (see their fFigure 5). Any offset, and especially such a large one, is not naturally expected if the ring is a long-lived structure. While my model shows no offset, note that there may be a natural way to produce that, although further numerical simulations are needed to confirm these ideas.

In particular, I have assumed here that the feedback from Sgr A* is exactly spherically symmetric. This is likely to be an over-simplification. Even if the wind outflow is quasi-spherical on the smallest scales (i.e., hundreds of Schwarzschild radii), on the somewhat larger scales of stellar discs there must be an accretion disc which cannot be readily expelled by Sgr A* feedback as discussed above. Also, the young stellar discs orbiting Sgr A* are

not simple planar structures, with significant warps needed to explain the observed stellar kinematics (Bartko et al., 2009). Large warps also naturally occur in numerical simulations of star forming gas flows (Hobbs and Nayakshin, 2009). Therefore, due to shadowing of Sgr A* feedback by the ~ 0.1 pc gas flow (which may be strongly non-circular), one side of the CMZ may have experienced a different amount of feedback compared with the other side, causing a strong non-axisymmetric perturbation to the CMZ disc and perhaps leading to an offset ring reminiscent of the observed Herschel ring. I note that the asymmetry in the feedback should not be too large over the whole 4π solid angle, however, so as to not result in too asymmetric *Fermi* Bubbles.

Additionally, natural non-axisymmetric density variations in the pre-feedback CMZ may result in outflow within the CMZ proceeding at different velocities in different directions, producing the offset.

2.6.7.3 Induced star formation in the CMZ?

A particularly interesting outcome of the CMZ compression by the outflow is the formation of a dense clump of gas at $t \sim 3.5$ Myr (see Section 2.5.1.3). The large mass, $\sim 10^7$ M$_\odot$, of the clump and its position at $R \sim 100$ pc from the Galactic centre suggest that the observed young Galactic centre stellar clusters (Serabyn et al., 1998; Figer et al., 1999a,b) or some of the largest molecular clouds (e.g. Sgr B2, Scoville et al., 1975; Reid et al., 2009) may have formed this way. Many smaller clumps in the dense ring may be susceptible to star formation; recent IR observations (Yusef-Zadeh et al., 2009; Immer et al., 2012) reveal that the star formation rate in the CMZ during the past ~ 1 Myr was ~ 0.08 M$_\odot$ yr^{-1}. At this rate, all of the CMZ gas would be turned into stars in $\sim 6 \times 10^8$ yr; even if the CMZ was supplied by molecular gas from further out, the whole molecular gas content of the Milky Way would have been turned into stars in ~ 6 Gyr. This suggests that the current star formation rate in the CMZ is higher than the long-term average, further implying a rather recent perturbation, consistent with the results of our simulations. Furthermore, combined *Chandra* and *HST* observations have revealed a population of isolated massive (O and B giant, but also WR) stars in the CMZ (e.g. Mauerhan et al., 2010). These stars are not associated with any of the known clusters and may have formed in small associations. The simulations suggest that while these stars are isolated now, they may have formed coherently in time if not in space due to a single very powerful perturbation produced by Sgr A* quasar outburst that turned the disc into a star-forming ring.

Finally, I note that the strong perturbations to the initially circular orbits of gas in the CMZ by Sgr A* feedback could form gas clumps on eccentric orbit. Indeed, the orbit of the clump found in the 'Base' simulations is mildly eccentric, $e \sim 0.2$. That was obtained in a perfectly azimuthally symmetric simulation; any deviation from this assumption would have likely resulted in an even more eccentric clump. Such eccentric

clump formation mechanism may be relevant to the origin of the Arches cluster which has a rather non-circular orbit (Stolte et al., 2008).

2.6.8 Implications for AGN feeding models

Sgr A* is the closest SMBH, and while its dimness is a familiar (and important) tale that stimulated development of non-radiative models of accretion for low density gas flows near SMBHs (e.g., Narayan et al., 1995; Blandford and Begelman, 1999), little has been known about the past of Sgr A* as an accretion-powered SMBH. This is mainly due to potential difficulties of discovering signs of past Sgr A* activity. Light-echos due to X-ray fluorescence of Sgr A* radiation on molecular clouds is a powerful technique (Sunyaev and Churazov, 1998; Revnivtsev et al., 2004; Terrier et al., 2010) but can only be used to constrain Sgr A* activity up to $\sim 10^4$ yrs at best due to the finite size of the Galaxy and the $\sim 1/R^2$ fading of signals from clouds at large distance R from the Galactic Centre.

However, shocks induced by an outflow from Sgr A* may continue to be visible for approximately a dynamical time of the Galaxy, i.e., $R_{\rm G}/\sigma \sim 50$ Myrs, where I set Galaxy "radius" to be ~ 5 kpc and velocity dispersion $\sigma = 100$ km s^{-1} for illustrative purposes. Therefore, the *Fermi* lobes detected by Su et al. (2010) may be such a "shock-echo" of the past Sgr A* activity. In this Chapter, I required the activity episode of Sgr A* to coincide with the well known star formation event in the Galactic Centre ~ 6 million years ago (Paumard et al., 2006), and found that the model has a number of attractive observational consequences which lend some support to this picture.

If Sgr A* indeed did have an Eddington-limited outburst for as long as ~ 1 Myr, it must have accreted $\sim 10^5$ M$_\odot$ of gas. This is an order of magnitude more than the mass in the stellar discs (Paumard et al., 2006; Nayakshin et al., 2006). The fact that Sgr A* managed to accrete $\sim 90\%$ of the gas from the star-forming accretion disc is highly significant for the general question of how SMBH are fed, and should be explored further as a potential example of an AGN disc that avoided the "star formation catastrophe" in which gas is believed to be turned into stars too rapidly to feed AGN (e.g., Paczynski, 1978; Kolykhalov and Syunyaev, 1980; Goodman, 2003; Nayakshin et al., 2007).

The interpretation of the high efficiency of gas accretion in comparison to star formation is model dependent. On the one hand, it may be evidence that feedback from stars inside the accretion disc is able to stave off star formation for long enough to channel a sufficient amount of fuel to the SMBH (Thompson et al., 2005). Alternatively, the dynamically hot structure of the young stars in the central parsec of the Milky Way is best explained by a non-planar gas deposition event resulting from, e.g., collisions of two massive gas clouds (Hobbs and Nayakshin, 2009), collision between a cloud and the circumnuclear disc, or capture of a large, turbulent giant molecular cloud (Wardle and Yusef-Zadeh, 2008; Bonnell and Rice, 2008). If this is so, a fraction of the gas may have

small enough angular momentum to orbit within the innermost *non self-gravitating* disc region, avoiding the "star formation catastrophe" entirely (King and Pringle, 2007; Nayakshin and King, 2007; Hobbs et al., 2011). In particular, in some of the cases simulated by Hobbs and Nayakshin (2009), the mass of the gas captured inside their inner boundary (a non self-gravitating part of the disc) was comparable with the mass required to fuel the *Fermi*-LAT lobes as found in the simulations in this Chapter.

2.6.9   Uncertainties and deficiencies of this work

As discussed in Section 2.6.4, I model the ambient gas "halo" with a single phase medium, whereas the ISM is expected to be multi-phase (McKee, 1990). The lower density medium, essentially unresolved in the simulations, is probably quite important for the dynamics of the fast outflow from Sgr A* interacting with the gas in the bulge of the Galaxy (see also Section 2.6.2). Therefore some of the conclusions (e.g., the likely quasar phase duration t_q, the geometrical thickness of the shocked shell, etc.) may somewhat depend on the treatment of the ambient medium, and future work is needed to quantify this issue.

Also, a more realistic model for the geometrical arrangement of the diffuse "halo" gas that the outflow interacts with is desirable as this probably affects the eventual shape of the bubbles. In the simulations, I consider a spherical halo mass distribution, whereas in reality, I expect stratification on a large scale, with higher gas density in the Galactic plane than perpendicular to it, and higher density in the bulge than outside. One can make a very simple estimate of the magnitude of this effect by considering the dependence of outflow stalling radius on the gas fraction, which I take here to be the mean gas fraction along a direction of expansion. The analysis in Section 2.3.2 shows that $R_{\text{stall}} \propto v_e^2 \propto f_g^{2/3}$. As the bubble expands in an approximately self-similar fashion (see Section 2.5.1) after the quasar switches off, I estimate that in any given direction $R_{\text{bub}} \propto f_{\text{g,eff.}}^{2/3}$. Therefore a factor of three difference in gas fraction results in approximately a factor of two difference in bubble radius. I hope that future observations of diffuse gas in the bulge of the Milky Way will provide constraints on this part of the model.

The results presented in this Chapter are, as expected, sensitive to the total mass of the CMZ, producing bubble morphology inconsistent with observations if it is reduced to 10^7 M$_\odot$ or less. This low value of the CMZ mass is, however, unrealistically small, smaller than the current observational constraints of $3-5 \times 10^7$ M$_\odot$ (Dahmen et al., 1998; Pierce-Price et al., 2000). A potentially important caveat is that I model the CMZ as a smooth disc, rather than as a clumpy distribution of gas (Molinari et al., 2011; Morris and Serabyn, 1996). In principle, a real outflow may stream past the clumps and so the collimation effect of the CMZ would be smaller than what I find. However, observations also show that the column density of gas toward the Galactic centre does not vary strongly with viewing direction (Goto et al., 2008), so the CMZ should provide a strong covering

effect to any outflow coming from Sgr A*. In addition, I find that the CMZ aspect ratio has a negligible effect on the bubble properties, i.e. there is a range of CMZ column densities for which the outflow is collimated efficiently. Therefore, I believe that the uncertainty in the results due to the shape of the CMZ is relatively small.

2.7 Conclusions

I have presented the model, analytical calculations and numerical simulations of a wide angle outflow from Sgr A*, temporally coincident with the star formation event ~ 6 Myr ago, and collimated into directions perpendicular to the plane of the Galaxy by the presence of a massive disc of gas, the Central Molecular Zone. The main results are:

- This model is a plausible way to inflate the γ-ray emitting lobes recently observed by the *Fermi*-LAT, provided that Sgr A*'s outburst duration is $\lesssim 1$ Myr.

- The energetics of the model is consistent with the observed γ-ray emission if radiating particles are electrons rather than hadrons.

- Sgr A* feedback could have reshaped the CMZ from a disc-like configuration into a ring-like one reminiscent of the observed structure (Molinari et al., 2011). I speculate that somewhat asymmetric feedback could produce an observed offset of the ring and eccentric orbits for young star clusters such as the Arches star cluster.

- Furthermore, CMZ compression by the feedback outflow may explain the formation of dense GMCs, the young star clusters, the population of isolated massive stars, and also result in the present-day high star formation rate in the Galactic Centre.

An important side result of this investigation is that the same feedback model appears to work for quasars as their SMBHs establish the $M - \sigma$ relation and clear the host galaxies of gas (e.g. King, 2003, 2005; Nayakshin and Power, 2010), as well as for a short burst of activity in Sgr A*, a SMBH that is somewhat below the $M - \sigma$ relation in a quiescent galaxy. This finding suggests that there is nothing fundamentally different between feedback from SMBHs at gas-rich epochs ($z \gtrsim 2$) and that from local galactic nuclei, except for the lower amount of fuel they receive.

More detailed future treatment of the feedback process, with improvements in both the physics of the simulations and more realistic observationally constrained initial conditions, may provide interesting and unique constraints on cosmological models of AGN feedback.

3

Sgr A* flares: tidal disruption of planets and asteroids?[1]

"For a moment it glimmered, faint as a rising
star struggling in heavy earthward mists, and
then as its power waxed, and hope grew in
Frodo's mind, it began to burn, and kindled to
a silver flame, a minute heart of dazzling light,
as though Eärendil had himself come down
from the high sunset paths with the last
Silmaril upon his brow. The darkness receded
from it until it seemed to shine in the centre of
a globe of airy crystal, and the hand that held
it sparkled with white fire."

J. R. R. Tolkien, "The Lord of the Rings",
Book IV, Chapter 9

3.1 Introduction

Most of the nearby SMBHs are rather dim (e.g. Ho, 2008), suggesting that little gas is supplied to them at the current epoch. However, rare and temporary exceptions from this "gas drought" are expected to occur when a star passing too close to a SMBH is shredded into streams by the tidal forces of the SMBH (Rees, 1988). The bound streams precess and self-intersect on the return passage past the black hole, resulting in very strong shocks. The result of these shocks should be a small-scale accretion disc around the SMBH, and thus power a spectacularly bright $L \sim 10^{44} - 10^{46}$ erg s^{-1} flare, lasting a few months (Lodato et al., 2009). Such candidate events have indeed been observed in nearby galaxies (Esquej et al., 2008), and there are some recent observations of γ-ray sources that are best explained by jets resulting from stellar tidal disruption events (Bloom et al., 2011; Campana et al., 2011).

Tidal disruption events are unlikely to be observed from Sgr A* any time soon because they are expected to be quite rare, i.e. $\dot{N}_{\text{tid}} \sim 10^{-5}$ yr^{-1} per galaxy (Alexander, 2005). However, the centre of our Galaxy does produce enigmatic flares on a roughly daily basis. Although miniscule in amplitude ($L_{\text{f}} \sim 10^{34} - 10^{35}$ erg s^{-1}) when compared with stellar disruptions, Sgr A* flares are still $10-100$ times brighter than its quiescent state. The flares are also shorter than stellar dial disruption events, lasting hours rather than months. Here I explore a scenario for the origin of these flares based on a hypothesis that they are the result of tidal disruption of asteroids rather than stars. The fact that there are many more asteroids than stars and that the asteroids are much smaller than stars would naturally explain why Sgr A* flares are much more frequent but much less luminous and shorter than the stellar tidal disruption events.

In this Chapter, I test the asteroid disruption hypothesis for Sgr A* flares. In doing so, I adopt an approach complementary to most of the existing popular models of Sgr A* flares. As reviewed in Section 3.2 below, these usually predict spectra given specific assumptions about emitting particle distributions; it is not always specified how these distributions are energised. In the context of the present model, instead, there is far too much physical uncertainty in predicting the particle distributions at this stage, but I am able to constrain the energetics, the duration and the frequency distribution of the tidal disruption events starting from reasonable assumptions about the populations of asteroids in the central parsec of Sgr A*. The model presents a mechanism for producing the transient hot particle populations responsible for the observed flares.

The Chapter is structured as follows. In Section 3.2 I overview the astrophysical setting of the problem, and the observational characteristics of the flares. In Section 3.3, I estimate the minimum size of the asteroid (~ 10 km) needed to power the observed flares. I then consider what happens to asteroids of different sizes as they pass by Sgr A* on orbits of a given pericentre distance. I show that large asteroids approaching Sgr A* within $R \lesssim 1$

AU are broken into smaller pieces (at most ~ 1 km in size). I also point out that asteroids evaporate as they pass through the gas of the tenuous quasi-spherical accretion flow that is believed to power the quiescent Sgr A* emission (Narayan et al., 1995; Yuan et al., 2003) at very high velocities. The combination of tidal "grinding" of large asteroids into smaller fragments and evaporation of the latter may destroy the asteroids efficiently and turn their bulk energy into heat in the shocks between the evaporated material and the background accretion flow.

In Section 3.4 I calculate the rate at which asteroids are supplied into the vicinity of the SMBH and find values roughly consistent with the frequency of observed flares. In Section 3.5 I note that planets, too, could be tidally disrupted by Sgr A*, although clearly far less frequently than asteroids. I consider whether one such disruption could account for the suspected Sgr A* brightening to $\sim 10^{39}$ erg s^{-1} approximately 100 yr ago, evidenced by the well-known X-ray echo on Sgr B2 molecular cloud (Sunyaev and Churazov, 1998; Revnivtsev et al., 2004) that is now fading (Terrier et al., 2010). Finally, in Section 3.6, I suggest how the evaporating asteroids could produce the high energy particles needed by the current models of flare emission from Sgr A*. I present a summary, discussion and conclusions of the model in Section 3.7.

3.2 Sgr A* and its flares

Sgr A* is the supermassive black hole (SMBH) in the nucleus of our Galaxy, with mass $M_{bh} \simeq 4 \times 10^6$ M$_\odot$ (Schödel et al., 2002; Ghez et al., 2005). By comparison with active galactic nuclei (AGN) Sgr A* is famously dim in all frequencies. Its bolometric luminosity is only $L_{bol} \simeq 100 L_\odot \simeq 10^{-9} L_{Edd}$ (e.g., Melia and Falcke, 2001). In X-rays Sgr A*'s quiescent luminosity is less than $\sim 10^{-11} L_{Edd}$, where $L_{Edd} \sim$ a few $\times 10^{44}$ erg s^{-1} is its Eddington luminosity (Baganoff et al., 2003), and in the near infrared $L \sim 10^{35}$ erg s^{-1} (Genzel et al., 2003a). This extraordinarily low luminosity has been explained in the literature via models of radiatively inefficient inflow and/or outflow (Narayan et al., 1995; Falcke and Markoff, 2000; Narayan, 2002; Yuan et al., 2003, and references therein).

The quiescent emission from Sgr A* is punctuated several times a day by short flares in the near infrared (Genzel et al., 2003a; Ghez et al., 2004; Marrone et al., 2008). Approximately once per day, these flares are accompanied by corresponding rises in the X-ray emission (Baganoff et al., 2001; Eckart et al., 2006a; Hornstein et al., 2007; Marrone et al., 2008; Porquet et al., 2003, 2008). When both NIR and X-ray flares occur, they are almost certainly causally connected and show no appreciable time lag between their peaks, although IR lightcurves have shallower rising and decaying slopes (Hornstein et al., 2007; Yusef-Zadeh et al., 2006a; Eckart et al., 2006b). Sub-mm flares have been observed approximately 1 hour later following some of the IR/X-ray flares (Mauerhan et al., 2005;

Herrnstein et al., 2004; Kunneriath et al., 2010), although the connection between the two has not been firmly established.

Typically, flares last for approximately an hour to a few hours ($t_{\mathrm{f}} \lesssim 10^4$ s) and have luminosities a factor 3–100 above the quiescent emission level in both X-rays and near infrared ($L_{\mathrm{X}} \sim L_{\mathrm{NIR}} \sim 10^{34} - 10^{35}$ erg s^{-1}; Baganoff et al., 2001; Genzel et al., 2003a). There may also be more frequent weaker flares that get blended in the quiescent emission of Sgr A* (Dodds-Eden et al., 2011). The brightest flare observed so far reached $L_{\mathrm{f,max}} \sim 10^{36}$ erg s^{-1} in both the NIR and the X-rays (Porquet et al., 2003, 2008). The observed NIR flare luminosity distribution (Section 3.4.4) seems to follow a $LN_{\mathrm{L}} \propto L^{\alpha}$ law, with $-1 \lesssim \alpha \lesssim 0$ (Dodds-Eden et al., 2011), where $N_{\mathrm{L}}\Delta L$ is defined as the number of flares with maximum luminosity during the flare between L and $L + \Delta L$. The rise and fall times, as well as short timescale variability, suggest that the flaring region is very compact and located within $R \sim 10R_{\mathrm{S}}$ of Sgr A*, where $R_{\mathrm{S}} = 2GM_{\mathrm{BH}}/c^2 \sim 1.2 \times 10^{12}$ cm is the Schwarzschild radius of Sgr A* (Baganoff et al., 2001; Porquet et al., 2003; Shen et al., 2005; Eckart et al., 2006b). Besides the time variability constraints, the location of the emission region is constrained directly by the NIR observations to be within a few milli-arcseconds of Sgr A* (which is equivalent to tens of AU or a few hundred R_{S} Genzel et al., 2003a).

There is currently no universally accepted model for the origin of the Sgr A* flares. Even the emission mechanism is not completely settled. The suggested models are synchrotron emission by either a thermal or a power-law distribution of electrons for the NIR flares plus inverse Compton or self-Compton emission in the X-rays, or power-law synchrotron emission for all the components (e.g., Markoff et al., 2001; Dodds-Eden et al., 2009). In terms of associated physical mechanisms responsible for flares, magnetic reconnection events (Yuan et al., 2003; Dodds-Eden et al., 2010), turbulent shocks (Liu et al., 2004) and jet acceleration (Markoff et al., 2001; Yuan et al., 2002; Maitra et al., 2009) have been proposed. Short-timescale magnetic reconnection event models seem to be more promising than transient density variation models (Markoff et al., 2001; Dodds-Eden et al., 2010).

Another class of flare models envisages a transient feature in the accretion flow around Sgr A*. Such a feature may be an accretion instability (e.g., Tagger and Melia, 2006) or an orbiting hot spot (e.g., Broderick and Loeb, 2005). Finally, a number of authors have proposed an expanding plasma blob as the source of the flares (van der Laan, 1966; Yusef-Zadeh et al., 2006b; Eckart et al., 2006a; Trap et al., 2011; Kusunose and Takahara, 2011). A blob of relativistic plasma, threaded by a magnetic field, is assumed to be suddenly created in the accretion flow around Sgr A*; it then moves outwards while simultaneously expanding at a prescribed velocity. This leads to an evolution of the optical depth of the plasma, which in turn causes different parts of the emission spectrum to appear different

during the flare, leading to time lags between emission maxima and characteristic light curves for the various spectral bands. The orbiting hot spot model is similar to this, except that in the latter, the plasma blob is assumed to circle around Sgr A* for at least several dynamical times.

Nayakshin et al. (2004) suggested that stars orbiting Sgr A* strike an optically thick disc, and that the resulting shocks produce the observed X-ray flares. This model is now firmly disfavoured by the constraints on the NIR flaring region size of $\lesssim 10$ AU, as it would require unphysically large stellar densities in the innermost region. Furthermore, no stellar eclipses or transient brightenings, which would be two observable signatures of the optically thick disc presence near Sgr A* (Nayakshin and Sunyaev, 2003; Cuadra et al., 2003), were found either.

While stars cannot produce enough flares in the small region near Sgr A*, one may legitimately wonder if disruption of asteroids instead of stars could work, as there are far more asteroids than stars. I shall now turn to putting physical constraints on this idea and argue that such a model may serve as a physical basis for the 'expanding transient plasma blob' model (see above). I note that a tidal disruption model has been investigated previously by Čadež et al. (2008) and Kostić et al. (2009). While it is superficially similar to the one presented in this Chapter, these authors only considered the tidal disruption of asteroids, without investigating the interaction of the remnants with the gaseous accretion flow around Sgr A*, which forms a significant part of the present investigation (see Section 3.3 below).

3.3 Asteroid destruction near Sgr A*

3.3.1 The minimum asteroid size

I shall now estimate the minimum size of an asteroid necessary to produce an observable flare. For the low end of observed flare luminosities, the flare luminosity $L_f \sim 10^{34}$ erg s^{-1} in both X-rays and NIR, and the typical duration is $\sim 10^4$ s. The resulting total luminous energy release is $E_f \sim 10^{38}$ erg in each of these bands. This is the minimum energy that the asteroid should produce upon interacting with the background gas flow around Sgr A*. Assuming that the energy is released by an asteroid of mass $M_a = 4\pi/3\rho_a r^3$, where r is the asteroid's mean radius and $\rho_a \sim 1$ g cm^{-3} is its material density (see, e.g., Table 1 in Britt et al., 2002), it seems reasonable to assume that the energy released in the flare is of the order of the bulk energy of the asteroid. Given that tidal disruption occurs inside an AU of Sgr A* or so (see below), the bulk energy is a significant fraction of the asteroid's rest mass energy. Thus, my estimate of energy release is

$$E_f = \xi M_a c^2 = \frac{4\pi\xi}{3}\rho_a r^3 c^2 \sim 4 \times 10^{38}\xi_1 r_1^3 \text{ erg,} \qquad (3.1)$$

where $\xi = 0.1\xi_1$ is the dimensionless fraction of the asteroid's rest mass energy released in the flare and $r_1 \equiv r/(10\text{km})$. It is evident that an asteroid with $r \gtrsim 6$ km releases enough energy to power an observable flare, if the whole energy is released in either IR or X-rays. For the rest of the paper, I use a more conservative value $r \gtrsim 10$ km and parametrise an asteroid's radius as $r \equiv 10\, r_1$ km.

The brightest observed Sgr A* flare requires about a factor of 100 more energy, which, using this rough estimate, would require an asteroid of $r \sim 30$ km, with a more conservative estimate of $r \sim 45$ km. Asteroids of these sizes are "typical" in the Asteroid belt of the Solar System (Bottke et al., 2005) and believed to lurk in the extra solar debris discs as well (Wyatt, 2008).

3.3.2 Tidal disruption of an asteroid

I shall consider large asteroids to have a "rubble-pile" structure, i.e., be a collection of smaller rocks held together by gravity rather than by material strength. This point of view is physically motivated by the fact that large monolithic bodies are expected to collide at high speeds with abundant smaller bodies. Such collisions do not completely obliterate the large bodies but do erode them even in our Solar System (Chapman, 1978; Richardson et al., 1998; Korycansky and Asphaug, 2006). In the environment I am considering, collisions occur at even higher speeds (Section 3.4.3), and therefore the rubble-pile structure is even more relevant.

There are both similarities and differences in the way that asteroids and stars are tidally disrupted near a SMBH. Since the mean density of asteroids, ρ_a, is of the same order as that of main-sequence solar type stars, the tidal disruption radius is very similar for asteroids and stars. An asteroid is tidally disrupted in the vicinity of the SMBH provided that

$$\rho_\text{a} \lesssim \frac{3M_\text{BH}}{4\pi R^3}, \tag{3.2}$$

where R is the distance to the SMBH. For $\rho_\text{a} = 1$ g cm^{-3}, the tidal disruption radius is

$$R_\text{td} \simeq 1.5 \times 10^{13} \text{ cm} \simeq 1 \text{ AU}. \tag{3.3}$$

Unlike a star, a tidally disrupted asteroid breaks up into smaller fragments that are bound by chemical forces rather than gravity. The fragments of the comet Shoemaker-Levy 9 tidally disrupted as it passed by Jupiter are estimated to be around ~ 1 km in size (see the discussion and references in Asphaug and Benz, 1996). Through analytical arguments and numerical simulations, Benz and Asphaug (1999) suggest that objects larger than about ~ 1 km in diameter must be composed of smaller pieces held together by gravity. I shall thus consider the maximum size of the fragments to be around 1 km, and probably less than 100 m due to the more extreme environment I study.

One further difference between stellar tidal disruptions and that of asteroids is in the orbits of the disrupted material. Rees (1988) shows that roughly half of the star's material falls onto orbits bound to the black hole, whereas the other half is ejected into the larger scales (outside ~ 1 pc) of the host galaxy. The semimajor axes of the orbits of disrupted streams of gas can be found from the specific energy of the relevant streams. Before the disruption, the orbit is assumed to be parabolic, thus the specific energy is nearly zero. After the disruption at pericentre distance R, the range of specific energies of the material is $\pm E_{\text{stream}}$, the maximum (or minimum) energy of a disrupted remnant:

$$E_{\text{stream}} \simeq \frac{\partial E}{\partial R} r = -\frac{G\,M_{\text{bh}}\,r}{R_{\text{td}}^2}, \tag{3.4}$$

where R is the distance to the black hole, r is the radius of the disrupted object and I assume that $r \ll R_{\text{td}}$. The energy can be expressed in terms of the orbital velocity of the object, v_{a} (see eq. 3.11) and the escape velocity from the object,

$$v_{\text{esc}}^2 \simeq \frac{GM_{\text{a}}}{r} \sim \frac{G\,M_{\text{bh}}\,r^2}{R_{\text{td}}^3}, \tag{3.5}$$

where I used the tidal disruption condition $M_{\text{bh}} R_{\text{td}}^{-3} \sim M_{\text{a}} r^{-3}$ (ignoring factors of order unity). Putting the two expressions of velocity into equation 3.4, I find that the energy spread is

$$E_{\text{stream}} \simeq v_{\text{a}} v_{\text{esc}}. \tag{3.6}$$

The semimajor axis of the most bound material is thus

$$R_{\text{orb}} \sim \frac{G\,M_{\text{bh}}}{2 v_{\text{a}} v_{\text{esc}}} \sim R \frac{v_{\text{a}}}{v_{\text{esc}}} \ . \tag{3.7}$$

For a Solar-type star, $|v_{\text{esc}}| \sim$ a few $\times 10^7$ cm s^{-1}, and hence the semimajor axis of the most bound orbit is a few hundred times the pericentre passage distance. This implies that the material will fall back to the SMBH vicinity on a timescale of between a month and a year, depending on the SMBH mass. This leads to a bright stellar disruption flare (for recent numerical simulations of the process see Lodato et al., 2009).

However, for an asteroid, $v_{\text{esc}} \sim 5 \times 10^2 \, r_1$ cm s^{-1}, i.e., much smaller than for a star. Therefore, if an asteroid tidal disruption proceeded in exactly the same fashion as that of a star, the change in the orbital energy of the different fragments of the asteroid would be negligible. The disintegrated asteroid would thus continue to travel on an almost identical orbit as the one it had before the disruption. The fragments would come back to the SMBH after hundreds or thousands of years. As luminosity is energy released per unit time, the luminosity output of such a disruption would be far too small to be relevant. Finally, unlike the disrupted stellar gas streams, that are certain to intersect due to precession of

the orbits (Rees, 1988), the returning asteroid fragments are very unlikely to collide with one another. It seems extremely unlikely that any significant flare would be produced in this "dry" disruption scenario.

3.3.3   Asteroid evaporation

The inner few AU of our Galactic centre, or any other galactic centre, are very likely to be filled with a gaseous accretion flow on to the SMBH, however tenuous that flow might be. The asteroid moves through this gas at an almost relativistic velocity. Aerodynamic friction may cause significant heating of the asteroid, perhaps leading to its evaporation before it leaves the central region. I shall term this background-gas-mediated disruption "wet disruption" in contrast to the dry disruption discussed in Section 3.3.2.

The quiescent luminosity of Sgr A* and its linear polarisation measurements suggest an accretion rate $\dot{M} \gtrsim 10^{-8}$ M$_\odot$ yr^{-1} in the system (Aitken et al., 2000; Bower et al., 2003; Marrone et al., 2006). If one assumes that the flow is spherically symmetric, and is in free-fall on to Sgr A*, the gas density can be estimated as

$$\rho_{\mathrm{g}} \simeq \frac{\dot{M}}{4\pi R^2 v_{\mathrm{ff}}} = \frac{\dot{M}}{4\pi \left(GM_{\mathrm{BH}}R^3\right)^{1/2}}$$
$$\sim 3.4 \times 10^{-20} \dot{M}_8\, R_{\mathrm{AU}}^{-3/2}\ \mathrm{g\ cm}^{-3}, \tag{3.8}$$

where $\dot{M}_8 \equiv \dot{M}/10^{-8}$ M$_\odot$ yr^{-1}. This is a lower limit since a geometrically thick disc is a more plausible flow configuration due to a likely nonzero angular momentum. Disc flows are centrifugally supported and hence the radial velocity is always slower than the free-fall velocity assumed above (Shakura and Sunyaev, 1973; Narayan and Yi, 1994). The results of Yuan et al. (2003) suggest a density profile

$$\rho_{\mathrm{g}} \simeq \rho_0 \left(\frac{R}{R_{\mathrm{S}}}\right)^{-s}\ \mathrm{g\ cm}^{-3}, \tag{3.9}$$

with $\rho_0 \simeq 6.4 \times 10^{-17}$ g cm^{-3}, $R_{\mathrm{S}} \simeq 1.2 \times 10^{12}$ cm the Schwarzschild radius and $s \simeq 1.23$. Numerically,

$$\rho_{\mathrm{g}} \simeq 2.9 \times 10^{-18}\, \rho_{18}\, R_{\mathrm{AU}}^{-s}\ \mathrm{g\ cm}^{-3}, \tag{3.10}$$

where ρ_{18} is a factor, of order unity, encompassing the possible deviations from this model. For definiteness, I use equation (3.10) in the calculations below.

An asteroid on a parabolic orbit close to the SMBH moves with velocity

$$v_{\mathrm{a}} \simeq \sqrt{\frac{2GM_{\mathrm{BH}}}{R}} \simeq 9.4 \times 10^9 R_{\mathrm{AU}}^{-1/2}\ \mathrm{cm\ s}^{-1}. \tag{3.11}$$

In the asteroid's rest frame, the mechanical energy flux of the background accretion flow

material striking the asteroid's surface is

$$\Phi_a \sim \rho_g v_a^3 \simeq 2.4 \times 10^{12} \rho_{18} \, R_{\mathrm{AU}}^{-3/2-s} \ \mathrm{erg \ s^{-1} \ cm^{-2}} \ . \tag{3.12}$$

Assuming that a sizeable fraction of this energy flux is re-radiated as thermal blackbody radiation, the effective temperature of the asteroid is

$$T_a \simeq \left(\frac{\Phi_a}{\sigma_{\mathrm{SB}}} \right)^{1/4} \sim 1.4 \times 10^4 \rho_{18}^{1/4} \, R_{\mathrm{AU}}^{-3/8-s/4} \ \mathrm{K}, \tag{3.13}$$

where σ_{SB} is the Stefan-Boltzmann constant. The radiation itself is, however, too faint to be detected (see Section 3.6.2).

Inside the central few AU, the effective temperature of the asteroid is larger than the melting and evaporation temperature of iron ($T_{\mathrm{Fe,m}} \simeq 1800$ K, $T_{\mathrm{Fe,v}} \simeq 3100$ K) and the sublimation temperature of carbon ($T_{\mathrm{C,v}} \sim 3900$ K; carbon does not have a liquid phase at pressures below a few MPa). Therefore, the asteroid's outer layers should indeed be evaporating as it is passing through the inner regions of the accretion flow onto Sgr A*.

The radius at which temperature T_X is reached is, using Stefan-Boltzmann law,

$$R_X \simeq \left(\frac{T_X}{1.4 \times 10^4 \rho_{18}^{1/4}} \right)^{-8/(3+2s)} \ \mathrm{AU}, \tag{3.14}$$

where T_X is one of the sublimation temperatures of interest as above. For the three cases of interest, and $s = 1.23$ I find

$$R_{\mathrm{Fe,m}} \simeq 21 \ \mathrm{AU}, \ R_{\mathrm{Fe,v}} \simeq 10 \ \mathrm{AU}, \ R_{\mathrm{C,v}} \simeq 7 \ \mathrm{AU}. \tag{3.15}$$

This shows that asteroids start melting and evaporating at $R \sim 10$ AU, i.e., well outside the tidal disruption radius. Of the two materials, I expect carbon to be more abundant, so its parameters are used in subsequent calculations.

To calculate the mass loss by the asteroid, I follow the classical meteor ablation considerations (Bronshten 1983, see also Section 2.3.2 in Alibert et al. 2005), which give

$$\dot{M}_v \sim \frac{\pi r^2 \Phi_a C_H}{2 Q_{\mathrm{C,v}}}. \tag{3.16}$$

Here, $\dot{M}_v$ is the mass loss rate due to vaporisation and $Q_{\mathrm{C,v}} \sim 3.0 \times 10^{11}$ erg g^{-1} is the energy per unit mass required to raise the asteroid temperature to the vaporisation temperature and evaporate it (the latter process is energetically dominant). $C_H < 1$ is an unknown dimensionless coefficient which specifies how much of the bulk mechanical energy inflow into the asteroid goes into the mass loss as opposed to thermal re-radiation of that

flux. In the high density environment of Earth and Jupiter atmospheres, C_H can be very small because the optical depth of the evaporating material can be large and hence the asteroids self-shield themselves efficiently (this is called "vapour shielding"). For example, for asteroids of size $1-10$ m in the Earth's atmosphere, $C_H \sim 10^{-3}$ (Svetsov et al., 1995), but this value increases with altitude (i.e. with decreasing atmospheric density).

In the very low ambient gas density environment studied here, C_H is likely to be close to unity because the optical depth of the evaporating material is too small for self-shielding. Two effects are responsible for this. Firstly, the temperature of the evaporating gas may increase to the order of that of the surrounding medium, which is $10^9 - 10^{11}$ K, at which point it would be completely ionised and only electron scattering opacity would be important. Secondly, the column depth of the evaporating flow is not large. To see this, assume that evaporated gas outflows at $v_{ev} \sim 10$ km/s. Since $\dot{M}_v = 4\pi r^2 \rho_v v_{ev}$, the column depth of self-shielding material is

$$\Sigma_v \sim \rho_v r = \frac{\dot{M}_v}{4\pi r v_{ev}} \ . \tag{3.17}$$

Using equation 3.16 I find

$$\Sigma_v \sim \frac{C_H r \Phi_a}{2 Q_{C,v} v_{ev}} \approx 0.3 C_H \frac{r}{1\text{km}} \text{ g cm}^{-2}. \tag{3.18}$$

With opacity coefficient not too different from electron scattering, the evaporated material is obviously optically thin. I hence conclude that thermal ablation of asteroid fragments should be very effective with $C_H \sim 1$ for fragment size $r \lesssim 1$ km.

The evaporation rate is

$$\dot{M}_v \sim 1.3 \times 10^{13} \rho_{18} \ R_{AU}^{-3/2-s} \ r_1^2 \ C_H \text{ g s}^{-1} \ . \tag{3.19}$$

For convenience, I define the vaporisation timescale,

$$t_v = \frac{M_a}{\dot{M}_v} \sim 3.2 \times 10^5 \rho_{18}^{-1} \ R_{AU}^{3/2+s} \ r_1 \ C_H^{-1} \text{ s}. \tag{3.20}$$

It is evident that the smaller the asteroid, the faster it vaporises. The material ablated from the asteroid might assume a cometary shape, with a long gaseous tail behind the solid head (see Section 3.6.2).

3.3.4 Total and partial asteroid disruptions

I shall now delineate the parameter space for the possible outcomes of an asteroid's flyby near a SMBH. An asteroid on a parabolic orbit around Sgr A* with pericentre distance

R_p spends a time

$$t_\mathrm{fly} \simeq \pi t_\mathrm{d} = \pi \sqrt{\frac{R_\mathrm{p}^3}{2GM_\mathrm{BH}}} \simeq 5600 R_\mathrm{AU}^{3/2} \text{ s} \qquad (3.21)$$

at radial distance comparable with R_p. The ratio between the vaporisation timescale and the flyby time is

$$\frac{t_\mathrm{v}}{t_\mathrm{fly}} \sim 57 \rho_{18}^{-1} \ R_\mathrm{AU}^s \ r_1 \ C_H^{-1}. \qquad (3.22)$$

This ratio is important in determining what exactly happens to an asteroid as it swings by the SMBH.

3.3.4.1   Orbits outside 1 AU but inside $\sim$ 10 AU

For asteroids on orbits with pericentre distances larger than $R_\mathrm{td} \sim 1$ AU (equation 3.3), the asteroid is not tidally disrupted. If the orbit passes within $R_\mathrm{X} \sim 10$ AU (eq. 3.14), the surface layers of the asteroid are vaporised at the rate given by equation 3.19. Only a fraction $\sim t_\mathrm{fly}/t_\mathrm{v}$ of the asteroid is ablated during the close passage. Therefore, large asteroids passing Sgr A* further away than 1 AU remain relatively untouched and leave the SMBH vicinity on their initial parabolic orbits.

The luminosity released by material lost by the asteroid in this regime can be estimated as

$$L_\mathrm{f,out} = \xi \dot{M}_\mathrm{v} c^2 = 2 \times 10^{33} \ \xi_1 \ \rho_{18} \ R_\mathrm{AU}^{-3/2-s} \ r_1^2 \ C_\mathrm{H} \text{ erg s}^{-1} \ . \qquad (3.23)$$

For an approach distance of 5 AU, this luminosity becomes observable (i.e. $L_\mathrm{f,out} > 10^{34}$ erg s^{-1}) only if the asteroid radius is $r \gtrsim 190$ km. Such large asteroids are rare. Thus asteroids passing Sgr A* at pericentre distances larger than ~ 1 AU are unlikely to result in observable flares.

3.3.4.2   Total destruction of asteroids inside 1 AU

Inside the tidal disruption radius, the asteroid breaks into fragments with sizes smaller than $r_\mathrm{frag} \sim 1$ km (cf. Section 3.3.2). For these smaller asteroid fragments, vaporisation is much more efficient. The incoming remnants heat up, melt and vaporise rapidly. This leads to a decrease in the material tensile strength, allowing further fragmentation due to tidal shear. As a result, most of the asteroid's mass evaporates during the flyby (cf. equation 3.22). I estimate the luminosity as

$$L_\mathrm{f,in} = \frac{\xi M_\mathrm{a} c^2}{t_\mathrm{fly}} = 6 \times 10^{34} \ \xi_1 \ R_\mathrm{AU}^{-3/2} \ r_1^3 \text{ erg s}^{-1}. \qquad (3.24)$$

At an approach of 1 AU, this luminosity becomes observable for asteroids of radius $r \gtrsim 10$ km.

I can also estimate the maximum flare luminosity. If the asteroid mass is larger than the total mass of the gas in the accretion flow inside 1 AU, then the efficiency of converting the asteroid's bulk motion into radiation must be reduced. Even if the massive asteroid is vaporised completely, the mass of the quiescent accretion flow is simply not high enough to stop the evaporated material bodily. The latter would continue on its outward course from the inner 1 AU. A part of the disrupted material comes back to Sgr A* as in the stellar disruption case but with a time delay much longer than the dynamical time in the inner AU. The proper estimate for the luminosity is then much smaller than equation 3.24 suggests.

This sets an upper limit to the mass of an asteroid that is wholly disrupted and stopped in the inner AU:

$$M_{a,max} \lesssim M_g \left(R < R_{td} \right) \simeq 6.7 \times 10^{22} \, \rho_{18} \text{ g} \tag{3.25}$$

for $s = 1.23$, yielding radius $r \sim 250$ km. The luminosity that an asteroid this massive would produce if it evaporated is

$$L_{f,max} = \frac{\xi M_g \left(R < R_{td} \right) c^2}{t_{fly}} \approx 10^{39} \, \xi_1 \, \rho_{18} \, R_{AU}^{-3/2} \text{ erg s}^{-1}. \tag{3.26}$$

No flares of this magnitude have been detected so far, but this may be quite reasonable as such large asteroids are expected to be rare.

3.3.5 Summary on asteroid disruption

From the arguments outlined above, it is clear that any large asteroids passing Sgr A* within $R \sim 1$ AU could be tidally disrupted and efficiently vaporised. If their material is mixed with the background accretion flow, the bulk kinetic energy of their orbital motion around Sgr A* would be deposited into the accretion flow around the SMBH. If the asteroid's initial radius exceeds ~ 10 km, this energy deposition might be large enough to produce an observable flare.

Asteroids passing at larger R, on the other hand, are not tidally disrupted. Their vaporisation times are longer than the time they spend near the pericentres of their orbits. Therefore, they lose just a small fraction of their mass. The amounts of mass and energy deposited by such more distant flybys in the inner regions near Sgr A* are small, and thus no bright flares from such passages could be produced.

3.4 Flare frequency and luminosity distribution

3.4.1 The "Super-Oort cloud" of asteroids

Nayakshin et al. (2012b) have recently suggested that AGN may be surrounded by several-pc scale clouds of asteroids and planets that have been formed in situ. In this model, star formation episodes take place inside a massive self-gravitating AGN accretion disc (Paczynski, 1978; Kolykhalov and Syunyaev, 1980; Collin and Zahn, 1999; Goodman, 2003; Paumard et al., 2006; Nayakshin et al., 2007) during gas-rich phases when the super-massive black hole grows rapidly. The AGN disc orientation performs a random walk due to chaotic mass deposition events of individual large gas clouds (as argued by King and Pringle, 2006; Nayakshin and King, 2007; Hobbs et al., 2011). As a result, a kinematically and geometrically thick cloud of stars surrounds the SMBH over time. The asteroids form on timescales of a few Myr, much shorter than the lifetimes of all but the most massive stars, and are then stripped from their parent stars by close passages of perturbers, such as other stars or stellar remnants, or by tidal forces of the SMBH. This creates a geometrically thick torus of asteroids and planets which may be called a "Super-Oort cloud" of SMBH by analogy with the Oort cloud of the Solar System.

I emphasise that the above scenario is highly uncertain in terms of the exact mass of the asteroids formed and their distributions around the parent stars. As discussed by Nayakshin et al. (2012b), the origin of solid bodies and even planets themselves around stars in the "normal" Galactic environment is still debated. Nevertheless, Nayakshin et al. (2012b) argued that there exist 3 different scenarios (see their sections 2.1.1 to 2.1.3) where a population of large solid bodies can be born in the central parsec around a SMBH. One important point to note is that while the stellar densities in the central parsec are much higher than in the Solar neighbourhood, implying mean stellar separations of order ~ 1000 AU, the asteroid birth region in all the current theories of planet formation is inside (or even well inside) ~ 100 AU, so tidal forces from either Sgr A* or stellar neighbours should not prevent the formation of solid bodies.

Faced with these significant uncertainties, I shall make the simplest assumption that the population of asteroids born around a host star is initially not too dissimilar from that found in debris discs of nearby stars and the Solar System. Physically, asteroids are remnants of protoplanetary discs and the planet formation process in stellar systems. While the planet formation process is itself not yet understood, one may use observational constraints on the properties of debris discs around nearby stars. Let $n(r)$ be the differential distribution function of asteroids, so that the number of asteroids with radii between r and $r + dr$ is

$$n(r)\, dr = n_0 \left(\frac{r}{r_0} \right)^q dr, \qquad (3.27)$$

where the slope q can be reasonably expected to vary between -3 and -4, but is probably close to the value -3.5 expected if the asteroid population is the high-mass tail of a collisionally evolved debris disc (Wyatt, 2008). I now calibrate n_0 by requiring that the

total mass of asteroids per star is $M_{a,t}$:

$$M_{a.t.} = \int_{r_{min}}^{r_{max}} M_a(r)n(r)dr \simeq \frac{4\pi\rho_a}{3(q+4)} r_{max}^{q+4} \frac{n_0}{r_0^q}, \tag{3.28}$$

where I have assumed that $q > -4$, and therefore the upper limit of the distribution is more important than the lower. I now find the total number of asteroids with radius $r > r_X$ per star:

$$f_a(r > r_X) = \int_{r_X}^{\infty} n(r)dr = \frac{n_0}{r_0^q} \frac{1}{-q-1} r_X^{q+1} =$$
$$= \frac{3M_{a.t.}}{4\pi\rho_a} \frac{q+4}{-q-1} \frac{r_X^{q+1}}{r_{max}^{q+4}}. \tag{3.29}$$

The mass in asteroids (i.e. solid bodies) per star, $M_{a.t.}$, is not easily constrained at present. First of all, the absolute upper limit for this quantity is the total metal (dust) content of a protostellar disc, which is of the order of 10^{-3} M$_\odot$ (assuming Solar metallicity and the disc mass of ~ 0.1 M$_\odot$; see also a compilation of dust mass observations in Figure 3 of Wyatt, 2008, but note that in the GC region, this upper limit may be slightly lower). The minimum mass of the asteroid population, on the other hand, is the mass of dust in debris disc systems. The dust particles in these aged populations are rapidly blown away by the radiation of the parent stars, and must be replenished by a credible source. The collisional cascade that grinds asteroids into the microscopic dust is believed to be such a source. Figure 3 of Wyatt (2008) shows that the dust mass for observed debris discs is of the order $\sim 10^{-8} - 10^{-7}$ M$_\odot$. The minimum mass of the asteroids in these discs should be at least several orders of magnitude higher.

Given this, I take the total mass of the asteroids per star as a free parameter of the model, setting $M_{a.t.} = 10^{-5} m_5$ M$_\odot$, where m_5 is a dimensionless parameter which is hopefully not too different from unity. Setting $r_{max} = 500$ km and $q = -3.5$ for illustrative purposes, I find

$$f_a(r > r_X) = 10^3 m_5 \left(\frac{r_X}{500km}\right)^{q+1} = 2 \times 10^7 m_5 r_1^{q+1}. \tag{3.30}$$

Thus there are approximately 2×10^7 asteroids that form *per star* that may cause observable flares. Assuming the mean stellar mass inside the sphere of influence of Sgr A* is ~ 1 M$_\odot$ (this is reasonable since the population of old stars in the Galactic centre has a standard mass function Bartko et al., 2010) gives $N_* = 4 \times 10^6$ stars and a grand total of $N_a \sim 8 \times 10^{13} m_5$ asteroids large enough to cause observable flares with the default parameter values chosen above.

3.4.2   Event rates

3.4.2.1   A quick estimate

Before proceeding to more detailed calculations, I shall simply assume that the spatial and velocity distribution of asteroids is exactly the same as that of parent stars. As the mean density of a main sequence solar mass star is similar to that of an asteroid, the tidal disruption radius for both is about the same. Given that the expected rate of stellar tidal disruptions in the Galactic Centre is $\dot{N}_* \sim 10^{-5}$ yr^{-1}, the rate for disruption of asteroids is $\dot{N}_*$ times the number of asteroids ($r > 10$ km) per star:

$$\frac{dN}{dt} \sim \dot{N}_* f_{\mathrm{a}} \sim 0.6 \text{ day}^{-1} \left(\frac{\dot{N}_* m_5}{10^{-5} \text{ yr}^{-1}} \right) . \tag{3.31}$$

One can see that the condition $m_5 \gtrsim 1$ must be satisfied to account for the observed flare rates.

   An additional "sanity check" can be done as well. If the currently observed flaring rate is representative of a long-term quasi-static process, then during the lifetime of the Galaxy, $t_{\mathrm{Gal}} \sim 10^{10}$ yr, one might expect $N_{\mathrm{tot}} \sim 3 \times 10^{12}$ flares to have occurred. This number is smaller than the total number of asteroids $r > 10$ km as estimated above, $N_{\mathrm{a}} \sim 10^{14}$, within the sphere of influence of Sgr A*.

3.4.2.2   A filled loss cone estimate

In order to make more detailed estimates of the asteroid disruption rates, I need to calculate the evolution of the angular momentum distribution of the asteroid population. In accordance with my simple model, given that there are f_{a} "interestingly" large asteroids per star, the number density of asteroids inside Sgr A* sphere of influence is

$$n_{\mathrm{ast}} = n_* f_{\mathrm{a}}, \tag{3.32}$$

where n_* is the number density of stars in the same region.

   If the loss cone of the asteroid distribution in angular momentum and energy space is kept full by some process, then the limiting rate of events is given by the estimate of spherical collisionless accretion. Following the derivation in Chapter 14.2 of Shapiro and Teukolsky (1983, equation 14.2.19), the number accretion rate on to a sphere of radius $R_{\mathrm{t}} = 1$ AU is

$$\frac{dN}{dt} = \frac{2\pi G M_{\mathrm{BH}} R_{\mathrm{t}} n_{\mathrm{ast}}}{\sigma}, \tag{3.33}$$

where $\sigma \simeq 10^7$ cm s^{-1} is the velocity dispersion in the Galactic bulge. Using this value of σ gives a minimum accretion rate for the above assumptions; indeed, asteroids with a greater velocity dispersion would escape the sphere of influence and hence do not contribute to the

rate, and asteroids with lower velocity would give a higher accretion rate. Numerically,

$$n_{\text{ast}} \simeq \frac{3N_*}{4\pi R_{\text{h}}^3} f_{\text{a}} \simeq 7.6 \times 10^{-44} \; m_5 \; r_1^{q+1} \; \text{cm}^{-3}, \tag{3.34}$$

where $R_{\text{h}} \simeq 2$ pc is the radius of influence of Sgr A*. The number accretion rate of asteroids on to Sgr A* is then

$$\begin{aligned} \frac{dN(r > r_{\text{x}})}{dt} &\sim 3.8 \times 10^{-4} \; R_{\text{AU}} \; m_5 \; r_1^{q+1} \; \text{s}^{-1} \\ &= 33 \; R_{\text{AU}} \; m_5 \; r_1^{q+1} \; \text{day}^{-1}. \end{aligned} \tag{3.35}$$

This is a large rate which is certainly an overestimate since it assumes a filled loss cone and no losses from the original asteroid population. I now address these two points.

3.4.2.3   A depleted loss cone rate

If the loss cone is almost empty, then the accretion rate is set by its refilling timescale. The classical loss cone refilling arguments, e.g., Alexander (2005, eq. 6.11) and references therein, give

$$\frac{dN}{dt} \sim \frac{2f_{\text{a}}N_*}{\ln{(R_{\text{h}}/R_{\text{t}})} \, t_{\text{r}}(R_{\text{h}})} \simeq 5 \times 10^{-12} f_{\text{a}} \; \text{s}^{-1}, \tag{3.36}$$

where $t_{\text{r}}(R_{\text{h}}) \simeq 4 \times 10^9$ yr is the relaxation time at R_{h}. Substituting for f_{a} from eq. (3.30) gives

$$\begin{aligned} \frac{dN(r > r_{\text{x}})}{dt} &\simeq 9.5 \times 10^{-5} m_5 \; r_1^{q+1} \; \text{s}^{-1} \\ &\simeq 8 \; m_5 \; r_1^{q+1} \; \text{day}^{-1}. \end{aligned} \tag{3.37}$$

This is somewhat smaller than the estimate in equation 3.35.

3.4.3   Secular evolution of asteroid population

In the above treatment, I only considered gravitational perturbations of asteroid orbits by stars that lead to eventual accretion by Sgr A*. In reality, two other processes are potentially important. First of all, while the asteroids themselves are too small to perturb each other's orbits gravitationally in the central parsec of the Galaxy, they may collide bodily with each other. Some of these collisions may be catastrophic (i.e., they break the asteroid into two or more pieces). Since I am interested in large bodies for which fragmentation conditions depend on self-gravity rather than tensile strength (Wyatt, 2008), the size of an impactor that can just shatter an asteroid of radius r is derived from

$$\frac{M_{\text{a}}(r_{\text{i}}) \, v_{\text{i}}^2}{2} = \frac{GM_{\text{a}}^2(r)}{r}, \tag{3.38}$$

where the subscript "i" stands for "impactor". Expressing mass in terms of asteroid radius gives an expression

$$r_i \sim 1.9 \times 10^3 \; r_1^{5/3} \; v_{100}^{-2/3} \; \text{cm}, \tag{3.39}$$

where the impactor velocity is parametrised in units of 100 km/s. Now I consider a large asteroid moving with velocity v_i through a stationary cloud of other asteroids. By definition, it sees on average 1 impactor large enough to shatter it in a cylinder of area πr^2 and length $v_i t_{\text{coll}}$, where t_{coll} is the collision timescale. Since the number density of impactors can be expressed using eq. (3.32), I find

$$\begin{aligned} t_{\text{coll}} &= \left[f_a(> r_i) n_* \pi r^2 v_i \right]^{-1} = \\ &= 2.1 \times 10^9 \; m_5^{-1} \; r_1^{13/6} \; v_{100}^{-8/3} \; \text{yr}. \end{aligned} \tag{3.40}$$

This timescale is longer than the Hubble time for $r > 24$ km. Therefore it is clear that while some of the smaller asteroids may be destroyed, the largest ones, which also contain the majority of the total mass, are not. Furthermore, the estimate assumes a steady-state collisional fragmentation cascade of the form (3.27), which may actually turn over at small r if the smaller bodies are removed from the cascade rapidly.

A second potentially important process is mass segregation, which causes heavier objects to sink in closer to the centre of the potential well while lighter ones move out and may be expelled from a galactic nucleus (Bahcall and Wolf, 1976; Alexander, 2005). For the problem at hand, the process is driven by dynamical friction (Chandrasekhar, 1943) between stars (the dominant heavy objects in the nuclear star cluster) and asteroids. As the latter gain energy, one expects a reduction in the population of asteroids over time. This should reduce the flare frequency.

The relevant question here is that of the timescales on which the asteroids are expelled by mass segregation. An order of magnitude estimate utilising the Chandrasekhar formula and stellar densities consistent with the observed stellar mass distribution in the central pc (e.g., Paumard et al., 2006) shows that asteroids at $R \sim 1$ pc gain enough energy in about $\sim 10^9$ years. A better estimate is possible based on calculations of dynamical mass segregation in the Sgr A* cluster (e.g., Freitag et al., 2006). To rescale these calculations to the case of interest, I note that the timescale to expel a light population of average particle mass M_1 by particles of mass $M_2 \gg M_1$ scales as $\propto (M_2 M_{2,\text{tot}})^{-1}$, where $M_{2,\text{tot}}$ is the total mass of the population of particles M_2 (cf. eq. 8 in Freitag et al., 2006). Now, I note that main-sequence stars only begin to be expelled outward by the cusp of stellar mass black holes at $t = 3.5 \times 10^9$ years as seen best in the middle panel of Fig. 11 of Freitag et al. (2006). Since the latter are a factor of ~ 20 times more massive than main sequence stars but are less frequent, the product $M_2 M_{2,\text{tot}}$ is actually almost the same for the main sequence star cluster as for the stellar mass black hole cluster. Therefore I

estimate that the dynamical mass segregation time scale for asteroids is not much shorter than $\sim 3 \times 10^9$ years.

This is somewhat shorter than the presumed age of the stellar cluster of $\sim 10^{10}$ years. In principle, therefore, mass segregation may reduce the flare frequency estimate by a factor of a few. However, there are also source terms in the "freely floating" asteroid population of the central parsec that I have not considered here. For example, the asteroids are released from the parent stars over time rather than only at birth of the stars. Also, as the latest star formation episode ~ 6 million years ago shows (Paumard et al., 2006), star formation in the central parsec may be continuing to the present day. Finally, in this Chapter I did not take into account asteroids that can be "shaved off" – removed by tidal forces of Sgr A* – from main sequence stars that pass through the inner region for the first time from the further regions of the Galaxy. Depending on the orbit of the star with respect to Sgr A* and the precise orbit of the asteroid around the parent star, there may be several outcomes of its removal from the parent's gravitational potential well. In analogy to disrupted stellar binaries and hypervelocity stars (Brown et al., 2005), it is clear that some of these asteroids become "hypervelocity asteroids" perhaps even escaping the Galaxy, whereas others are bound to the central parsec (e.g., Hills, 1988).

Therefore, while dynamical friction is important in removing asteroids from the central parsec on long time scales, I feel that its importance is rather limited compared to other uncertainties of the problem encapsulated in the parameter m_5 and the asteroid size distribution.

3.4.4   Flare luminosity distribution

The asteroid number density (eq. 3.30) may be used to calculate the number of asteroids per star that have mass greater than M_X:

$$f_a \left(M_a > M_X \right) = 6 \times 10^9 \, m_5 \left(\frac{M_X}{4 \times 10^{15} \text{g}} \right)^{(q+1)/3}. \tag{3.41}$$

The observed distribution of flare luminosities follows a $L N_L \propto L^\alpha$ law, with $-1 \lesssim \alpha \lesssim 0$ (Dodds-Eden et al., 2011, see also Section 3.2). Using this, the frequency of flares with luminosity $L_f > L_X$ is

$$N(L_f > L_X) = \int_{L_X}^{\infty} N_L dL \propto L N_L \propto L^\alpha. \tag{3.42}$$

Since the luminosity of a flare from an asteroid of mass M_X is proportional to M_X in the present model, I can convert the asteroid mass distribution into flare luminosity distribution:

$$N(L_f > L_X) \propto L_X^{(q+1)/3}, \tag{3.43}$$

where the value of the exponent varies between $-2/3$ (for $q = -3$) and -1 (for $q = -4$). This is within the observationally constrained range of α (Dodds-Eden et al., 2010).

Flares with luminosity $L_{\rm f,X} = 10^{34}\ L_{34}$ erg s^{-1} correspond to

$$r \sim 10\ \xi_1^{-1/3}\ R_{\rm AU}^{1/2}\ L_{34}^{1/3} {\rm km}. \tag{3.44}$$

Using eq. (3.37), I normalise the flare luminosity distribution, and obtain, for $q = -3.5$ as the likely value,

$$\dot{N} \sim 8\ m_5\ L_{34}^{-5/6} {\rm day}^{-1}. \tag{3.45}$$

The brightest flare seen so far has $L_{\rm X,max} \sim 10^{36}$ erg s^{-1}, requiring $r \gtrsim 45$ km, which corresponds to $\dot{N} \sim 0.2$ day^{-1}. The total duration of *Chandra* observations of Sgr A* is $t_{\rm obs} \sim 1.4$ Msec, so one would expect it to have seen $N \lesssim 3.5$ flares of this magnitude or brighter, which is not too far off from the one flare actually observed (the Poisson probability of observing 1 flare in a distribution with mean of 3.5 is $\sim 10\%$).

3.5 Planet disruptions

Although much less frequent, planet disruptions may also occur near Sgr A*. Their frequency is probably comparable to that of stellar disruptions, i.e., one per $\sim 10^5$ yr (Alexander, 2005), if one assumes one planet per star on average. Consider now a gas giant planet passing within 1 AU of Sgr A*. Its disruption is quite analogous to that of a star. The most bound disrupted material is on an orbit with a semimajor axis (cf. eq. 3.7)

$$a_{\rm p} \sim R \frac{v_{\rm a}}{v_{\rm esc,p}} \sim 2 \times 10^3 \ {\rm AU} \sim 0.01 \ {\rm pc}, \tag{3.46}$$

where $v_{\rm esc,p}$ is the escape velocity from the planet's surface (~ 60 km/s for a Jupiter mass body). The bound debris returns back to the vicinity of Sgr A* after a time

$$P_{\rm orb} \sim 2\pi \sqrt{\frac{a_{\rm p}^3}{GM_{\rm BH}}} \sim 30 \ {\rm yr}. \tag{3.47}$$

The maximum fallback rate is thus $\dot{M}_{\rm back} \sim 10^{-3}\ {\rm M}_\odot/(30{\rm yr}) = 3 \times 10^{-5}\ {\rm M}_\odot\ {\rm yr}^{-1}$. This rate is significantly larger than the estimated current quiescent accretion rate onto Sgr A*, $\dot{M} \sim 10^{-8}\ {\rm M}_\odot\ {\rm yr}^{-1}$ (Aitken et al., 2000; Bower et al., 2003; Marrone et al., 2006). Conceivably one could expect Sgr A* to brighten by multiple orders of magnitude for approximately tens to a hundred years. The maximum bolometric luminosity is obtained assuming the radiatively efficient conversion of accretion energy into radiation:

$$L_{\rm back} \lesssim 0.1 \dot{M}_{\rm back} c^2 \sim 2 \times 10^{41} \ {\rm erg s}^{-1} . \tag{3.48}$$

The order of magnitude of this luminosity and the flare duration (tens of years) are consistent with the brightening inferred to have occurred some ~ 100 yr ago, when Sgr A* was apparently as bright as $\gtrsim 10^{39}$ erg s^{-1} in X-rays (Revnivtsev et al., 2004; Terrier et al., 2010). I therefore propose a hypothesis that tidal disruption of a rogue gas giant planet could account for that activity episode.

3.6 Emission mechanisms

A detailed modelling of the emission from the vaporised material mixed with the background flow is beyond the scope of this Chapter due to many physical uncertainties (such as the role of magnetic fields along the interface between the vaporised tail and the ambient gas). However, it is possible to rule out several potential emission mechanisms and point out the most promising scenario under which tidal disruption of asteroids could produce spectra consistent with those observed.

3.6.1 Asteroid disruptions are not "accretion rate" flares

The simplest view of emission from asteroids is that they bring in an additional mass to the inner accretion flow on to Sgr A*. The transient enhancement in the accretion rate on to Sgr A* could then make it temporarily brighter. However, in Section 3.3.4.2, I pointed out that the mass of the background quiescent accretion flow onto Sgr A* inside 1 AU is $\sim 10^{23}$ g based on the model of Yuan et al. (2003). This is ~ 3 orders of magnitude more massive than the typical asteroid mass that I considered here. The mass added by an asteroid to the region within 1 AU is simply too small to make an accretion powered flare unless the asteroid's diameter is about 500 km, which must be a very rare event, and would in any case evolve very differently from the small asteroids considered in this treatment (see eq. 3.25 and Section 3.3.4.2). Therefore, if asteroid tidal disruptions are to be observable, they are to be accompanied by production of particles emitting differently (more efficiently) than the background radiatively inefficient accretion flow.

This is consistent with observational constraints on the flares. Markoff et al. (2001) have shown that constraints on the absence of significant variability in the radio emission of Sgr A* suggest that during the flares it is not the magnetic field but rather the energy distribution of emitting particles that vary. This conclusion rules out accretion-powered flares as the mean magnetic field is expected to be proportional to the flow pressure and thus density. Similarly, Yuan et al. (2004) found that infrared flares from Sgr A* are best explained by assuming that a small fraction of electrons in the flow (e.g., a few percent) is accelerated into a non-thermal power-law tail.

3.6.2   Thermal radiation from the asteroid's tail

One new population of particles, compared with the very hot $T \sim 10^{11}$ K quiescent accretion flow, is in the vaporising asteroid's ejecta while it is still relatively cold, i.e., $T \sim T_{\mathrm{X}} \sim 10^4$ K (cf. Section 3.3.3). The ejecta has initially a much higher density than the ambient medium and must expand into the latter as it heats up. The evaporating coma is probably shaped as a conical tail behind the asteroid. Since the surface area of the tail is much larger than the asteroid itself, the tail should be much brighter than the asteroid's face, and perhaps observable from Earth. Its emission can be approximated as thermal, since the thermalisation timescale of electrons in the coma is less than 1 s (e.g., Stepney, 1983). The bolometric luminosity of the emission emanating from the tail is

$$L_{\mathrm{bb}} \simeq A\ \sigma_{\mathrm{SB}}\ T_{\mathrm{tail}}^4\ \frac{\tau}{\tau + 1}, \qquad (3.49)$$

where τ is the optical depth in the direction perpendicular to the tail and A is the surface area of the tail. The optical depth, τ, is

$$\tau \sim \kappa\ \rho_{\mathrm{tail}}\ r_{\mathrm{tail}}, \qquad (3.50)$$

with $\kappa \equiv 10\kappa_1$ the opacity of the material. Assuming $A \sim \pi r_{\mathrm{tail}} h_{\mathrm{tail}}$, where r_{tail} and $h_{\mathrm{tail}} \gg r_{\mathrm{tail}}$ are the base radius and height of the cone, I note that

$$A\tau = \kappa\ \rho_{\mathrm{tail}}\ \pi r_{\mathrm{tail}}^2 h_{\mathrm{tail}} \sim \kappa\ M_{\mathrm{tail}}, \qquad (3.51)$$

where $M_{\mathrm{tail}} \lesssim M_{\mathrm{a}}$ is the mass of the tail. The maximum thermal luminosity from the evaporating ejecta is achieved if the tail is moderately optically thin, $\tau \lesssim 1$, and is

$$L_{\mathrm{bb,max}} \simeq \kappa\ M_{\mathrm{a}}\ \sigma_{\mathrm{SB}}\ T_{\mathrm{tail}}^4 \simeq 2 \times 10^{31}\ \kappa_1\ r_1^3\ \left(\frac{T_{\mathrm{tail}}}{10^4\ \mathrm{K}} \right)^4\ \mathrm{erg\ s}^{-1}. \qquad (3.52)$$

This value is significantly smaller than the quiescent NIR luminosity of Sgr A*. Further, the blackbody spectrum for $T_{\mathrm{tail}} \sim 10^4$ K peaks in the UV, where extinction is very large. In the NIR frequencies, where Sgr A* line-of-sight is less obscured, the tail emits in the Rayleigh–Jeans regime and hence is far dimmer than the bolometric luminosity estimate above. Summing this up, I conclude that direct thermal radiation from the evaporating material is not observable against the background of quiescent Sgr A* emission.

On the other hand, the opacity of the expanding tail may be sufficiently large to account for absorption of the quiescent emission, producing the occasionally observed dimming of Sgr A* in radio and sub-mm wavelengths just before a flare (Yusef-Zadeh et al., 2010).

3.6.3   A new relativistic population of particles?

The particles in the asteroid's tail have a very different velocity distribution compared with that of the background flow. The initial velocities of the ions in the tail are strongly dominated by the bulk motion inherited from the initial asteroid's orbit around Sgr A*. This velocity is somewhat larger than the ion sound speed of the accretion flow (for a hot quasi-spherical inflow the sound speed is of the order of the local Keplerian speed).

When the vaporised tail particles get mixed with the accretion flow particles, a very anisotropic velocity distribution develops. Therefore I expect a number of plasma instabilities to operate while the ions and the electrons of the vaporised material are assimilated into the hot Sgr A* accretion flow. If non-thermal electrons reach equipartition with the shocked ions as in the models of gamma-ray bursts (e.g., Meszaros et al., 1994), their maximum γ-factors could be as large as $(G\,\mathrm{M_{bh}}/c^2 R)\,(m_\mathrm{i}/m_\mathrm{e}) \sim 0.1 m_\mathrm{i}/m_\mathrm{e}$, where m_i and m_e are the ion and electron mass respectively. Even for $m_\mathrm{i} = m_\mathrm{p}$, inside the inner AU this factor exceeds 100.

It is thus likely that a disrupted asteroid produces a transient population of high energy electrons along its original trail. This population should cool by radiative emission and mixing with the background. Without going into a model-dependent characterisation of these processes, I only note that a tidal disruption event may plausibly give rise to the hot particle distributions needed in the scenarios of transient plasma blob based flare emission (e.g. Trap et al., 2011, and Section 3.2). I think that this scenario of converting asteroid's bulk energy into radiation is by far the most promising one to produce spectra resembling Sgr A* flares.

3.7   Discussion and conclusions

In this Chapter I considered the fate of asteroids passing Sgr A* within a few AU on nearly radial orbits. As noted in the Introduction section, I am unable to make detailed spectral predictions at this time, but I do obtain interesting constraints on the energetics, bolometric luminosity and frequency of flares powered by tidal disruption of asteroids. I give a short summary of the main results and model predictions here.

The physical picture of asteroid disruption near Sgr A* has two stages. Firstly, the asteroid is tidally disrupted if it enters the inner ~ 1 AU region, where it is broken into smaller fragments bound by molecular forces rather than gravity. These fragments are probably less than a few hundred meters in radius. The second stage of the disruption is evaporation of these smaller fragments by heat released due to aerodynamic friction of the fragments on the quiescent accretion flow near Sgr A*. The bulk kinetic energy of the asteroid is sufficient to power an observable flare if the asteroid's radius is greater than about 10 km. I then estimated the asteroid disruption event rate based on the assumption

that the number of asteroids per star is reasonably large and is of the order of that inferred from nearby stars.

The model presented here makes the following predictions:

1. The small size of the flaring region, $R_\mathrm{f} \lesssim 10 R_\mathrm{S} \sim 1$ AU. This is the tidal disruption radius for a typical asteroid. Bodies passing Sgr A* outside this radius lose some mass by vaporisation of the outer layers, but the amount of such a mass loss is too small to give a detectable flare (cf. Section 3.3.5).

2. Frequency of flare occurrence is given by the rate at which asteroids from the "Super-Oort" cloud in the inner parsec (Nayakshin et al., 2012b) are deflected onto low angular momentum orbits that bring them within the tidal disruption radius. For fiducial numbers, the model yields a reasonable agreement with the observations (Section 3.4.2). This estimate, however, sensitively depends on the poorly constrained normalisation factor m_5 (equation 3.37).

3. The model naturally predicts a wide range of flare luminosities due to a range in asteroid sizes. Under the assumption that flare luminosity is proportional to the mass of the asteroid disrupted, I also find that the luminosity-frequency relation for flares is within observational constraints (Section 3.4.4).

4. Extending the model to tidal disruption of gas giant planets predicts rare but much brighter flares. One such event may have produced the AGN-like flare of Sgr A* ~ 100 years ago (Section 3.5).

5. The flare frequency in this model is given by the supply of asteroids rather than by the properties of the hot quiescent flow. Therefore, I would expect no strong correlation between the quiescent properties of Sgr A* spectrum and the occurrence of flares (that is, if Sgr A* quiescent emission were to brighten or dim by a factor of a few in the next few years, I would not expect the rate of flaring at a given flare luminosity to be affected). A weak correlation may be expected if the flare luminosity depends more on the asteroid evaporation rate than on the dynamical timescale.

6. I also note that asteroid disruption flares from exceptionally large asteroids may be observable from nearby galactic nuclei. Equation 3.45 predicts that a flare with $L \sim 10^{39}$ erg s^{-1} would occur once every few years at best. However, for a large enough sample of sources such events may be detected in dormant nearby galactic nuclei.

7. The fact that the flare trigger has an external origin provides a way to test this model. Markoff (2005) showed that in the flaring state, Sgr A* sits on the Fundamental Plane of radio and X-ray luminosities for black holes (both stellar mass and supermassive) The uncertainty in the slope and the scatter in the relation make most observed Sgr A* flares consistent with the Fundamental Plane, with the brightest flares being at the high-luminosity end of the allowed scatter. The Fundamental Plane is thought to arise due to accretion physics (Merloni et al., 2003), so if the flares are caused by accretion insta-

bilities of any kind (i.e. internal triggers), flares more luminous than $L_X \simeq 10^{36}$ erg s^{-1} should be accompanied by a corresponding increase in radio luminosity, with a possible lag of months to years. On the other hand, asteroid-induced flares should not exhibit this correlation, at least not up to luminosities $L_{f,max} \simeq 10^{39}$ erg s^{-1} (eq. 3.26), when the asteroid mass becomes comparable to the gas mass in the quiescent flow. Future long-duration observational campaigns of Sgr A* may thus help distinguish between differing flare scenarios.

The least constrained parts of the model have to do with the exact distribution of asteroids and their orbits in the hypothesised "Super-Oort cloud" around Sgr A*, and with conversion of the bulk kinetic energy of the asteroids into electromagnetic radiation. However, there almost certainly are asteroids in the central few pc of the Galaxy and the processes described here must occur. In this Chapter, I make several estimates of the effects that asteroids have on the luminosity of Sgr A* and suggest a method to distinguish between such externally caused flares and accretion-instability caused ones. If future observations reveal that asteroid disruptions are responsible for at least a fraction of the flares, this would be an important step in understanding the accretion processes in Sgr A*. In addition, further investigation may help constrain the size of the asteroid population in the Galactic centre.

4

Clearing out a galaxy with large-scale energy-driven outflows[1]

> "And thou, Melkor, shalt see that no theme may be played that hath not its uttermost source in me, nor can any alter the music in my despite. For he that attempteth this shall prove but mine instrument in the devising of things more wonderful, which he himself hath not imagined."
>
> *J. R. R. Tolkien, "Ainulindalë"*

---

[1]The contents of this Chapter have been published as Zubovas & King, 2012, ApJL, 745, 34

4.1   Introduction

4.1.1   AGN wind feedback

As already discussed in the Introduction (Section 1.3) and Chapter 2, supermassive black hole (SMBH) activity leads to the development of a fast wind which inflates an outflow of gas in the host galaxy. Depending on the mass of the SMBH and its luminosity, the outflow may either fragment and collapse on small scales, or be expelled to large distances. This latter situation is the focus of this Chapter.

Large-scale outflows can significantly affect the appearance and structure of the host galaxies. A dramatic reduction of gas available for star formation and SMBH feeding may establish the black hole – bulge mass relations (Power et al., 2011b, also see Introduction, Section 1.2) and move the galaxy from the blue cloud to the red sequence (Bell et al., 2004). While the outflow proceeds, it should produce observable signatures. Such outflows have been recently observed (see Section 4.1.2 below) and provide a good test for the AGN wind feedback model.

4.1.2   Observations

Recently, three groups (Feruglio et al., 2010; Rupke and Veilleux, 2011; Sturm et al., 2011) have used molecular spectral line observations to reveal fast ($v_{\mathrm{out}} \sim 1000$ km s^{-1}) kpc-scale, massive ($\dot{M}_{\mathrm{out}} \sim 1000$ M$_\odot$ yr^{-1}) outflows in the nearby quasar Mrk231. Other galaxies show indications of similar phenomena (e.g. Riffel and Storchi-Bergmann, 2011a,b; Sturm et al., 2011, see also Table 4.1). These appear to show how quasar feedback can transform young, star-forming galaxies into red and dead spheroids (Schawinski et al., 2007). All three groups reach this conclusion for Mrk231 essentially by noting that the mass outflow rate $\dot{M}_{\mathrm{out}}$ and the kinetic energy rate $\dot{E}_{\mathrm{out}} = \dot{M}_{\mathrm{out}} v_{\mathrm{out}}^2 / 2$ of the outflow are too large to be driven by star formation, but comparable with those predicted in numerical simulations of AGN feedback. The kinetic energy rate is a few percent of the likely Eddington luminosity (eq. 1.5) of the central black hole. The outflowing material must have a multi-phase structure, because v_{out} greatly exceeds the velocity corresponding to the molecular dissociation temperature ($v_{\mathrm{diss}} \lesssim 10$ km s^{-1}; see Section 4.6 below).

4.1.3   Previous work

In a recent paper (King et al., 2011) my collaborators and I showed that large-scale fast outflows (technically, energy-driven flows, see Section 4.3) can drive much of the interstellar gas out of a galaxy bulge on a dynamical timescale $\sim 10^8$ yr, leaving it red and dead, provided that the central supermassive black hole accretes for about twice the Salpeter time after reaching the value set by the $M - \sigma$ relation. However we did not

investigate the observable features of this process, including in particular the way that the interstellar gas is swept up.

4.1.4   This Chapter

I return to this problem here, as it offers a clear observational test of the idea that AGN outflows are responsible for making galaxies red and dead. To keep the treatment as general as possible (specifically, independent of the details of numerical simulations) I adopt a simple analytic approach (described in some detail in the Introduction, Section 1.3). I find that this process predicts outflow velocities $\sim 1000 - 1500$ km s^{-1}, and mass outflow rates up to ~ 4000 M$_\odot$ yr^{-1}, several hundred times the Eddington accretion rate, in good agreement with observations (see below). In addition, I find that the observable momentum outflow rate is ~ 20 times greater than L/c of the driving AGN, also in agreement with observations. I conclude that AGN outflows are good candidates for the agency sweeping galaxies clear of gas.

This Chapter is structured as follows. In Section 4.2 I review the evidence and properties of AGN winds. A discussion of shocks with the ambient medium follows in Section 4.3 and basic outflow properties are presented in Section 4.4. Finally, I derive the observable properties of large-scale outflows in Section 4.5. I finish with a summary and discussion in Section 4.6.

4.2   Winds

To drive outflows with $\dot{E}_{\rm out}$ approaching $L_{\rm Edd}$ at large radius, the active nucleus of a galaxy must somehow communicate this luminosity from its immediate vicinity. Direct transport by radiation is problematic, not least because galaxies are generally optically thin (However, dust opacity may be large enough to absorb this radiation and provide feedback; see Murray et al., 2005). Jets are sometimes invoked, but are relatively inefficient because they tend to drill holes in the interstellar medium rather than driving it bodily away. Accordingly the most likely connection is via high-velocity wide-angle winds expelled from the vicinity of the nucleus by radiation pressure (e.g. Pounds et al., 2003a,b). Recent observations suggest that such winds are very common in AGN (Tombesi et al., 2010a,b). In this Chapter, I use the term "wind" to refer to the mildly relativistic ($v \sim 0.1c$) ejection of accretion disc gas from the immediate vicinity of the SMBH resulting from Eddington accretion, and "outflow" (see Section 4.4) for the large-scale nonrelativistic flows caused by the interaction between the wind and the galaxy's ambient gas.

The winds have simple properties. With mass flow rate $\dot{M}_{\rm w} \sim \dot{M}_{\rm Edd}$, where $\dot{M}_{\rm Edd} = L_{\rm Edd}/\eta c^2$ is the Eddington accretion rate and η is the accretion efficiency, a wide-angle wind has scattering optical depth ~ 1 (King and Pounds, 2003, also Section 1.3.4), as-

shock front
(momentum and
pressure conserved)

wind shock
(thermalized energy rapidly
lost to cooling,
only ram pressure
conserved)

fast wind
($\dot{E}_w = \eta L_{Edd}/2$)

ISM

cooling ISM

cold shocked ISM
($\dot{E} \approx \sigma L_{Edd}/c \ll \dot{E}_w$)

cold shocked wind
($\dot{E} \approx \sigma L_{Edd}/c \ll \dot{E}_w$)

cooling wind

fast wind

ISM shock
(thermalized energy
rapidly lost to cooling,
only ram pressure
conserved)

momentum-driven outflow

SMBH

contact discontinuity
(momentum and
pressure conserved)

energy-driven outflow

fast wind
($\dot{E}_w = \eta L_{Edd}/2$)

shocked,
adiabatically expanding
wind
($\dot{E}_w = \eta L_{Edd}/6$)

shocked,
adiabatically
expanding
ISM
($\dot{E} = \eta L_{Edd}/3$)

ISM

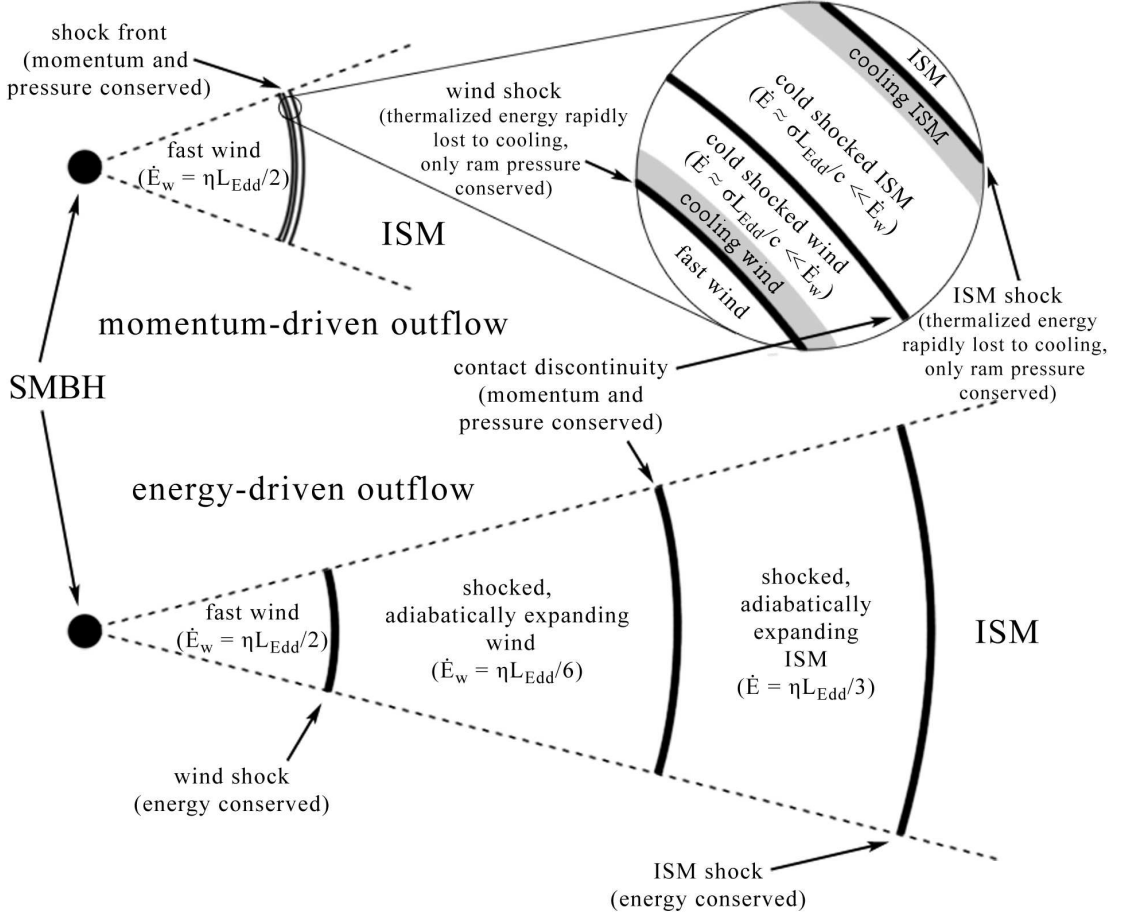wind shock
(energy conserved)

ISM shock
(energy conserved)

Figure 4.1: Diagram of momentum-driven (top) and energy-driven (bottom) outflows. In both cases a fast wind (velocity $\sim 0.1c$) impacts the interstellar gas of the host galaxy, producing an inner reverse shock slowing the wind, and an outer forward shock accelerating the swept-up gas. In the momentum-driven case, the shocks are very narrow and rapidly cool to become effectively isothermal. Only the ram pressure is communicated to the outflow, leading to very low kinetic energy $\sim (\sigma/c)L_{Edd}$. In an energy-driven outflow, the shocked regions are much wider and do not cool. They expand adiabatically, communicating most of the kinetic energy of the wind to the outflow (during the AGN phase, approximately 1/3rd is retained by the shocked wind). The outflow radial momentum flux is therefore greater than that of the wind. Momentum-driven flows occur when shocks happen within ~ 1 kpc of the AGN, and establish the $M - \sigma$ relation (King, 2003, 2005). Once the supermassive black hole mass attains the critical $M - \sigma$ value, the shocks move further from the AGN and the outflow becomes energy-driven. This produces the observed large-scale flows, which probably sweep the galaxy clear of gas.

suming that the covering factor of absorbing gas is close to unity (see the discussion below equation 4.2). So each driving photon on average scatters about once before escaping to infinity and gives up all of its momentum to the wind, so that the wind mass flow rate $\dot{M}_\mathrm{w}$ and velocity v obey

$$\dot{M}_\mathrm{w}v \sim \frac{lL_\mathrm{Edd}}{c}, \tag{4.1}$$

with $l \simeq 1$ the Eddington ratio. Defining $\dot{m} = \dot{M}_\mathrm{w}/\dot{M}_\mathrm{Edd} \sim 1$ as the mass flow factor of the wind, I immediately find

$$\frac{v}{c} \sim \frac{l\eta}{\dot{m}} \sim 0.1 \tag{4.2}$$

(cf King, 2010b). The likely ionisation equilibrium of the wind is such that it produces X-rays (King, 2010b). In line with these expectations, blueshifted X-ray iron absorption lines corresponding to velocities $\sim 0.1c$ are seen in a significant fraction of local AGN (e.g. Pounds et al., 2003a,b; Tombesi et al., 2010a,b), justifying the assumption of a covering factor close to unity. In all cases the inferred wind mass flow rates agree with equation (4.1). So these black hole winds have momentum and energy rates

$$\dot{P}_\mathrm{w} \sim \dot{m}\frac{lL_\mathrm{Edd}}{c} \sim \frac{L_\mathrm{Edd}}{c}, \tag{4.3}$$

and

$$\dot{E}_\mathrm{w} = \frac{1}{2}\dot{M}_\mathrm{w}v^2 \sim \frac{l^2\eta}{2\dot{m}}L_\mathrm{Edd} \sim 0.05L_\mathrm{Edd}, \tag{4.4}$$

where I have used equations (4.1, 4.2) to express the mass outflow rate and velocity in equation (4.4).

4.3   Shocks

The expression in equation (4.4) for the energy transfer rate of a black hole wind is obviously promising for driving the observed large-scale outflows. Although the interstellar medium is clumpy, the outflow bubble inflated by the wind easily sweeps past the clumps, affecting the diffuse gas (e.g. Mac Low and McCray, 1988). Furthermore, the clouds are shocked by the passing outflow and evaporate inside the hot wind bubble (Cowie and McKee, 1977), so most of their material also joins the outflow. A detailed treatment of the interaction between the clumpy ISM and the wind-driven outflow is beyond the scope of this Chapter, although I address some of the implications in Section 4.6. In the present analysis I assume that most of the sightlines from the SMBH are covered with diffuse medium, irrespective of whether they are also obscured by clumps.

The question now is how efficiently the wind energy is transmitted to the outflow. This depends crucially on how the wind interacts with the diffuse interstellar medium of the host galaxy. Since the wind is supersonic, it must decelerate violently in a reverse

shock and simultaneously drive a forward shock into the host ISM. There are two possible outcomes, which are realised under different conditions in galaxies.

The first outcome (momentum-driven flow) occurs if the shocked wind gas can cool on a timescale short compared with the motion of the shock pattern. In this case the shocked wind gas is compressed to high density and radiates away almost all of the wind kinetic energy (i.e. $\dot{E}_{\rm out} << \dot{E}_w = (\eta/2\dot{m})L_{\rm Edd}$). This shocked wind has gas pressure equal to the pre-shock ram pressure $\dot{P}_{\rm w} \simeq lL_{\rm Edd}\dot{m}/c \propto M$, and this pushes into the host ISM.

The second case (energy-driven flow) occurs if the shocked wind gas is not efficiently cooled, and instead expands as a hot bubble. Then the flow is essentially adiabatic, and has the wind energy rate, i.e. $\dot{E}_{\rm out} \simeq \dot{E}_{\rm w} = (\eta/2\dot{m})L_{\rm Edd} \sim 0.05L_{\rm Edd}$ (from equation 4.4). The hot bubble's thermal expansion makes the driving into the host ISM more vigorous than in the momentum-driven case. Observed galaxy-wide molecular outflows must be energy-driven, as demonstrated directly by their kinetic energy content (cf equation 4.4).

Which of these two very different cases occurs at a given point depends on the cooling of the shocked gas. It is easy to show that the usual atomic cooling processes (free-free and free-bound radiation) are negligible in all cases. The dominant process tending to cool the shocked black hole wind is the inverse Compton effect (Ciotti and Ostriker, 1997). The quasar radiation field is much cooler than the wind shock temperature (typically $\sim 10^7$ K and $\sim 10^{11}$ K respectively), and so cools the shocked wind provided that it is not too diluted by distance. Equations 8 and 9 of King (2003) show that this holds if and only if the shock is at distances $R \lesssim 1$ kpc from the active nucleus, since the Compton cooling time goes as R^2 and the flow time typically as R. So one may expect a momentum-driven flow close to the nucleus, and an energy-driven flow if gas can be driven far away from it (See Sections 1.3.3 and 1.3.4 for derivation of the cooling radius).

Note that the shell of the swept-up material may have a different cooling radius than the inner wind shock, because different cooling processes are important at its temperature $\sim 10^7$ K (see Section 4.5 below). However the large-scale dynamics of the outflow depend primarily on the properties of the wind bubble, and investigation of the small-scale properties is beyond the scope of this Chapter.

4.4 Outflows

For an isothermal ISM density distribution with velocity dispersion σ and gas fraction $f_{\rm g}$ (the ratio of gas density to background potential density) one can solve analytically the equation of motion for the shock pattern for both momentum-driven flow (King, 2003, 2005) and energy-driven flow (King, 2005; King et al., 2011).

In the momentum-driven case there are two distinct flow patterns, depending on the

black hole mass M. For $M < M_\sigma$, where

$$M_\sigma = \frac{f_c \kappa}{\pi G^2} \sigma^4 \simeq 4 \times 10^8 \mathrm{M}_\odot \sigma_{200}^4, \quad (4.5)$$

with $f_c = 0.16$ (the cosmological value of f_g) and $\sigma_{200} = \sigma/(200 \ \mathrm{km\,s^{-1}})$, the wind momentum is too weak to drive away the swept-up ISM, and the flow stalls at some point. For $M > M_\sigma$ the wind momentum drives the swept-up matter far from the nucleus. It is intuitively reasonable to assume that the black hole cannot easily grow its mass significantly beyond the point where it expels the local interstellar gas in this way, i.e. beyond M_σ. Equation (4.5) is very close to the observed $M - \sigma$ relation, despite having no free parameter. Detailed calculations (King et al., 2011; Power et al., 2011b) show that the SMBH is likely to grow for 1-2 additional Salpeter times after it reaches M_σ, increasing its final mass by a factor of a few. This process is less pronounced at larger redshift, when the physical size of a galaxy is smaller; on the other hand, the gas mass within the virial radius of a galaxy halo also decreases with redshift due to the same effect, so the ratio of black hole and bulge mass in fact grows with redshift, in line with current observations (Targett et al., 2012).

I conclude that outflows drive gas far from the nucleus, and thus become energy-driven, once $M \gtrsim M_\sigma$. This is evidently the case needed to explain the molecular outflows seen in Mrk231 and other galaxies.

4.5   Large-Scale Flows

In an energy-driven flow the adiabatic expansion of the shocked wind pushes the swept-up interstellar medium in a "snowplow". King (2005) and King et al. (2011) derive the analytic solution for the expansion of the shocked wind in a galaxy bulge with an isothermal mass distribution:

$$\frac{\eta}{2} l L_{\mathrm{Edd}} = \frac{2 f_g \sigma^2}{G} \left[\frac{1}{2} R^2 \dddot{R} + 3 R \dot{R} \ddot{R} + \frac{3}{2} \dot{R}^3 \right] + 10 f_g \frac{\sigma^4}{G} \dot{R}. \quad (4.6)$$

With AGN luminosity $l L_{\mathrm{Edd}}$, all such solutions tend to an attractor

$$\dot{R} = v_e \simeq \left[\frac{2 \eta l f_c}{3 f_g} \sigma^2 c \right]^{1/3} \simeq 925 \sigma_{200}^{2/3} (l f_c / f_g)^{1/3} \ \mathrm{km\,s^{-1}} \quad (4.7)$$

until the central AGN luminosity decreases significantly while the outflow is at some radius $R = R_0$. Subsequently, the expansion speed decays as

$$\dot{R}^2 = 3 \left(v_e^2 + \frac{10}{3} \sigma^2 \right) \left(\frac{1}{x^2} - \frac{2}{3 x^3} \right) - \frac{10}{3} \sigma^2 \quad (4.8)$$

where $x = R/R_0 \geq 1$. In eq. (4.7), f_{g} is the gas fraction relative to all matter. This may be lower than the value f_{c} prevailing when the earlier momentum-driven outflow establishes the $M - \sigma$ relation (4.5): gas in galaxies may be depleted, for example, through star formation.

The solutions (4.7, 4.8) describe the motion of the contact discontinuity where the shocked wind encounters swept-up interstellar gas (see Figure 4.1). The observed molecular lines are likely to come from the shocked interstellar gas ahead of this discontinuity – its temperature is much lower ($\sim 10^7$ K) than that of the shocked wind, as shall be shown below, and hence conducive to becoming a multi-phase medium (McKee and Ostriker, 1977, also see Discussion). The outer shock must run ahead of the contact discontinuity into the ambient interstellar medium in such a way that the velocity jump across it is a factor $(\gamma + 1)/(\gamma - 1)$ (where γ is the specific heat ratio). This fixes its velocity as

$$ v_{\mathrm{out}} = \frac{\gamma + 1}{2} \dot{R} \simeq 1230 \sigma_{200}^{2/3} \left(\frac{l f_{\mathrm{c}}}{f_{\mathrm{g}}} \right)^{1/3} \ \mathrm{km \ s}^{-1} \tag{4.9} $$

(where I have used $\gamma = 5/3$ to obtain the last equality). This corresponds to a shock temperature of order 10^7 K for the forward shock into the interstellar medium (as opposed to $\sim 10^{10-11}$ K for the wind shock). Since the outer shock and the contact discontinuity are very close together when energy-driven flow starts (see Fig. 4.1) this means that the outer shock is always at

$$ R_{\mathrm{out}} = \frac{\gamma + 1}{2} R. \tag{4.10} $$

The outflow rate of shocked interstellar gas is

$$ \dot{M}_{\mathrm{out}} = \frac{\mathrm{d}M(R_{\mathrm{out}})}{\mathrm{d}t} = \frac{(\gamma + 1) f_{\mathrm{g}} \sigma^2}{G} \dot{R}. \tag{4.11} $$

Assuming $M = M_\sigma$, the wind outflow rate is

$$ \dot{M}_{\mathrm{w}} \equiv \dot{m} \dot{M}_{\mathrm{Edd}} = \frac{4 f_{\mathrm{c}} \dot{m} \sigma^4}{\eta c G}. \tag{4.12} $$

I can now define a mass-loading factor for the outflow, which is the ratio of the mass flow rate in the shocked ISM to that in the wind:

$$ f_{\mathrm{L}} \equiv \frac{\dot{M}_{\mathrm{out}}}{\dot{M}_{\mathrm{w}}} = \frac{\eta(\gamma + 1)}{4\dot{m}} \frac{f_{\mathrm{g}}}{f_{\mathrm{c}}} \frac{\dot{R}c}{\sigma^2}. \tag{4.13} $$

Then the mass outflow rate is

$$ \dot{M}_{\mathrm{out}} = f_{\mathrm{L}} \dot{M}_{\mathrm{w}} = \frac{\eta(\gamma + 1)}{4} \frac{f_{\mathrm{g}}}{f_{\mathrm{c}}} \frac{\dot{R}c}{\sigma^2} \dot{M}_{\mathrm{Edd}}. \tag{4.14} $$

If the AGN is still radiating at a luminosity close to Eddington, I can use $\dot{R} = v_{\rm e}$. Now, using equation (4.7), this gives

$$f_{\rm L} = \left(\frac{2\eta c}{3\sigma}\right)^{4/3} \left(\frac{f_{\rm g}}{f_{\rm c}}\right)^{2/3} \frac{l^{1/3}}{\dot{m}} \simeq 460 \sigma_{200}^{-4/3} \frac{l^{1/3}}{\dot{m}}, \tag{4.15}$$

and

$$\dot{M}_{\rm out} \simeq 3700 \sigma_{200}^{8/3} l^{1/3} \ {\rm M}_\odot \ {\rm yr}^{-1} \tag{4.16}$$

for typical parameters, $f_{\rm g} = f_{\rm c}$ and $\gamma = 5/3$. If the central quasar is no longer active, the mass outflow rate evidently declines as $\dot{R}/v_e$ times this expression, with $\dot{R}$ given by (4.8).

It is easy to check from equations (4.9, 4.16) that the approximate equality

$$\frac{1}{2}\dot{M}_{\rm w}v_{\rm w}^2 \simeq \frac{1}{2}\dot{M}_{\rm out}v_{\rm out}^2. \tag{4.17}$$

holds, i.e. most of the wind kinetic energy ultimately goes into the mechanical energy of the outflow, as expected for energy driving. While the quasar is still active, this energy is shared between the shocked wind bubble and the outer shell of shocked ISM. Using equations (15) and (16) of King (2005), i.e. the equation of motion

$$\frac{\rm d}{{\rm d}t}\left[M(R)\dot{R}\right] + \frac{GM(R)M_{\rm tot}(R)}{R^2} = 4\pi R^2 P \tag{4.18}$$

and the energy equation

$$\frac{\rm d}{{\rm d}t}\left[\frac{4\pi R^3}{3} \times \frac{3}{2}P\right] = \frac{\eta}{2}lL_{\rm Edd} - P\frac{\rm d}{{\rm d}t}\left(\frac{4\pi}{3}R^3\right) - 4f_{\rm g}\frac{\sigma^4}{G}\dot{R}, \tag{4.19}$$

I note that the second term on the right hand side of eq. (4.19) refers to the rate of work done by the expanding bubble, i.e. the energy transfer rate to the outer shell, while the third term is the kinetic power of the swept-up outflowing gas (since $M_{\rm shell} \gg M_{\rm w}$, I can neglect the kinetic energy of the bulk motion of the shocked wind). Using eq. (4.18) to eliminate P, I find that

$$P\frac{\rm d}{{\rm d}t}\left(\frac{4\pi}{3}R^3\right) + 4f_{\rm g}\frac{\sigma^4}{G}\dot{R} = \frac{2f_{\rm g}\sigma^2}{G}\left(\dot{R}^3 + R\dot{R}\ddot{R} + 4\sigma^2\dot{R}\right). \tag{4.20}$$

I then compare this expression with the full equation of motion (eq. 4.6) and assume $\dot{R} = v_{\rm e} = {\rm const.}$ to find the ratio

$$\frac{\dot{E}_{\rm shell}}{\dot{E}_{\rm total}} = \frac{2}{3}\frac{v_{\rm e}^2 + 4\sigma^2}{v_{\rm e}^2 + \frac{10}{3}\sigma^2}. \tag{4.21}$$

In the case where $v_{\rm e} \gg \sigma$, the ratio tends to 2/3rds, i.e. the shocked wind retains 1/3

of the total incident wind kinetic energy $\dot{M}_{\rm w} v_{\rm w}^2/2$, giving 2/3rds to the swept-up gas. In the case of a weak outflow, i.e. $v_{\rm e} \simeq \sigma$, the ratio becomes $\sim 10/13$. One can see that the ratio does not depend strongly on the precise parameters of the outflow, as long as the driving continues. The energy retained in the wind and the swept-up gas has potentially observable emission signatures (see Discussion).

Equation (4.17) means that the swept-up gas must have a momentum rate greater than the Eddington value $L_{\rm Edd}/c$, since I can rewrite it as

$$\frac{\dot{P}_{\rm w}^2}{2\dot{M}_{\rm w}} \simeq \frac{\dot{P}_{\rm out}^2}{2\dot{M}_{\rm out}}, \tag{4.22}$$

where $\dot{P}_{\rm w}$ and $\dot{P}_{\rm out}$ are the momentum fluxes of the wind and the outflow, respectively. With $\dot{P}_{\rm w} = L_{\rm Edd}/c$, I find

$$\dot{P}_{\rm out} = \dot{P}_{\rm w} \left(\frac{\dot{M}_{\rm out}}{\dot{M}_{\rm w}} \right)^{1/2} = \frac{L_{\rm Edd}}{c} f_{\rm L}^{1/2} \sim 20 \sigma_{200}^{-2/3} l^{1/6} \frac{L_{\rm Edd}}{c} \tag{4.23}$$

where $f_{\rm L}$ is the mass loading factor of the outflow. The factor $f_{\rm L}^{1/2} \sim 20$ is the reason why observations consistently show $\dot{M}_{\rm out} v_{\rm out} > L_{\rm Edd}/c$.

4.6 Discussion

I have shown that large-scale outflows driven by wide-angle AGN winds should have typical velocities $v_{\rm out} \sim 1000 - 1500 \ {\rm km \, s^{-1}}$ and mass flow rates up to $\dot{M}_{\rm out} \sim 4000 \ {\rm M_\odot \, yr^{-1}}$ (equations 4.9, 4.16) if the central quasar is still active, with lower values if it has become fainter. Equations (4.9, 4.16) directly relate the outflow velocities and mass rates to the properties of the host galaxy. The outflows should have mechanical luminosities $\dot{E}_{\rm out} \sim (\eta/2) L_{\rm Edd} \sim 0.05 L_{\rm Edd}$, but (scalar) momentum flow rates $\dot{P}_{\rm out} \sim 20 L_{\rm Edd}/c$. These predictions agree well with observations (see Tables 4.1 and 4.2).

This picture predicts several other features that may aid in interpreting observations. It suggests that the molecular outflows come from clumps of cool gas embedded in the outflowing shocked ISM. They are entrained by the advancing outer shock front and persist for a long time. I note that this shock front is Rayleigh-Taylor stable since interstellar gas is compressed here. Further, the temperature of the shocked ISM is in the right range for thermal instability, leading to the development of a multi-phase medium (McKee and Ostriker, 1977). Additionally, Richtmyer-Meshkov instabilities (Kane et al., 1999) induced by the forward shock mean that new cold clumps may form in the outflow behind it. Simulations by Nayakshin & Zubovas (in preparation) show that the shocked ISM shell may fragment and $\sim 10\%$ of the total mass may end up locked in cold dense clumps.

Object	$M_{\mathrm{BH}}/\mathrm{M}_\odot$	$\sigma/$ km s^{-1}	$L_{\mathrm{bol}}/$ erg s^{-1} (l)	$\dot{M}_{\mathrm{out}}/\mathrm{M}_\odot$ yr^{-1}	$v_{\mathrm{out}}/$km s^{-1}
Mrk231$^{(a)}$	$4.7 \times 10^{7(b)}$	$120^{(b)}$	$45.69^{(c)}$ (0.80)	420	1100
Mrk231$^{(d)}$	4.7×10^{7}	120	45.69 (0.80)	700	750
Mrk231$^{(e)}$	4.7×10^{7}	120	$46.04^{(f)}$ (1.8)	1200	1200
IRAS 08572+3915$^{(e)}$	$\sim 4.5 \times 10^{7*}$	120*	45.66 (1*)	970	1260
IRAS 13120–5453$^{(e)}$	$5.3 \times 10^{6*}$	70*	44.83 (1*)	130	860
IRAS 17208–0014$^{(e)**}$	–	–	45.11 ($\ll 1$)	90	370
Mrk1157$^{(g)}$	8.3×10^{6}	100	42.57 (3.4×10^{-3})	6	350
2QZJ002830.4-281706$^{(h)}$	$5.1 \times 10^{9(i)}$	385***	46.58 (5.8×10^{-2})	2000	2000

Table 4.1: Parameters of observed large-scale outflows in molecular gas (Mrk231, IRAS 08572+3915, IRAS 13120–5453 and IRAS 17208–0014), and warm ionised gas (Mrk1157). * - the AGN is assumed to be radiating at its Eddington limit and the SMBH is assumed to lie on the $M - \sigma$ relation; ** - the galaxy is known to be starburst-dominated, so I expect a low Eddington factor and hence make no estimates; *** - the SMBH is assumed to lie on the $M - \sigma$ relation.

References: ^{a} - Rupke and Veilleux (2011); ^{b} - Tacconi et al. (2002); ^{c} - Lonsdale et al. (2003); ^{d} - Feruglio et al. (2010); ^{e} - Sturm et al. (2011); ^{f} - Veilleux et al. (2009); ^{g} - Riffel and Storchi-Bergmann (2011b); ^{h} - Cano-Díaz et al. (2012); ^{i} - Shemmer et al. (2004).

Object	$\frac{\dot{E}_{\rm out}}{0.05 L_{\rm bol}}$	$\frac{\dot{M}_{\rm out} v_{\rm out} c}{L_{\rm bol}}$	$f_{\rm L} \equiv \frac{\dot{M}_{\rm out}}{\dot{M}_{\rm acc}}$	$f_{\rm L,pred.}$	$\dot{M}_{\rm pred.}/{\rm M}_\odot~{\rm yr}^{-1}$	$v_{\rm pred.}/~{\rm km~s}^{-1}$
Mrk231	0.66	18	$490 = 22^2$	840	880	810
Mrk231	0.51	20	$820 = 29^2$	840	880	810
Mrk231	1.0	25	$1400 = 37^2$	1110	1150	1060
IRAS 08572+3915	2.1	50	$1200 = 35^2$	910	950	875
IRAS 13120–5453	0.88	31	$1080 = 33^2$	1870	220	610
IRAS 17208–0014	0.06	4.9	$396 = 20^2$	–	–	–
Mrk1157	1.3	110	$9270 = 96^2$	170	85	115
2QZJ002830.4-281706	1.3	20	$307 = 17.5^2$	74	8200	740

Table 4.2: Observationally derived versus theoretically predicted outflow parameters. The first three columns give quantities derived from observations of large-scale outflows for the objects in Table 4.1. The last three columns give the mass-loading parameter, mass sweep-out rate and terminal velocity predicted by equations (4.15), (4.16) and (4.9) respectively. With one outlier (see below), the outflow kinetic energy is always very close to 5% of $L_{\rm bol}$ (1st column) as predicted by eq. (4.4), and the momentum loading (2nd column) is always very similar to the square root of the mass loading (rhs of 3rd column), as predicted by eq. (4.23). It is striking that the relation holds both for local quasars (Mrk231), high-redshift quasars (2QZJ002830.4-281706) and low luminosity galaxies (Mrk1157). The last two columns can be directly compared with the last two columns of Table 4.1; the discrepancies in the case of Mrk1157 and 2QZJ002830.4-281706 arise due to their outflows being strongly collimated, an effect I neglect in my calculations. The only significant outlier, IRAS 17208–0014, is known to be a starburst-dominated galaxy, so I would not expect the outflow to be dominated by the AGN contribution.

This agrees with the conversion factor of $\sim 10\%$ used in the papers cited in Table 4.1 to estimate the total mass outflow rate from observed molecular species. The present model therefore predicts both the total mass outflow rates (equation 4.16) and the observational signatures used to estimate them, in good agreement with observation (Table 4.2).

Other observational signatures of large-scale outflows may include gamma rays produced when cosmic ray (CR) particles, accelerated by the inner wind shock, hit the colder ISM and shocked wind. As a result, it is a general prediction that galaxies exhibiting outflows should also show gamma-ray emission similar to the *Fermi* bubbles discussed in Chapter 2 of this Thesis, as well as by Zubovas et al. (2011) and Zubovas and Nayakshin (2012). The gamma-ray emission from distant galaxies discussed here should be intrinsically stronger than in the Milky Way, but the long integration time required to detect the Galactic bubbles (Su et al., 2010) means that these outflows may be undetectable with current instruments.

Perhaps more promisingly, these cosmic ray electrons cool and emit synchrotron radiation in the radio band. This radiation may be observable and so it would be interesting to check whether there are kpc or sub-kpc scale radio bubbles associated with the outflows.

I conclude that AGN outflows may well be what sweeps galaxies clear of gas. This theoretical conclusion agrees well with previous observational evidence (Schawinski et al., 2007) and reinforces the notion that AGN feedback is an important process in galaxy formation and evolution. Furthermore, the outflows leave clear observational signatures that persist for a significant amount of time, allowing for easier identification of past AGN activity. Therefore, outflows are a potential tracer of black hole accretion history in galaxies, a feature which may be exploited by future observations in most bands of the electromagnetic spectrum.

5

Conclusion

"The Road goes ever on and on
Down from the door where it began.
Now far ahead the Road has gone,
And I must follow, if I can,
Pursuing it with eager feet,
Until it joins some larger way
Where many paths and errands meet.
And whither then? I cannot say"

J. R. R. Tolkien, "The Lord of the Rings",
Book I, Chapter 1

5.1   Overview

In this Thesis, I have presented three investigations of the processes caused by accretion on to supermassive black holes (SMBHs) and their effects on the host galaxies of the SMBHs. The first two science Chapters were concerned with the SMBH of our own Galaxy, the well-studied object named Sgr A*, while the third one presented a more general analysis of SMBH outflows.

In the first science Chapter, I investigated the propagation of an outflow inflated by a short outburst of quasar activity in Sgr A*, speculated to have occurred contemporaneously with the star formation event in the central parsec of the Galaxy 6 Myr ago. The goal was to find out whether the recently discovered *Fermi* bubbles may be explained by this model.

In Chapter 3, I suggested a possible mechanism for producing the flares that are currently observed to occur several times a day in Sgr A*. I proposed that asteroids born around the stars in close proximity to the SMBH are routinely deflected on to orbits that bring them within their tidal disruption radius. The disrupted remnants may then evaporate in the tenuous accretion flow around the SMBH and provide the fuel for the flaring events.

The last Chapter is devoted to a more general exploration of the properties of large-scale outflows from SMBHs. I present the conditions under which the outflows are energy driven and then derive the outflow properties. I also compare the derived observable properties with the results of recent observations of large-scale outflows from several nearby quasars.

I now describe the results of each Chapter in more detail. I also discuss the possible future developments and improvements of these investigations.

5.2   *Fermi* bubbles and the activity history of Sgr A*

Both the analytical and numerical calculations reproduce the salient properties of the observed *Fermi* bubbles (Su et al., 2010). A quasi-spherical outflow from Sgr A*, driven by the AGN wind for $t_q = 1$ Myr, is collimated by the Central Molecular Zone (CMZ) and expands predominantly in the direction perpendicular to the Galactic plane, where gas density is low ($f_g = 10^{-3}$ times the background density). By $t = 6$ Myr, i.e. today, the two teardrop-shaped cavities have expanded to a height $R \sim 11$ kpc and width $d \sim 9$ kpc, similar to the size and shape of the *Fermi* bubbles.

In addition to bubble morphology, the model reproduces the energy content of the cavities. This is closely related to the observable emission from the bubble (see also Chapter 4 and Section 5.4). While I do not model the radiative processes in any detail, both the analytical and numerical results are consistent with there being gamma ray

emission produced by cosmic ray electrons accelerated by the shocks inside the bubbles. Thermal emission from the hot gas inside the bubbles may explain the X-ray "limbs" that have been observed with the ROSAT satellite. Finally, synchrotron emission from the same cosmic ray electrons that produce the gamma rays may be responsible for the haze in the microwave emission associated with the region of the bubbles.

The Central Molecular Zone is also significantly affected by feedback. The outflow from Sgr A* is unable to disperse the dense gas; however, approximately half of the gas in the original distribution is compressed into a thin ring, which subsequently spreads due to viscous forces, but persists for the duration of the simulation. Gas density in the ring is large enough to make it susceptible to fragmentation, which produces at least one massive ($M \sim 10^7$ M$_\odot$) compact ($R \sim 5$ pc) gas clump. The properties of the clumpy ring are reminiscent of the recently-discovered *Herschel* ring of molecular clouds and streams in the Galactic centre (Molinari et al., 2011). Detailed properties of this clump and the likely onset of star formation in the ring cannot be resolved in the simulations; however, both observations and modelling suggest that a recent perturbation to the CMZ may have been responsible for the present elevated star-formation rate in the region.

Finally, the results of this investigation show that the same AGN wind feedback model is applicable to a short outburst in an otherwise quiescent galaxy as well as to a gas-rich galaxy during the quasar epoch, as investigated previously (Nayakshin and Power, 2010). They also reveal that dynamical evidence of past AGN activity may persist in quiescent galaxies for an order of magnitude longer than the duration of the activity. This evidence may provide a wealth of information about the activity history of SMBHs in the local Universe.

5.2.1   Further work

In the future, the simulations presented in this Chapter may be enhanced in several directions. Possible improvements include a better treatment of the AGN wind, inclusion of radiative processes and adaptation of the model for the analysis of outflows in other galaxies.

5.2.1.1   Our Galaxy

With regard to the *Fermi* bubbles, a major improvement to the simulations carried out so far would be the inclusion of a numerical treatment of the radiative process. A thorough understanding of the emission expected from an outflow bubble and its surrounding shell would not only allow direct comparison with observations, but also show what emission we may expect from similar processes in other galaxies (see below and Section 5.4).

Implementation of a numerical treatment of radiation from the outflow requires several other improvements to the current set up. First of all, the fast wind emanating from the

AGN must be treated hydrodynamically, so that its interaction with the expanding gas shell – the potentially complicated geometry and the presence of various shock fronts – is modelled properly. Secondly, a lot of the emission depends on the presence of cosmic rays (CRs); these particles must be accelerated in the shocks within the outflow. In order to predict the CR density and energy distribution, the shocks have to be resolved. As the shocks are expected to develop due to the small-scale instabilities along the contact discontinuity, it is important to have much better resolution simulations (and perhaps novel numerical techniques) in order to get a clear picture of the detailed morphology of the outflow.

In addition, the initial conditions used in the simulations in this Thesis are overly simplified. An improvement in this regard, e.g. by using a triaxial background potential and a diffuse gas distribution more representative of the bulge and the gaseous halo of the Milky Way, would provide better results and allow for more detailed comparison with observations of the present-day structures in the Galaxy.

Overall, these improvements may one day allow researchers to trace the history of activity in Sgr A* within the past several Myr, and perhaps even longer, in great detail. This would enhance our general understanding of the SMBH activity and galaxy evolution on million-year timescales.

5.2.1.2   Other galaxies

In addition to the improvements listed above, these simulations may be enhanced and used to study other galaxies. Energy-driven outflows (see Chapter 4) are likely to be the process quenching star formation in galaxies and turning their colours from blue to red (cf. Schawinski et al., 2007). Simulations of this process, with the associated complications of aspherical galaxy geometry, triggered star formation and turbulent gas flows can shed light upon numerous details of galaxy evolution, such as the origin of the black hole - bulge mass relation (see Section 1.2), build-up of the stellar populations and the quenching of cooling flows in clusters. Overall, galaxy-scale hydrodynamical simulations of AGN feedback provide a crucial stepping stone linking the small-scale accretion physics with the large-scale evolution of cosmic structure. In the future, such simulations will be indispensable when investigating the details of the build-up of the Universe we see around us today.

5.3   Asteroids and Sgr A* today

The results of the model presented in Chapter 3 are consistent with the observed flare frequency and luminosity distribution. The number of observable flares per day is found to be $\lesssim 8$ per day, slightly more than, but consistent with, the observed number (~ 1 per

day in X-rays and ~ 3 per day in the IR). In addition, $\lesssim 3.5$ flares with luminosity at least equivalent to the brightest observed one may have occurred during the total time of *Chandra* observations of Sgr A*, again not too dissimilar from the actual observed value.

While I do not model the flare spectra, my results tie in with previous work in the field. The "transient plasma blob" model developed by, e.g., Trap et al. (2011), is particularly interesting, as it requires a short-lived expanding population of relativistic particles to appear in the quiescent accretion flow around Sgr A*. Such a population should be created as the tidally disrupted asteroid remnants evaporate. Various plasma instabilities may accelerate a fraction of both electrons and ions to highly relativistic velocities, providing the seed for emission required in the "expanding blob" model.

5.3.1 Future prospects

The model makes a few testable predictions. First of all, upcoming long-term observations of Sgr A* should reveal ever larger flares, with their luminosity unconstrained by the correlation of X-ray and radio luminosities of black holes (the Fundamental Plane of black hole activity; Markoff, 2005). Conversely, models that envision an internally induced trigger for the flares predict a rise in radio power accompanying X-ray flares brighter than the brightest ones currently observed.

Another prediction is that if the quiescent luminosity of Sgr A* increases, the flare luminosity should not increase significantly, if at all. The only change to an incoming asteroid would be a more rapid evaporation in the denser accretion flow; this may shorten the flare timescale slightly, correspondingly increasing the luminosity. However, without detailed modelling of the evolution of evaporated material, it is not possible to quantify this prediction. On the other hand, if the flare luminosity caused by an asteroid of a given mass does not change significantly, the frequency of flares at a given luminosity should also stay the same. An opportunity to test this prediction may come in mid-2013, when the recently-discovered gas cloud G2 (Gillessen et al., 2012) is expected to reach the pericentre of its orbit, which will put it at a distance $R \sim 3000 R_S$ from Sgr A*. The subsequent tidal disruption of the cloud may provide additional fuel for Sgr A*, creating a long-lasting higher luminosity state. Using it as a background, the flare luminosity distribution may be probed and various hypotheses of flare origin tested.

Finally, the model does not require any specific conditions in the accretion flow around Sgr A*. The only requirement is that there should be a cloud of asteroids stripped from their parent stars. A large number of galaxies have nuclear stellar clusters, which presumably provide a supply of asteroids. Therefore the vast majority of galaxies experience the same flaring events as the one described for the case of the Milky Way. In other galaxies, the flares are obviously more difficult to observe, both due to distance and possible higher quiescent luminosity of SMBHs, but such discoveries are possible with dedicated

observational campaigns.

5.4 Clearing the galaxies: possible future of Sgr A* and the Milky Way

In the final Chapter, I found that the derived observational properties (mass flow rate, outflow velocity, momentum and energy fluxes) of large-scale outflows match very well with those recently observed in several active galaxies. Furthermore, the energy input by the black hole radiation field through a fast wind into an energy-driven outflow is enough to unbind the gas in a galaxy. Therefore black hole outflows have the potential to clear gas from galaxies and suppress further star formation, transforming them from blue to red in colour.

Further implications of the Chapter results relate to the observational evidence of past AGN outflows (see also Chapter 2 and Section 5.2). As outflows may persist in the "stalling" state for an order of magnitude longer than the duration of the quasar phase driving them, they are a potential tracer of AGN activity history. Combined with the fact that outflows may be revealed by a number of processes in different radiation bands (radio synchrotron emission, molecular IR from embedded clouds, thermal X-rays and CR-induced γ-ray emission), this makes AGN-outflow-inflated bubbles a very interesting future observation target.

5.4.1 Model enhancement

In addition to quenching star formation by sweeping the galaxy clear of gas, an AGN outflow may also trigger a burst of star formation by compressing the ISM as it expands. An analytical analysis of the stability of such a shell, similar to that done in Vishniac (1983), may reveal interesting behaviour and constrain the timescales for clump development and hence onset of star formation activity. The break-up of a shock front into self-gravitating clumps would also affect the large-scale dynamics of the outflow, but analysing that effect analytically may be impossible.

Researchers performing numerical simulations of galaxy evolution may implement large-scale wind-driven outflows in order to better model the processes that form the present-day galaxy population in the Universe. In the future, I intend to work towards creating and running galaxy evolution simulations as self-consistently as possible, with AGN wind feedback as an important ingredient.

Finally, the processes described in Chapter 4 are potentially relevant even for our own Galaxy. Within the next $\sim 3 - 5$ Gyr, the Milky Way is going to merge with the Andromeda galaxy (Cox and Loeb, 2008; Dubinski, 2006). This event will almost undoubtedly channel large quantities of gas to the central parts of both galaxies, while

simultaneously transforming their morphologies into a combined elliptical shape. The two SMBHs – Sgr A* and M31* – will suddenly find themselves in gas-rich surroundings and light up as AGN or even quasars. The resulting winds and outflows may very well sweep the combined galaxy clear of gas, leaving it as a red-and-dead spheroid. While this is not an immediately relevant issue, understanding the ultimate fate of our cosmic home is an endeavour worth pursuing.

References

Agertz, O., Moore, B., Stadel, J., Potter, D., Miniati, F., Read, J., Mayer, L., Gawryszczak, A., Kravtsov, A., Nordlund, Å., Pearce, F., Quilis, V., Rudd, D., Springel, V., Stone, J., Tasker, E., Teyssier, R., Wadsley, J., and Walder, R.: 2007, *MNRAS* **380**, 963

Aitken, D. K., Greaves, J., Chrysostomou, A., Jenness, T., Holland, W., Hough, J. H., Pierce-Price, D., and Richer, J.: 2000, *ApJ* **534**, L173

Alexander, D. M. and Hickox, R. C.: 2012, *NewAR* **56**, 93

Alexander, R. D., Smedley, S. L., Nayakshin, S., and King, A. R.: 2012, *MNRAS* **419**, 1970

Alexander, T.: 2005, *Phys. Rep.* **419**, 65

Alibert, Y., Mordasini, C., Benz, W., and Winisdoerffer, C.: 2005, *A&A* **434**, 343

Aller, M. C. and Richstone, D. O.: 2007, *ApJ* **665**, 120

Ascasibar, Y., Jean, P., Bœhm, C., and Knödlseder, J.: 2006, *MNRAS* **368**, 1695

Asphaug, E. and Benz, W.: 1996, *Icarus* **121**, 225

Baganoff, F. K., Bautz, M. W., Brandt, W. N., Chartas, G., Feigelson, E. D., Garmire, G. P., Maeda, Y., Morris, M., Ricker, G. R., Townsley, L. K., and Walter, F.: 2001, *Nature* **413**, 45

Baganoff, F. K., Maeda, Y., Morris, M., Bautz, M. W., Brandt, W. N., Cui, W., Doty, J. P., Feigelson, E. D., Garmire, G. P., Pravdo, S. H., Ricker, G. R., and Townsley, L. K.: 2003, *ApJ* **591**, 891

Bagla, J. S. and Ray, S.: 2003, *NewA* **8**, 665

Bahcall, J. N. and Wolf, R. A.: 1976, *ApJ* **209**, 214

Balbus, S. A.: 2003, *ARA&A* **41**, 555

Balick, B. and Brown, R. L.: 1974, *ApJ* **194**, 265

Balsara, D. S.: 1995, *Journal of Computational Physics* **121**, 357

Bartko, H., Martins, F., Fritz, T. K., Genzel, R., Levin, Y., Perets, H. B., Paumard, T., Nayakshin, S., Gerhard, O., Alexander, T., Dodds-Eden, K., Eisenhauer, F., Gillessen, S., Mascetti, L., Ott, T., Perrin, G., Pfuhl, O., Reid, M. J., Rouan, D., Sternberg, A., and Trippe, S.: 2009, *ApJ* **697**, 1741

Bartko, H., Martins, F., Trippe, S., Fritz, T. K., Genzel, R., Ott, T., Eisenhauer, F., Gillessen, S., Paumard, T., Alexander, T., Dodds-Eden, K., Gerhard, O., Levin, Y., Mascetti, L., Nayakshin, S., Perets, H. B., Perrin, G., Pfuhl, O., Reid, M. J., Rouan, D., Zilka, M., and Sternberg, A.: 2010, *ApJ* **708**, 834

Batcheldor, D.: 2010, *ApJ* **711**, L108

Begelman, M. C., Volonteri, M., and Rees, M. J.: 2006, *MNRAS* **370**, 289

Bell, E. F., Wolf, C., Meisenheimer, K., Rix, H.-W., Borch, A., Dye, S., Kleinheinrich, M., Wisotzki, L., and McIntosh, D. H.: 2004, *ApJ* **608**, 752

Belokurov, V., Zucker, D. B., Evans, N. W., Gilmore, G., Vidrih, S., Bramich, D. M., Newberg, H. J., Wyse, R. F. G., Irwin, M. J., Fellhauer, M., Hewett, P. C., Walton, N. A., Wilkinson, M. I., Cole, N., Yanny, B., Rockosi, C. M., Beers, T. C., Bell, E. F., Brinkmann, J., Ivezić, Ž., and Lupton, R.: 2006, *ApJ* **642**, L137

Benz, W. and Asphaug, E.: 1999, *Icarus* **142**, 5

Berti, E. and Volonteri, M.: 2008, *ApJ* **684**, 822

Biermann, P. L., Becker, J. K., Caceres, G., Meli, A., Seo, E.-S., and Stanev, T.: 2010, *ApJ* **710**, L53

Binney, J. and Tremaine, S.: 2008, *Galactic Dynamics: Second Edition*, Princeton University Press

Blandford, R. and Eichler, D.: 1987, *Phys. Rep.* **154**, 1

Blandford, R. D. and Begelman, M. C.: 1999, *MNRAS* **303**, L1

Bloom, J. S., Giannios, D., Metzger, B. D., Cenko, S. B., Perley, D. A., Butler, N. R., Tanvir, N. R., Levan, A. J., O'Brien, P. T., Strubbe, L. E., De Colle, F., Ramirez-Ruiz, E., Lee, W. H., Nayakshin, S., Quataert, E., King, A. R., Cucchiara, A., Guillochon, J., Bower, G. C., Fruchter, A. S., Morgan, A. N., and van der Horst, A. J.: 2011, *Science* **333**, 203

Bode, P., Ostriker, J. P., and Xu, G.: 2000, *ApJS* **128**, 561

Bonnell, I. A. and Rice, W. K. M.: 2008, *Science* **321**, 1060

Booth, C. M. and Schaye, J.: 2009, *MNRAS* **398**, 53

Bottke, W. F., Durda, D. D., Nesvorny, D., Jedicke, R., Morbidelli, A., Vokrouhlicky, D., and Levison, H.: 2005, *Icarus* **175**, 111

Bower, G. C., Wright, M. C. H., Falcke, H., and Backer, D. C.: 2003, *ApJ* **588**, 331

Bowyer, S., Byram, E. T., Chubb, T. A., and Friedman, H.: 1965, *Science* **147**, 394

Britt, D. T., Yeomans, D., Housen, K., and Consolmagno, G.: 2002, *Asteroids III* pp 485–500

Broderick, A. E. and Loeb, A.: 2005, *MNRAS* **363**, 353

Bronshten, V. A.: 1983, *Physics of meteoric phenomena*

Brown, W. R., Geller, M. J., Kenyon, S. J., and Kurtz, M. J.: 2005, *ApJ* **622**, L33

Butcher, J.: 2003, *Numerical methods for ordinary differential equations*, J. Wiley, Chichester, West Sussex, England Hoboken, NJ

Campana, S., Lodato, G., D'Avanzo, P., Panagia, N., Rossi, E. M., Valle, M. D., Tagliaferri, G., Antonelli, L. A., Covino, S., Ghirlanda, G., Ghisellini, G., Melandri, A., Pian, E., Salvaterra, R., Cusumano, G., D'Elia, V., Fugazza, D., Palazzi, E., Sbarufatti, B., and D. Vergani, S.: 2011, *Nature* **480**, 69

Cano-Díaz, M., Maiolino, R., Marconi, A., Netzer, H., Shemmer, O., and Cresci, G.: 2012, *A&A* **537**, L8

Carter, B.: 1973, *Communications in Mathematical Physics* **30**, 261

Chandrasekhar, S.: 1943, *ApJ* **97**, 255

Chapman, C. R.: 1978, in D. Morrison & W. C. Wells (ed.), *NASA Conference Publication*, Vol. 2053 of *NASA Conference Publication*, pp 145–160

Cheng, K.-S., Chernyshov, D. O., Dogiel, V. A., Ko, C.-M., and Ip, W.-H.: 2011, *ApJ* **731**, L17+

Cimatti, A., Daddi, E., and Renzini, A.: 2006, *A&A* **453**, L29

Ciotti, L. and Ostriker, J. P.: 1997, *ApJ* **487**, L105+

Collin, S. and Zahn, J.-P.: 1999, *A&A* **344**, 433

Courant, R., Friedrichs, K., and Lewy, H.: 1928, *Mathematische Annalen* **100**, 32

Cowie, L. L. and McKee, C. F.: 1977, *ApJ* **211**, 135

Cox, T. J. and Loeb, A.: 2008, *MNRAS* **386**, 461

Crocker, R. M.: 2011, *ArXiv e-prints*

Crocker, R. M. and Aharonian, F.: 2011, *Physical Review Letters* **106(10)**, 101102

Crocker, R. M., Jones, D. I., Aharonian, F., Law, C. J., Melia, F., Oka, T., and Ott, J.: 2011, *MNRAS* **413**, 763

Cuadra, J., Nayakshin, S., and Martins, F.: 2008, *MNRAS* **383**, 458

Cuadra, J., Nayakshin, S., Springel, V., and Di Matteo, T.: 2006, *MNRAS* **366**, 358

Cuadra, J., Nayakshin, S., and Sunyaev, R.: 2003, *A&A* **411**, 405

Cullen, L. and Dehnen, W.: 2010, *MNRAS* **408**, 669

Dahmen, G., Huttemeister, S., Wilson, T. L., and Mauersberger, R.: 1998, *A&A* **331**, 959

Dame, T. M., Hartmann, D., and Thaddeus, P.: 2001, *ApJ* **547**, 792

Devecchi, B., Volonteri, M., Colpi, M., and Haardt, F.: 2010, *MNRAS* **409**, 1057

Di Matteo, T., Springel, V., and Hernquist, L.: 2005, *Nature* **433**, 604

Dobler, G.: 2012, *ApJ* **750**, 17

Dobler, G., Cholis, I., and Weiner, N.: 2011, *ApJ* **741**, 25

Dobler, G., Finkbeiner, D. P., Cholis, I., Slatyer, T., and Weiner, N.: 2010, *ApJ* **717**, 825

Dodds-Eden, K., Gillessen, S., Fritz, T. K., Eisenhauer, F., Trippe, S., Genzel, R., Ott, T., Bartko, H., Pfuhl, O., Bower, G., Goldwurm, A., Porquet, D., Trap, G., and Yusef-Zadeh, F.: 2011, *ApJ* **728**, 37

Dodds-Eden, K., Porquet, D., Trap, G., Quataert, E., Haubois, X., Gillessen, S., Grosso, N., Pantin, E., Falcke, H., Rouan, D., Genzel, R., Hasinger, G., Goldwurm, A., Yusef-Zadeh, F., Clenet, Y., Trippe, S., Lagage, P.-O., Bartko, H., Eisenhauer, F., Ott, T., Paumard, T., Perrin, G., Yuan, F., Fritz, T. K., and Mascetti, L.: 2009, *ApJ* **698**, 676

Dodds-Eden, K., Sharma, P., Quataert, E., Genzel, R., Gillessen, S., Eisenhauer, F., and Porquet, D.: 2010, *ApJ* **725**, 450

Dopita, M. A.: 1985, *ApJ* **295**, L5

Dubinski, J.: 2006, *S&T* **112(4)**, 040000

Eckart, A., Baganoff, F. K., Schödel, R., Morris, M., Genzel, R., Bower, G. C., Marrone, D., Moran, J. M., Viehmann, T., Bautz, M. W., Brandt, W. N., Garmire, G. P., Ott, T., Trippe, S., Ricker, G. R., Straubmeier, C., Roberts, D. A., Yusef-Zadeh, F., Zhao, J. H., and Rao, R.: 2006a, *A&A* **450**, 535

Eckart, A., Schodel, R., Meyer, L., Trippe, S., Ott, T., Genzel, R., Muzic, K., Moultaka, J., Straubmeier, C., Baganoff, F. K., Morris, M., and Bower, G. C.: 2006b, *Journal of Physics Conference Series* **54**, 391

Edge, D. O., Scheuer, P. A. G., and Shakeshaft, J. R.: 1958, *MNRAS* **118**, 183

Edge, D. O., Shakeshaft, J. R., McAdam, W. B., Baldwin, J. E., and Archer, S.: 1959, *MmRAS* **68**, 37

Einstein, A.: 1915, *Sitzungsberichte der Königlich Preußischen Akademie der Wissenschaften (Berlin), Seite 844-847.* pp 844–847

Esquej, P., Saxton, R. D., Komossa, S., Read, A. M., Freyberg, M. J., Hasinger, G., García-Hernández, D. A., Lu, H., Rodriguez Zaurín, J., Sánchez-Portal, M., and Zhou, H.: 2008, *A&A* **489**, 543

Euler, L.: 1768, *Institutionum Calculi integralis, 1*

Everett, J. E., Zweibel, E. G., Benjamin, R. A., McCammon, D., Rocks, L., and Gallagher, III, J. S.: 2008, *ApJ* **674**, 258

Falcke, H., Biermann, P. L., Duschl, W. J., and Mezger, P. G.: 1993, *A&A* **270**, 102

Falcke, H. and Markoff, S.: 2000, *A&A* **362**, 113

Falcke, H., Melia, F., and Agol, E.: 2000, *ApJ* **528**, L13

Faucher-Giguère, C.-A. and Quataert, E.: 2012, *MNRAS* **425**, 605

Feoli, A. and Mancini, L.: 2009, *ApJ* **703**, 1502

Ferrarese, L., Côté, P., Dalla Bontà, E., Peng, E. W., Merritt, D., Jordán, A., Blakeslee, J. P., Haşegan, M., Mei, S., Piatek, S., Tonry, J. L., and West, M. J.: 2006, *ApJ* **644**, L21

Ferrarese, L. and Merritt, D.: 2000, *ApJ* **539**, L9

Feruglio, C., Maiolino, R., Piconcelli, E., Menci, N., Aussel, H., Lamastra, A., and Fiore, F.: 2010, *A&A* **518**, L155+

Figer, D. F., Kim, S. S., Morris, M., Serabyn, E., Rich, R. M., and McLean, I. S.: 1999a, *ApJ* **525**, 750

Figer, D. F., McLean, I. S., and Morris, M.: 1999b, *ApJ* **514**, 202

Finkbeiner, D. P.: 2004, *ApJ* **614**, 186

Fish, V. L., Doeleman, S. S., Beaudoin, C., Blundell, R., Bolin, D. E., Bower, G. C., Chamberlin, R., Freund, R., Friberg, P., Gurwell, M. A., Honma, M., Inoue, M., Krichbaum, T. P., Lamb, J., Marrone, D. P., Moran, J. M., Oyama, T., Plambeck, R., Primiani, R., Rogers, A. E. E., Smythe, D. L., SooHoo, J., Strittmatter, P., Tilanus, R. P. J., Titus, M., Weintroub, J., Wright, M., Woody, D., Young, K. H., and Ziurys, L. M.: 2011, *ApJ* **727**, L36

Frank, J., King, A., and Raine, D. J.: 2002, *Accretion Power in Astrophysics: Third Edition*

Freitag, M., Amaro-Seoane, P., and Kalogera, V.: 2006, *ApJ* **649**, 91

Gammie, C. F.: 2001, *ApJ* **553**, 174

Gebhardt, K., Bender, R., Bower, G., Dressler, A., Faber, S. M., Filippenko, A. V., Green, R., Grillmair, C., Ho, L. C., Kormendy, J., Lauer, T. R., Magorrian, J., Pinkney, J., Richstone, D., and Tremaine, S.: 2000a, *ApJ* **539**, L13

Gebhardt, K., Kormendy, J., Ho, L. C., Bender, R., Bower, G., Dressler, A., Faber, S. M., Filippenko, A. V., Green, R., Grillmair, C., Lauer, T. R., Magorrian, J., Pinkney, J., Richstone, D., and Tremaine, S.: 2000b, *ApJ* **543**, L5

Genzel, R., Schödel, R., Ott, T., Eckart, A., Alexander, T., Lacombe, F., Rouan, D., and Aschenbach, B.: 2003a, *Nature* **425**, 934

Genzel, R., Schödel, R., Ott, T., Eisenhauer, F., Hofmann, R., Lehnert, M., Eckart, A., Alexander, T., Sternberg, A., Lenzen, R., Clénet, Y., Lacombe, F., Rouan, D., Renzini, A., and Tacconi-Garman, L. E.: 2003b, *ApJ* **594**, 812

Ghez, A. M., Salim, S., Hornstein, S. D., Tanner, A., Lu, J. R., Morris, M., Becklin, E. E., and Duchêne, G.: 2005, *ApJ* **620**, 744

Ghez, A. M., Salim, S., Weinberg, N. N., Lu, J. R., Do, T., Dunn, J. K., Matthews, K., Morris, M. R., Yelda, S., Becklin, E. E., Kremenek, T., Milosavljevic, M., and Naiman, J.: 2008, *ApJ* **689**, 1044

Ghez, A. M., Wright, S. A., Matthews, K., Thompson, D., Le Mignant, D., Tanner, A., Hornstein, S. D., Morris, M., Becklin, E. E., and Soifer, B. T.: 2004, *ApJ* **601**, L159

Gillessen, S., Genzel, R., Fritz, T. K., Quataert, E., Alig, C., Burkert, A., Cuadra, J., Eisenhauer, F., Pfuhl, O., Dodds-Eden, K., Gammie, C. F., and Ott, T.: 2012, *Nature* **481**, 51

Gillispie, C. C.: 1997, *Pierre-Simon Laplace (1749-1827) : a life in exact science*

Gingold, R. A. and Monaghan, J. J.: 1977, *MNRAS* **181**, 375

Goodman, J.: 2003, *MNRAS* **339**, 937

Goto, M., Usuda, T., Nagata, T., Geballe, T. R., McCall, B. J., Indriolo, N., Suto, H., Henning, T., Morong, C. P., and Oka, T.: 2008, *ApJ* **688**, 306

Graham, A. W.: 2008, *ApJ* **680**, 143

Greene, J. E., Peng, C. Y., Kim, M., Kuo, C.-Y., Braatz, J. A., Violette Impellizzeri, C. M., Condon, J. J., Lo, K. Y., Henkel, C., and Reid, M. J.: 2010a, *ApJ* **721**, 26

Greene, J. E., Peng, C. Y., and Ludwig, R. R.: 2010b, *ApJ* **709**, 937

Guesten, R., Genzel, R., Wright, M. C. H., Jaffe, D. T., Stutzki, J., and Harris, A. I.: 1987, *ApJ* **318**, 124

Gültekin, K., Richstone, D. O., Gebhardt, K., Lauer, T. R., Tremaine, S., Aller, M. C., Bender, R., Dressler, A., Faber, S. M., Filippenko, A. V., Green, R., Ho, L. C., Kormendy, J., Magorrian, J., Pinkney, J., and Siopis, C.: 2009, *ApJ* **698**, 198

Gültekin, K., Tremaine, S., Loeb, A., and Richstone, D. O.: 2011, *ApJ* **738**, 17

Guo, F. and Mathews, W. G.: 2011, *ArXiv e-prints*

Häring, N. and Rix, H.-W.: 2004, *ApJ* **604**, L89

Harms, R. J., Ford, H. C., Tsvetanov, Z. I., Hartig, G. F., Dressel, L. L., Kriss, G. A., Bohlin, R., Davidsen, A. F., Margon, B., and Kochhar, A. K.: 1994, *ApJ* **435**, L35

Herrnstein, R. M., Zhao, J., Bower, G. C., and Goss, W. M.: 2004, *AJ* **127**, 3399

Hills, J. G.: 1988, *Nature* **331**, 687

Ho, L. C.: 2008, *ARA&A* **46**, 475

Hobbs, A. and Nayakshin, S.: 2009, *MNRAS* **394**, 191

Hobbs, A., Nayakshin, S., Power, C., and King, A.: 2011, *MNRAS* **413**, 2633

Hopkins, P. F., Hernquist, L., Cox, T. J., Robertson, B., and Krause, E.: 2007, *ApJ* **669**, 67

Hornstein, S. D., Matthews, K., Ghez, A. M., Lu, J. R., Morris, M., Becklin, E. E., Rafelski, M., and Baganoff, F. K.: 2007, *ApJ* **667**, 900

Immer, K., Schuller, F., Omont, A., and Menten, K. M.: 2012, *A&A* **537**, A121

Jones, P. A., Burton, M. G., Cunningham, M. R., Requena-Torres, M. A., Menten, K. M., Schilke, P., Belloche, A., Leurini, S., Martín-Pintado, J., Ott, J., and Walsh, A. J.: 2011, *MNRAS* p. 1895

Kane, J., Drake, R. P., and Remington, B. A.: 1999, *ApJ* **511**, 335

Kerr, R. P.: 1963, *Physical Review Letters* **11**, 237

King, A.: 2003, *ApJ* **596**, L27

King, A.: 2005, *ApJ* **635**, L121

King, A. R.: 2010a, *MNRAS* **408**, L95

King, A. R.: 2010b, *MNRAS* **402**, 1516

King, A. R., Lubow, S. H., Ogilvie, G. I., and Pringle, J. E.: 2005, *MNRAS* **363**, 49

King, A. R. and Pounds, K. A.: 2003, *MNRAS* **345**, 657

King, A. R. and Pringle, J. E.: 2006, *MNRAS* **373**, L90

King, A. R. and Pringle, J. E.: 2007, *MNRAS* **377**, L25

King, A. R., Zubovas, K., and Power, C.: 2011, *MNRAS* **415**, L6

Kinney, A. L., Schmitt, H. R., Clarke, C. J., Pringle, J. E., Ulvestad, J. S., and Antonucci, R. R. J.: 2000, *ApJ* **537**, 152

Kolykhalov, P. I. and Syunyaev, R. A.: 1980, *Soviet Astronomy Letters* **6**, 357

Kompaneets, A. S.: 1960, *Soviet Physics Doklady* **5**, 46

Kormendy, J. and Bender, R.: 2011, *Nature* **469**, 377

Kormendy, J., Bender, R., and Cornell, M. E.: 2011, *Nature* **469**, 374

Kormendy, J. and Richstone, D.: 1995, *ARA&A* **33**, 581

Korycansky, D. G. and Asphaug, E.: 2006, *Icarus* **181**, 605

Kostić, U., Čadež, A., Calvani, M., and Gomboc, A.: 2009, *A&A* **496**, 307

Koushiappas, S. M., Bullock, J. S., and Dekel, A.: 2004, *MNRAS* **354**, 292

Krichbaum, T. P., Graham, D. A., Witzel, A., Greve, A., Wink, J. E., Grewing, M., Colomer, F., de Vicente, P., Gomez-Gonzalez, J., Baudry, A., and Zensus, J. A.: 1998, *A&A* **335**, L106

Krichbaum, T. P., Zensus, J. A., Witzel, A., Mezger, P. G., Standke, K. J., Schalinski, C. J., Alberdi, A., Marcaide, J. M., Zylka, R., Rogers, A. E. E., Booth, R. S., Ronnang, B. O., Colomer, F., Bartel, N., and Shapiro, I. I.: 1993, *A&A* **274**, L37

Kunneriath, D., Witzel, G., Eckart, A., Zamaninasab, M., Gießübel, R., Schödel, R., Baganoff, F. K., Morris, M. R., Dovčiak, M., Duschl, W. J., García-Marín, M., Karas, V., König, S., Krichbaum, T. P., Krips, M., Lu, R.-S., Mauerhan, J., Moultaka, J., Mužić, K., Sabha, N., Najarro, F., Pott, J.-U., Schuster, K. F., Sjouwerman, L. O., Straubmeier, C., Thum, C., Vogel, S. N., Teuben, P., Weiss, A., Wiesemeyer, H., and Zensus, J. A.: 2010, *A&A* **517**, A46+

Kusunose, M. and Takahara, F.: 2011, *ApJ* **726**, 54

Lánczos, C.: 1922, *Physikalische Zeitschrift* **23**, 537

Laor, A.: 2001, *ApJ* **553**, 677

Laplace, P. S.: 1796, *Exposition du Systeme du Monde*

Laplace, P. S.: 1799, *Allgemeine Geographische Ephemeriden* **4**, 1

Law, D. R. and Majewski, S. R.: 2010, *ApJ* **714**, 229

Lemaître, G.: 1933, *Annales de la Societe Scietifique de Bruxelles* **53**, 51

Levin, Y. and Beloborodov, A. M.: 2003, *ApJ* **590**, L33

Lin, D. N. C. and Papaloizou, J. C. B.: 1996, *ARA&A* **34**, 703

Liu, B. F., Yuan, W., Meyer, F., Meyer-Hofmeister, E., and Xie, G. Z.: 1999, *ApJ* **527**, L17

Liu, S., Petrosian, V., and Melia, F.: 2004, *ApJ* **611**, L101

Lodato, G., King, A. R., and Pringle, J. E.: 2009, *MNRAS* **392**, 332

Lonsdale, C. J., Lonsdale, C. J., Smith, H. E., and Diamond, P. J.: 2003, *ApJ* **592**, 804

Lu, J. R., Ghez, A. M., Hornstein, S. D., Morris, M. R., Becklin, E. E., and Matthews, K.: 2009, *ApJ* **690**, 1463

Lucy, L. B.: 1977, *AJ* **82**, 1013

Lynden-Bell, D.: 1969, *Nature* **223**, 690

Mac Low, M.-M. and McCray, R.: 1988, *ApJ* **324**, 776

Mac Low, M.-M., McCray, R., and Norman, M. L.: 1989, *ApJ* **337**, 141

Mac Low, M.-M. and Norman, M. L.: 1993, *ApJ* **407**, 207

Magorrian, J., Tremaine, S., Richstone, D., Bender, R., Bower, G., Dressler, A., Faber, S. M., Gebhardt, K., Green, R., Grillmair, C., Kormendy, J., and Lauer, T.: 1998, *AJ* **115**, 2285

Maitra, D., Markoff, S., and Falcke, H.: 2009, *A&A* **508**, L13

Mancini, L. and Feoli, A.: 2012, *A&A* **537**, A48

Marconi, A. and Hunt, L. K.: 2003, *ApJ* **589**, L21

Markoff, S.: 2005, *ApJ* **618**, L103

Markoff, S., Falcke, H., Yuan, F., and Biermann, P. L.: 2001, *A&A* **379**, L13

Marrone, D. P., Baganoff, F. K., Morris, M. R., Moran, J. M., Ghez, A. M., Hornstein, S. D., Dowell, C. D., Muñoz, D. J., Bautz, M. W., Ricker, G. R., Brandt, W. N., Garmire, G. P., Lu, J. R., Matthews, K., Zhao, J.-H., Rao, R., and Bower, G. C.: 2008, *ApJ* **682**, 373

Marrone, D. P., Moran, J. M., Zhao, J.-H., and Rao, R.: 2006, *ApJ* **640**, 308

Martin, C. L.: 2005, *ApJ* **621**, 227

Matthews, T. A. and Sandage, A. R.: 1963, *ApJ* **138**, 30

Mauerhan, J. C., Morris, M., Walter, F., and Baganoff, F. K.: 2005, *ApJ* **623**, L25

Mauerhan, J. C., Muno, M. P., Morris, M. R., Stolovy, S. R., and Cotera, A.: 2010, *ApJ* **710**, 706

McConnell, N. J., Ma, C.-P., Gebhardt, K., Wright, S. A., Murphy, J. D., Lauer, T. R., Graham, J. R., and Richstone, D. O.: 2011, *Nature* **480**, 215

McKee, C. F.: 1990, in L. Blitz (ed.), *The Evolution of the Interstellar Medium*, Vol. 12 of *Astronomical Society of the Pacific Conference Series*, pp 3–29

McKee, C. F. and Cowie, L. L.: 1975, *ApJ* **195**, 715

McKee, C. F. and Ostriker, J. P.: 1977, *ApJ* **218**, 148

McLaughlin, D. E., King, A. R., and Nayakshin, S.: 2006, *ApJ* **650**, L37

McLure, R. J., Jarvis, M. J., Targett, T. A., Dunlop, J. S., and Best, P. N.: 2006, *MNRAS* **368**, 1395

Melia, F. and Falcke, H.: 2001, *ARA&A* **39**, 309

Merloni, A., Heinz, S., and di Matteo, T.: 2003, *MNRAS* **345**, 1057

Merritt, D. and Ferrarese, L.: 2001, *MNRAS* **320**, L30

Merritt, D. and Quinlan, G. D.: 1998, *ApJ* **498**, 625

Mertsch, P. and Sarkar, S.: 2011, *Physical Review Letters* **107(9)**, 091101

Meszaros, P., Rees, M. J., and Papathanassiou, H.: 1994, *ApJ* **432**, 181

Meyer, F., Liu, B. F., and Meyer-Hofmeister, E.: 2000, *A&A* **361**, 175

Michell, J.: 1784, *Royal Society of London Philosophical Transactions Series I* **74**, 35

Misner, C. W., Thorne, K. S., and Wheeler, J. A.: 1973, *Gravitation*

Moellenhoff, C.: 1976, *A&A* **50**, 105

Molinari, S., Bally, J., Noriega-Crespo, A., Compiègne, M., Bernard, J. P., Paradis, D., Martin, P., Testi, L., Barlow, M., Moore, T., Plume, R., Swinyard, B., Zavagno, A., Calzoletti, L., Di Giorgio, A. M., Elia, D., Faustini, F., Natoli, P., Pestalozzi, M., Pezzuto, S., Piacentini, F., Polenta, G., Polychroni, D., Schisano, E., Traficante, A., Veneziani, M., Battersby, C., Burton, M., Carey, S., Fukui, Y., Li, J. Z., Lord, S. D., Morgan, L., Motte, F., Schuller, F., Stringfellow, G. S., Tan, J. C., Thompson, M. A., Ward-Thompson, D., White, G., and Umana, G.: 2011, *ApJ* **735**, L33

Monaghan, J. J.: 1992, *ARA&A* **30**, 543

Monaghan, J. J. and Gingold, R. A.: 1983, *Journal of Computational Physics* **52**, 374

Montgomery, C., Orchiston, W., and Whittingham, I.: 2009, *Journal of Astronomical History and Heritage* **12**, 90

Morris, J. P. and Monaghan, J. J.: 1997, *Journal of Computational Physics* **136**, 41

Morris, M., Ghez, A. M., and Becklin, E. E.: 1999, *Advances in Space Research* **23**, 959

Morris, M. and Serabyn, E.: 1996, *ARA&A* **34**, 645

Murray, N., Quataert, E., and Thompson, T. A.: 2005, *ApJ* **618**, 569

Nagar, N. M. and Wilson, A. S.: 1999, *ApJ* **516**, 97

Narayan, R.: 2002, in M. Gilfanov, R. Sunyeav, & E. Churazov (ed.), *Lighthouses of the Universe: The Most Luminous Celestial Objects and Their Use for Cosmology*, pp 405–+

Narayan, R., Mahadevan, R., Grindlay, J. E., Popham, R. G., and Gammie, C.: 1998, *ApJ* **492**, 554

Narayan, R. and Yi, I.: 1994, *ApJ* **428**, L13

Narayan, R., Yi, I., and Mahadevan, R.: 1995, *Nature* **374**, 623

Nayakshin, S.: 2005, *A&A* **429**, L33

Nayakshin, S., Cha, S.-H., and Hobbs, A.: 2009a, *MNRAS* **397**, 1314

Nayakshin, S. and Cuadra, J.: 2005, *A&A* **437**, 437

Nayakshin, S., Cuadra, J., and Springel, V.: 2007, *MNRAS* **379**, 21

Nayakshin, S., Cuadra, J., and Sunyaev, R.: 2004, *A&A* **413**, 173

Nayakshin, S., Dehnen, W., Cuadra, J., and Genzel, R.: 2006, *MNRAS* **366**, 1410

Nayakshin, S. and King, A.: 2007, *ArXiv e-prints*

Nayakshin, S. and Power, C.: 2010, *MNRAS* **402**, 789

Nayakshin, S., Power, C., and King, A. R.: 2012a, *ApJ* **753**, 15

Nayakshin, S., Sazonov, S., and Sunyaev, R.: 2012b, *MNRAS* **419**, 1238

Nayakshin, S. and Sunyaev, R.: 2003, *MNRAS* **343**, L15

Nayakshin, S., Wilkinson, M. I., and King, A.: 2009b, *MNRAS* **398**, L54

Neistein, E., van den Bosch, F. C., and Dekel, A.: 2006, *MNRAS* **372**, 933

Oppenheimer, J. R. and Volkoff, G. M.: 1939, *Physical Review* **55**, 374

Örndahl, E., Rönnback, J., and van Groningen, E.: 2003, *A&A* **404**, 883

Paczynski, B.: 1978, *Acta Astronomica* **28**, 91

Papaloizou, J. C. B. and Lin, D. N. C.: 1995, *ARA&A* **33**, 505

Paumard, T., Genzel, R., Martins, F., Nayakshin, S., Beloborodov, A. M., Levin, Y., Trippe, S., Eisenhauer, F., Ott, T., Gillessen, S., Abuter, R., Cuadra, J., Alexander, T., and Sternberg, A.: 2006, *ApJ* **643**, 1011

Paumard, T., Maillard, J.-P., and Morris, M.: 2004, *A&A* **426**, 81

Peng, C. Y., Impey, C. D., Ho, L. C., Barton, E. J., and Rix, H.-W.: 2006, *ApJ* **640**, 114

Peterson, B. M.: 1993, *PASP* **105**, 247

Peterson, B. M.: 1997, *An Introduction to Active Galactic Nuclei*

Pierce-Price, D., Richer, J. S., Greaves, J. S., Holland, W. S., Jenness, T., Lasenby, A. N., White, G. J., Matthews, H. E., Ward-Thompson, D., Dent, W. R. F., Zylka, R., Mezger, P., Hasegawa, T., Oka, T., Omont, A., and Gilmore, G.: 2000, *ApJ* **545**, L121

Ponti, G., Terrier, R., Goldwurm, A., Belanger, G., and Trap, G.: 2010, *ApJ* **714**, 732

Porquet, D., Grosso, N., Predehl, P., Hasinger, G., Yusef-Zadeh, F., Aschenbach, B., Trap, G., Melia, F., Warwick, R. S., Goldwurm, A., Bélanger, G., Tanaka, Y., Genzel, R., Dodds-Eden, K., Sakano, M., and Ferrando, P.: 2008, *A&A* **488**, 549

Porquet, D., Predehl, P., Aschenbach, B., Grosso, N., Goldwurm, A., Goldoni, P., Warwick, R. S., and Decourchelle, A.: 2003, *A&A* **407**, L17

Pounds, K. A., King, A. R., Page, K. L., and O'Brien, P. T.: 2003a, *MNRAS* **346**, 1025

Pounds, K. A., Reeves, J. N., King, A. R., Page, K. L., O'Brien, P. T., and Turner, M. J. L.: 2003b, *MNRAS* **345**, 705

Power, C., Nayakshin, S., and King, A.: 2011a, *MNRAS* **412**, 269

Power, C., Zubovas, K., Nayakshin, S., and King, A. R.: 2011b, *MNRAS* **413**, L110

Price, D. J.: 2012, *Journal of Computational Physics* **231**, 759

Pringle, J. E.: 1981, *ARA&A* **19**, 137

Rees, M. J.: 1988, *Nature* **333**, 523

Reid, M. J., Menten, K. M., Zheng, X. W., Brunthaler, A., and Xu, Y.: 2009, *ApJ* **705**, 1548

Revnivtsev, M. G., Churazov, E. M., Sazonov, S. Y., Sunyaev, R. A., Lutovinov, A. A., Gilfanov, M. R., Vikhlinin, A. A., Shtykovsky, P. E., and Pavlinsky, M. N.: 2004, *A&A* **425**, L49

Rice, W. K. M., Lodato, G., and Armitage, P. J.: 2005, *MNRAS* **364**, L56

Richardson, D. C., Bottke, W. F., and Love, S. G.: 1998, *Icarus* **134**, 47

Riffel, R. A. and Storchi-Bergmann, T.: 2011a, *MNRAS* **411**, 469

Riffel, R. A. and Storchi-Bergmann, T.: 2011b, *MNRAS* **417**, 2752

Rothschild, R. E., Boldt, E. A., Holt, S. S., and Serlemitsos, P. J.: 1974, *ApJ* **189**, L13

Różańska, A. and Czerny, B.: 2000, *A&A* **360**, 1170

Rupke, D. S. N. and Veilleux, S.: 2011, *ApJ* **729**, L27+

Rybicki, G. B. and Lightman, A. P.: 1979, *Radiative processes in astrophysics*

Salpeter, E. E.: 1964, *ApJ* **140**, 796

Sazonov, S. Y., Ostriker, J. P., Ciotti, L., and Sunyaev, R. A.: 2005, *MNRAS* **358**, 168

Schawinski, K., Thomas, D., Sarzi, M., Maraston, C., Kaviraj, S., Joo, S.-J., Yi, S. K., and Silk, J.: 2007, *MNRAS* **382**, 1415

Schawinski, K., Urry, C. M., Virani, S., Coppi, P., Bamford, S. P., Treister, E., Lintott, C. J., Sarzi, M., Keel, W. C., Kaviraj, S., Cardamone, C. N., Masters, K. L., Ross, N. P., Andreescu, D., Murray, P., Nichol, R. C., Raddick, M. J., Slosar, A., Szalay, A. S., Thomas, D., and Vandenberg, J.: 2010, *ApJ* **711**, 284

Schmidt, M.: 1962, *ApJ* **136**, 684

Schmidt, M.: 1963, *Nature* **197**, 1040

Schödel, R., Najarro, F., Muzic, K., and Eckart, A.: 2010, *A&A* **511**, A18

Schödel, R., Ott, T., Genzel, R., Hofmann, R., Lehnert, M., Eckart, A., Mouawad, N., Alexander, T., Reid, M. J., Lenzen, R., Hartung, M., Lacombe, F., Rouan, D., Gendron, E., Rousset, G., Lagrange, A.-M., Brandner, W., Ageorges, N., Lidman, C., Moorwood, A. F. M., Spyromilio, J., Hubin, N., and Menten, K. M.: 2002, *Nature* **419**, 694

Schulze, A. and Wisotzki, L.: 2011, *A&A* **535**, A87

Schwarzschild, K.: 1916, *Abh. Konigl. Preuss. Akad. Wissenschaften Jahre 1906,92, Berlin,1907* pp 189–196

Scoville, N. Z., Solomon, P. M., and Penzias, A. A.: 1975, *ApJ* **201**, 352

Serabyn, E., Shupe, D., and Figer, D. F.: 1998, *Nature* **394**, 448

Shakura, N. I. and Sunyaev, R. A.: 1973, *A&A* **24**, 337

Shapiro, S. L. and Teukolsky, S. A.: 1983, *Black holes, white dwarfs, and neutron stars: The physics of compact objects*, Wiley-Interscience

Shemmer, O., Netzer, H., Maiolino, R., Oliva, E., Croom, S., Corbett, E., and di Fabrizio, L.: 2004, *ApJ* **614**, 547

Shen, Z.-Q., Lo, K. Y., Liang, M.-C., Ho, P. T. P., and Zhao, J.-H.: 2005, *Nature* **438**, 62

Shields, G. A., Gebhardt, K., Salviander, S., Wills, B. J., Xie, B., Brotherton, M. S., Yuan, J., and Dietrich, M.: 2003, *ApJ* **583**, 124

Shields, G. A., Menezes, K. L., Massart, C. A., and Vanden Bout, P.: 2006, *ApJ* **641**, 683

Silk, J. and Rees, M. J.: 1998, *A&A* **331**, L1

Snowden, S. L., Egger, R., Freyberg, M. J., McCammon, D., Plucinsky, P. P., Sanders, W. T., Schmitt, J. H. M. M., Truemper, J., and Voges, W.: 1997, *ApJ* **485**, 125

Sofue, Y.: 2011, *ArXiv e-prints*

Soltan, A.: 1982, *MNRAS* **200**, 115

Spitzer, L.: 1987, *Dynamical evolution of globular clusters*

Springel, V.: 2005, *MNRAS* **364**, 1105

Springel, V.: 2010, *ARA&A* **48**, 391

Steinhardt, C. L. and Elvis, M.: 2010, *MNRAS* **402**, 2637

Stepney, S.: 1983, *MNRAS* **202**, 467

Stolte, A., Ghez, A. M., Morris, M., Lu, J. R., Brandner, W., and Matthews, K.: 2008, *ApJ* **675**, 1278

Sturm, E., González-Alfonso, E., Veilleux, S., Fischer, J., Graciá-Carpio, J., Hailey-Dunsheath, S., Contursi, A., Poglitsch, A., Sternberg, A., Davies, R., Genzel, R., Lutz, D., Tacconi, L., Verma, A., Maiolino, R., and de Jong, J. A.: 2011, *ApJ* **733**, L16+

Su, M., Slatyer, T. R., and Finkbeiner, D. P.: 2010, *ApJ* **724**, 1044

Sunyaev, R. and Churazov, E.: 1998, *MNRAS* **297**, 1279

Sutherland, R. S. and Dopita, M. A.: 1993, *ApJS* **88**, 253

Svetsov, V. V., Nemtchinov, E. V., and Teterev, A. V.: 1995, *Icarus* **116**, 131

Tacconi, L. J., Genzel, R., Lutz, D., Rigopoulou, D., Baker, A. J., Iserlohe, C., and Tecza, M.: 2002, *ApJ* **580**, 73

Tagger, M. and Melia, F.: 2006, *ApJ* **636**, L33

Tanaka, Y., Nandra, K., Fabian, A. C., Inoue, H., Otani, C., Dotani, T., Hayashida, K., Iwasawa, K., Kii, T., Kunieda, H., Makino, F., and Matsuoka, M.: 1995, *Nature* **375**, 659

Targett, T. A., Dunlop, J. S., and McLure, R. J.: 2012, *MNRAS* **420**, 3621

Terrier, R., Ponti, G., Bélanger, G., Decourchelle, A., Tatischeff, V., Goldwurm, A., Trap, G., Morris, M. R., and Warwick, R.: 2010, *ApJ* **719**, 143

Thacker, R. J., Scannapieco, E., and Couchman, H. M. P.: 2006, *ApJ* **653**, 86

Thompson, T. A., Quataert, E., and Murray, N.: 2005, *ApJ* **630**, 167

Tolman, R. C.: 1939, *Physical Review* **55**, 364

Tombesi, F., Cappi, M., Reeves, J. N., Palumbo, G. G. C., Yaqoob, T., Braito, V., and Dadina, M.: 2010a, *A&A* **521**, A57+

Tombesi, F., Sambruna, R. M., Reeves, J. N., Braito, V., Ballo, L., Gofford, J., Cappi, M., and Mushotzky, R. F.: 2010b, *ApJ* **719**, 700

Toomre, A.: 1964, *ApJ* **139**, 1217

Trap, G., Goldwurm, A., Dodds-Eden, K., Weiss, A., Terrier, R., Ponti, G., Gillessen, S., Genzel, R., Ferrando, P., Bélanger, G., Clénet, Y., Rouan, D., Predehl, P., Capelli, R., Melia, F., and Yusef-Zadeh, F.: 2011, *A&A* **528**, A140+

Treister, E., Schawinski, K., Volonteri, M., Natarajan, P., and Gawiser, E.: 2011, *Nature* **474**, 356

Tremaine, S., Gebhardt, K., Bender, R., Bower, G., Dressler, A., Faber, S. M., Filippenko, A. V., Green, R., Grillmair, C., Ho, L. C., Kormendy, J., Lauer, T. R., Magorrian, J., Pinkney, J., and Richstone, D.: 2002, *ApJ* **574**, 740

Treu, T., Ellis, R. S., Liao, T. X., and van Dokkum, P. G.: 2005, *ApJ* **622**, L5

Čadež, A., Calvani, M., and Kostić, U.: 2008, *A&A* **487**, 527

van der Laan, H.: 1966, *Nature* **211**, 1131

Veilleux, S., Rupke, D. S. N., Kim, D.-C., Genzel, R., Sturm, E., Lutz, D., Contursi, A., Schweitzer, M., Tacconi, L. J., Netzer, H., Sternberg, A., Mihos, J. C., Baker, A. J., Mazzarella, J. M., Lord, S., Sanders, D. B., Stockton, A., Joseph, R. D., and Barnes, J. E.: 2009, *ApJS* **182**, 628

Vestergaard, M. and Osmer, P. S.: 2009, *ApJ* **699**, 800

Vishniac, E. T.: 1983, *ApJ* **274**, 152

Wardle, M. and Yusef-Zadeh, F.: 2008, *ApJ* **683**, L37

Watson, C. R., Kochanek, C. S., Forman, W. R., Hickox, R. C., Jones, C. J., Brown, M. J. I., Brand, K., Dey, A., Jannuzi, B. T., Kenter, A. T., Murray, S. S., Vikhlinin, A., Eisenstein, D. J., Fazio, G. G., Green, P. J., McNamara, B. R., Rieke, M., and Shields, J. C.: 2009, *ApJ* **696**, 2206

Wyatt, M. C.: 2008, *ARA&A* **46**, 339

Yuan, F., Markoff, S., and Falcke, H.: 2002, *A&A* **383**, 854

Yuan, F., Quataert, E., and Narayan, R.: 2003, *ApJ* **598**, 301

Yuan, F., Quataert, E., and Narayan, R.: 2004, *ApJ* **606**, 894

Yusef-Zadeh, F., Bushouse, H., Dowell, C. D., Wardle, M., Roberts, D., Heinke, C., Bower, G. C., Vila-Vilaró, B., Shapiro, S., Goldwurm, A., and Bélanger, G.: 2006a, *ApJ* **644**, 198

Yusef-Zadeh, F., Hewitt, J. W., Arendt, R. G., Whitney, B., Rieke, G., Wardle, M., Hinz, J. L., Stolovy, S., Lang, C. C., Burton, M. G., and Ramirez, S.: 2009, *ApJ* **702**, 178

Yusef-Zadeh, F., Roberts, D., Wardle, M., Heinke, C. O., and Bower, G. C.: 2006b, *ApJ* **650**, 189

Yusef-Zadeh, F., Wardle, M., Bushouse, H., Dowell, C. D., and Roberts, D. A.: 2010, *ApJ* **724**, L9

Zel'Dovich, Y. B.: 1964, *Soviet Physics Doklady* **9**, 195

Zel'Dovich, Y. B. and Novikov, I. D.: 1971, *Theory of gravitation and the evolution of stars.*

Zubovas, K. and King, A.: 2012, *ApJ* **745**, L34

Zubovas, K., King, A. R., and Nayakshin, S.: 2011, *MNRAS* **415**, L21

Zubovas, K. and Nayakshin, S.: 2012, *MNRAS* **424**, 666